MASTER'S THESIS IN PHYSICS

SEARCH FOR LARGE EXTRA DIMENSIONS IN DIMUON EVENTS WITH THE CMS EXPERIMENT AT $\sqrt{s} = 8\,\text{TeV}$

Written by

TOBIAS POOK

Submitted to the

FACULTY FOR MATHEMATICS, COMPUTER SCIENCE AND NATURAL SCIENCES

Created at the

III. PHYS. INST. A

of the

RWTH AACHEN UNIVERSITY

Supervised by

PROF. DR. THOMAS HEBBEKER

Second examiner

PROF. DR. CHRISTOPHER WIEBUSCH

May 28, 2014

Abstract

The Large Hadron Collider (LHC) experiment operated at a center of mass energy of $\sqrt{s} = 8\,\text{TeV}$ during the 2012 Run and the Compact Muon Solenoid (CMS) experiment recorded signatures of particle collisions with an integrated luminosity of $20.6\,\text{fb}^{-1}$. Signatures from collisions where two high energy muons emerge are studied and interpreted in the Arkani-Hamed, Dimopoulos, Dvali (ADD) model of large spartial extra dimensions. The ADD model predicts a non-resonant excess in the tails of the dimuon invariant mass distribution. Several background processes are studied with Monte Carlo simulation. The Drell-Yan process is the dominant source of background events and it is studied in detail up to NNLO in QCD and NLO in EW. Several sources of systematic uncertainty influence both the theoretical model and the measurement and are studied in detail for high mass dimuon events. The dimuon spectrum with yet inaccessible particle energies is evaluated and no evidence for a signal is observed. The number of events above dimuon masses of $unit[1.9]\text{TeV}$ is used to set lower limits on the string scale M_s between $4.6\,\text{TeV}$ and $3.1\,\text{TeV}$ for $n = 3$ to $n = 7$ extra dimensions in the ADD model at 95% confidence level. The exclusion limits are further extended by a combination of dilepton mass spectra ($ee+\mu\mu$) for masses above $2.0\,\text{TeV}$. The combination gives lower limits on M_s between $4.9\,\text{TeV}$ and $3.3\,\text{TeV}$ for $n = 3$ to $n = 7$ extra dimensions.

Zusammenfassung

Das Large Hadron Collider (LHC) Experiment wurde im Jahr 2012 mit einer Schwerpunktsenergie von $\sqrt{s} = 8\,\text{TeV}$ betrieben und das Compact Muon Solenoid (CMS) Experiment hat Signaturen von Teilchenkollisionen mit einer integrierten Luminosität von $20.6\,\text{fb}^{-1}$ aufgezeichnet. Signaturen von Ereignissen, bei denen zwei hochenergetische Myonen entstehen, werden studiert und im Arkani-Hamed, Dimopoulos, Dvali (ADD) Modell für ausgedehnte räumliche Dimensionen interpretiert. Das ADD Modell sagt einen nicht-resonanten Überschuss in den Ausläufern des Invariante Massespektrums von Myonpaaren voraus. Verschiedene Untergründe werden mit Monte-Carlo-Simulationen untersucht. Der Drell-Yan-Prozess ist die dominante Untergrundquelle und wird detailliert bis zo NNLO in QCD und NLO in EW studiert. Verschiedene Quellen systematischer Unsicherheit beeinflussen sowohl die theoretische Beschreibung als auch die Messungen und werden detailliert für Ereignisse mit zwei hochenergetischen Myonen untersucht. Das zwei Myon Invariante Massespektrum mit bisher unzugänglichen Teilchenenergien wird evaluiert und es wir keine Evidenz für ein Signal beobachtet. Die Anzahl von Ereignissen mit einer Masse des Myonpaars über $1.9\,\text{TeV}$ wird benutzt um untere Ausschlussgrenzen mit 95% Konfidenzniveau auf die String Skala M_s zwischen $4.6\,\text{TeV}$ und $3.1\,\text{TeV}$ für $n = 3$ bis $n = 7$ zusätzliche Dimensionen im ADD Modell zu setzen. Die Ausschlussgrenzen werden zusätzlich durch eine Kombination der Massenspektren für den zwei Elektron und zwei Myon Kanal mit Massen über $2.0\,\text{TeV}$ erweitert. Die Kombination ergibt untere Ausschlussgrenzen auf M_s zwischen $4.9\,\text{TeV}$ und $3.3\,\text{TeV}$ für $n = 3$ bis $n = 7$ zusätzliche Dimensionen

Contents

1. Introduction

This thesis describes the search for extra dimensions on quantum scales, and this introduction aims to guide the reader into this topic with some basic considerations about the concept of spatial dimensions and how an observer may perceive additional space dimensions. Hypothetical extra dimensions need to be somehow different from our known three spatial dimensions as the current models describe common physical processes very well, e.g. the momentum is always conserved assuming three spatial dimensions. One common approach to explain why additional dimensions may not change our everyday perception of reality is to assume them to be compactified and limited in size. A popular way [1] to illustrate this concept is the ant on an infinitely long thread as shown in figure 1.1. The ant can move along the thread (z-axis) and around the thread (ϕ-axis). The ϕ axis is compactified, as the ant reaches its initial position when it continuously moves along the ϕ direction. The size of this dimension is described by the width or radius of the line. A human who observes the ant with a distance of some meters may notice the line only as a one dimensional object and overlook the additional compactified dimension.
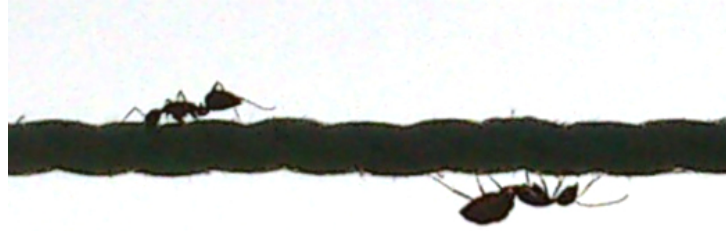
Figure 1.1.: The ant on a thread as a classical example for an observer in a higher dimensional space [2].

This example may be simplistic but it already contains most of the general concepts for the extra dimensional model studied in this thesis. This leads to the questions: If n additional compactified dimensions exist, how would they change our known space-time and why did we find no evidence for them so far?

A direct but still classical consequence would be a change of Newton's law at length scales comparable to the radius R of the compactified dimension [3, 4]. The structure of the field equation for the gravitational force field $\vec{F}(\vec{r})$ created by a mass density $\rho(\vec{r})$ is unchanged by a generalization to (3+n) space dimensions. The conservation of mass demands a conservation of the gravitational force field divergence within a sphere of arbitrary size following Gauss's law:

$$m \propto \int_V \mathrm{div}\vec{F} = \int_A \vec{F} \propto F(r)\, r^{n+2}, \tag{1.1}$$

This implies two boundary cases $R \ll r$ and $R \gg r$ for the radial gravitational force:

1

$$F(r) \propto \begin{cases} \frac{1}{r^2} & R \ll r \\ \frac{1}{r^{n+2}} & R \gg r \end{cases} \tag{1.2}$$

It can be seen from equation 1.2 that additional dimensions would not change Newton's law as we know it, as long as one measures the gravitational force on a length scale much larger than the radius R of the compactified extra dimension. For length scales much smaller than R the gravitational force can propagate into the extra dimension similar to the the 3 known spatial dimensions and the resulting power law would change its exponent dependent on the number of additional dimensions. Newton's law is currently tested down to the sub-millimetre range with torsion balance experiments. A summary of these experiments together with constraints for large extra dimensions can be found in section 2.2.1.

Modern theoretical physics considers the idea of additional spatial dimensions as a possible extension to our space time at least since Kaluza showed[1] in 1921 that a five-dimensional spacetime can be split into the Einstein equations and the Maxwell equations in four dimensions [6]. Kaluza's theory was later extended by Oskar Klein to what is today known as the Kaluza-Klein (KK) theory by introducing the idea, that the additional spatial dimension is compactified on a circle. The interest in KK theories declined with the discovery of quantum mechanics and the subsequent development of the standard model of particle physics (SM).

The standard model comprises our current knowledge about the interactions between the so far discovered fundamental constituents of matter in terms of three elementary forces. Despite its capability to predict a wide variety of phenomena with high precision, the SM is still not able to include the effects of gravity. Some of the problems which arise during the quantization of gravity are described in section 2.1. The unification of all forces into one fundamental formula first tried by Kaluza still remains one of the great challenges in theoretical physics and the idea of additional dimensions still plays a major part in current approaches to achieve this goal, e.g. string theory needs more than the known 4 dimensional space to develop an approach for a unified theory of our universe. Here extra dimensions are needed to inherit enough degrees of freedom within the theory to generate the known standard model fields from modes of the underlying strings (e.g. $n_{dimensions} = 11$ for M-theory [7, 8]).

The following thesis starts with a brief introduction to the standard model of particle physics and current approaches to include quantum gravity into it. The next chapter describes extensions to the standard model with additional spatial dimensions with emphasis on the **A**rkani-Hamed, **D**imopulus and **D**vali (ADD) model, which predicts a non-resonant excess in the cross section for the process $p + p \rightarrow ll$. As explained before, the right scale of observation is crucial to notice extra dimensions, and small length scales correspond to high energies in the quantum world. The LHC particle collider located near Geneva operated at a center of mass energy of $\sqrt{s} = 8\text{TeV}$ in 2012 and allows to study the structure of spacetime at yet inaccessible length scales. The LHC is described in the third chapter together with the CMS particle detector which is used to measure particles which emerge in proton-proton collisions at the LHC. The next chapters explain how muons are reconstructed and simulated within CMS and which uncertainties arise in this procedure. The introduced methods are used to study the dimuon invariant mass spectrum and extend previous exclusion limits for the ADD model in light of the new measurement.

---

[1]A first attempt for this was taken out by Gunnar Nordström, but did not receive general recognition [5].

1.1. Units, Notation and References

Some initial remarks about notation and units are necessary to shorten the later description of formulas. Summation over repeating indices is implied if not stated otherwise. In descriptions of Lagrangian densities γ^μ denotes the Dirac matrices and ϵ^{ijk} the total antisymmetric tensor [2] and c denotes the speed of light if not stated otherwise.

SI units[9] are only used to describe the geometry and electrical properties of CMS detector parts. The description of particle interactions uses natural units ($\hbar = c = 1$).

Most references in this thesis are published in peer-reviewed journals, part of publicly available conference contributions or official CMS publications. Yet some detailed aspects regarding the CMS detector are only described in internal documentation and the referenced documents are only available to CMS collaborators.

---

[2]The indices may be different in some contexts.

1.2. Standard Model

The standard model of particle physics (SM) describes the interaction of matter from length scales comparable to the size of molecules down to the smallest length scales accessible to current experiments below the subatomic level $\mathcal{O}(10^{-19}\mathrm{m})$. It describes the interaction of fermion fields (spin $\frac{1}{2}$) in terms of three elementary forces and their charges: *electromagnetic force* (electric charge), *weak force* (weak isospin) and *strong force* (color charge), where weak and electromagnetic force are unified at high energies. The forces are mediated by integer spin particles called bosons. The fermions can be categorized into particles that carry a color charge (quarks) and particles that do not (leptons), thus only quarks participate in strong interactions.

The following description of the standard model is mainly based on [10, 11, 12, 13], yet numerous similar descriptions exists and the reader may be refered to one of the cited publications when a part of the description is not directly referenced to another source.

	1st generation	2nd generation	3rd generation	charge Q	weak Isospin I_3
Leptons:	$\begin{pmatrix} e \\ \nu_e \end{pmatrix}_L, e_R$	$\begin{pmatrix} \mu \\ \nu_\mu \end{pmatrix}_L, \mu_R$	$\begin{pmatrix} \tau \\ \nu_\tau \end{pmatrix}_L, \tau_R$	$1e$ 0	$\frac{-1}{2}$, 0 $\frac{1}{2}$
Quarks:	$\begin{pmatrix} u \\ d' \end{pmatrix}_L,\ u_R \\ d_R$	$\begin{pmatrix} c \\ s' \end{pmatrix}_L,\ c_R \\ s_R$	$\begin{pmatrix} t \\ b' \end{pmatrix}_L,\ t_R \\ b_R$	$\frac{2}{3}e$ $\frac{-1}{3}e$	$\frac{1}{2}$, 0 $\frac{-1}{2}$, 0

Table 1.1.: Overview of fermions in the standard model.

An overview of the fermions in the standard model can be found in table 1.1. Both quarks and leptons can be grouped into three so called generations or families. Each generation represents a exact heavier copy of the previous generation. Neither the origin of fermions nor the mass hierarchy is explained within the SM.

Leptons

The charged leptons consist of three particles with charge $1e$ (electron e, muon μ, and tau τ) and their corresponding antiparticles with same quantum numbers and mass, but opposite charge. A neutral and almost massless [3] (anti-)neutrino ν exists for every charged lepton. The indices R, L in table 1.1 indicate the chiral structure of the standard model introduced by the weak interaction. Only left handed particles and right handed anti-particles have a non-vanishing Isospin I_3 and participate in weak interactions, leading to a left handed weak Isospin doublet and a right handed singlet for each generation.

---

[3]Only upper bounds on the neutrino mass exist, but the discovery of neutrino oscillations is clear evidence that neutrinos have a non vanishing mass [14].

Quarks

Quarks consist of particles with electric charge $2/3e$ (up u, charm c, top t) and charge $-1/3e$ (down d, strange s, bottom b). The dashed quarks d', s', b' in table 1.1 indicate that the weak isospin eigenstates and the mass eigenstates for quarks can not be diagonalized at the same time. They are related by the *Cabibbo–Kobayashi–Maskawa* (CKM) matrix (details can be found in e.g. [12, 13]). The components of the CKM matrix can not be predicted by the standard model and the complex phase in the CKM matrix is source of the observed CP-violation in the SM.

1.2.1. Structure of the Standard Model

One of the remarkable properties of the standard model is its ability to explain a wide range of physical processes with a diverse phenomenology using one common principle: *gauge invariance* under symmetry transformation. All interactions in the standard model can be described by imposing the invariance of the Lagrangian density $\mathcal{L}$ under a group of local symmetry transformations. The following description is a brief summary of the approach in [13].

Each SM force can be described by a Lagrangian density $\mathcal{L}[\phi, \partial_\mu \phi]$ which is invariant under a D dimensional group of transformations:

$$\phi'(x) = U(\theta^i)\phi(x) \qquad (i = 1, .., D) \tag{1.3}$$

where $\boldsymbol{\theta}$ characterises the transformation $U(\theta^i)$ [4], it can be described using the group generators T^i in the representation of the fields ϕ and the coupling constant g:

$$U(\theta^i) = \exp\left(ig \sum_i \theta^i T^i\right) \approx 1 + ig \sum_i \theta^i T^i \tag{1.4}$$

The generators T^i in the SM are independent of the space-time point x, which means that the SM contains only internal symmetries of the Poincaré group and does not extend space-time itself, in contrast to extra dimensions [15] or SUSY [16, 17] models. The forces of the SM can all be described by unitary transformations leading to hermitian generators, which in general do not commute and can be described using the fully anti-symmetric structure constants C_{ijk} of the group:

$$[T^i, T^j] = iC_{ijk}T^k \tag{1.5}$$

The SM consists of local gauge field theories, which means, that the parameters θ depend on the space-time coordinate x_μ. In order to conserve the gauge invariance, it is necessary to replace the ordinary derivative by the covariant derivative:

$$D_\mu = \partial_\mu + ig\mathbf{V}_\mu, \tag{1.6}$$

introducing a set of D gauge vector fields (one for every group generator) where the gauge fields are defined by their behaviour under the studied gauge transformation and can be

---

[4]e.g. an angle for rotation groups

reduced to a tensor of the adjoint group representation:

$$\mathbf{V}'_\mu = U\mathbf{V}_\mu U^{-1} - \frac{1}{ig}(\partial_\mu U)U^{-1} \approx \mathbf{V}_\mu + ig[\boldsymbol{\theta}, \mathbf{V}_\mu]... \tag{1.7}$$

This redefinition of the first derivative leads to the same behaviour under gauge transformations for ϕ and $D_\mu\phi$. The standard model aims to be a closed theory without external fields. In order to achieve this independence, it is necessary to add kinetic terms for the new introduced fields in the Lagrangian density:

$$\mathcal{L}_{YM} = -\frac{1}{2}Tr(\mathbf{F}_{\mu\nu}\mathbf{F}^{\mu\nu}) + \mathcal{L}[\phi, D_\mu\phi], \tag{1.8}$$

where $\mathbf{F}_{\mu\nu}$ describes the field strength tensor for the gauge fields. The complete gauge invariant Lagrangian is referred to as *Yang-Mills Lagrangian*. The last step to derive a quantum gauge theory is the quantization of the fields in eq. 1.8 and the following regularization and renormalization, which is necessary for the calculation of finite probabilities within the theory. For the SM it is necessary to introduce a dependency on the energy scale at which the coupling is observed during the renormalization. This effect is called *running couplings*. The quantization of a field theory by canonical quantization of the action is explained in more detail in the next chapter in context of the quantization of gravitational fields.

1.2.2. Formulation of the Standard Model

The concepts introduced in the last section can be incorporated to formulate the SM as a field theory for fermions which is invariant under $SU(3)_C \times SU(2)_L \times U(1)_Y$ gauge transformations. Here C denotes the invariance of color charges under SU(3) transformations and is associated to the strong force, described in the framework of *quantum chromodynamics* (QCD). The following two terms represent the electroweak-force which is described in the framework of *quantum flavour dynamics*. In the second term L indicates that only left-handed fermions possess a non-vanishing isospin charge τ_3, which is invariant under SU(2) transformations within the SM. The last term describes the invariance of hypercharges Y under U(1) transformations. The electroweak symmetry is broken below the electro-weak scale $v \approx 246\text{GeV}$ leading to a separation into electromagnetic and weak force and an additional massive higgs field.

Quantum Chromo Dynamics QCD

Following equation 1.8 the QCD Lagrangian is given by [18]:

$$\mathcal{L}_{QCD} = -\frac{1}{4}F^{A\mu\nu}F_A^{\mu\nu} + \sum_q \bar{\psi}_{q,a}(i\gamma^\mu\partial_\mu\delta_{ab} - g_s\gamma^\mu t_{ab}^C G_\mu^C - m_q\delta_{ab})\psi_{q,b} \tag{1.9}$$

where $\psi_{q,.}$ denotes quark-field spinors with flavour q and mass m_q, G_μ^C the 8 massless gluon gauge fields, t_{ab}^C the SU(3) structure constants. Indices for the three color charges are denoted a,b. The gluon fields carry a color charge resulting in gluon-gluon self coupling terms. Terms including the structure constant result in a changed color charge in QCD interactions. The renormalization of QCD introduces a running of the strong coupling constant α_s, where α_s

vanishes in the ultraviolet limit and reaches a non-perturbative region below an infrared cut-off Λ_{QCD} [18]. This effect causes two characteristic phenomena in QCD:

- **Asymptotic freedom:** The coupling in QCD interactions with large four-momentum transfer is small and it can be calculated perturbatively.

- **Confinement:** The energy stored in the flux field rises approximately linear with the distance between two color carrying particles. If the energy stored in the field is large enough, secondary particles emerge from the vacuum state until the momentum of all particles is small enough to form bound states (hadrons). This process is called *hadronization* and the emerging particle cascade is referred to as a jet. As a consequence it is not possible to observe single hadrons, they are always in color-neutral bound states .

Parton Distributions functions   In the hadron collider LHC protons are brought to collision, but only one parton per proton within the two interacting protons participates in the hard interaction at leading order. The distribution of the total proton momentum among the particles within the proton (partons) is subject to non-perturbative QCD and it is thus not possible to perturbatively calculate cross sections from the initial state. Yet it is possible to exploit that the time scales for interactions at high energies are much smaller than the time scales for significant changes in the parton momentum distribution. Using one of the *QCD factorization theorems*[19, 18, 3] it is possible to describe the inelastic scattering of two hadrons $\mathcal{H}_1, \mathcal{H}_2$ by:

$$\sigma(\mathcal{H}_1, \mathcal{H}_2 \rightarrow X + \text{hadron remnants}; Q, \mu_f, \mu_R) =$$
$$\sum_{i,j} \int dx_1 dx_2 \; f_{i,H1}(x_1, Q, \mu_F) \cdot f_{i,H2}(x_2, Q, \mu_F) \cdot \hat{\sigma}(\mathcal{P}_i + \mathcal{P}_i \rightarrow X, x_1, x_2, Q, \mu_F, \mu_R) \quad (1.10)$$

where the indices i,j label different types of partons in the hadron.[5] The *parton distribution functions* (PDF) $f_{i,H1}$ describe the probability that a hadron of type i participates in the interaction with hadron momentum fraction x_i at the factorization scale μ_F and process scale[6] Q. The high-energy parton parton interaction cross section at renormalization scale μ_R is described by $\hat{\sigma}$ and can be calculated perturbativly. The parton distribution functions describe non-perturbative parts of the theory and can not be calculated analytically. Yet it is possible to measure PDF contributions at a certain scale and extrapolate the results to another scale using the DGLAP [19, 18] equations. In practice various factors[7] influence the fitted PDF functions and the variations among PDF sets from different theory groups exceed the uncertainties in the single set sometimes by more than an order in magnitude. This is taken into account in most physics analyses by considering different PDF sets and using the variation for the parameter of interest as an uncertainty in the final result, see section 8.3.

---

[5]A proton for example consists of virtual quarks, called sea quarks, of different flavour and gluons beside the three main constituents 2 up and one down quark.

[6]In the case of dimuon events Q can be identified with the dimuon invariant mass.

[7]e.g. the chosen set of measurements, treatment of quark masses or modelling of uncertainties.

1. Introduction

Electroweak Force and Symmetry Breaking

The electro-weak force Lagrangian is given by:

$$\mathcal{L}_{EW} = \mathcal{L}_{gauge} + \mathcal{L}_f + \mathcal{L}_\phi + \mathcal{L}_{Yukawa}. \tag{1.11}$$

The first two terms describe the Yang-Mills gauge theory for $SU(2)_L \times U(1)_Y$ symmetries as described in section 1.2.1:

- The gauge term contains kinetic and self coupling terms for the SU(2) gauge fields W_μ^i (i=1,2,3) and the U(1) field B_μ:

$$\mathcal{L}_{gauge} = -\frac{1}{4} F_{\mu\nu}^i F_i^{\mu\nu} - \frac{1}{4} B_{\mu\nu} B^{\mu\nu} \tag{1.12}$$

$$B_{\mu\nu} = \partial_\mu B_\nu - \partial_\nu B_\mu \tag{1.13}$$

$$F_{\mu\nu}^i = \partial_\mu W_\nu^i - \partial_\nu W_\mu^i - g\epsilon_{jk}^i W_\mu^j W_\nu^k \tag{1.14}$$

- The fermion Lagrangian $\mathcal{L}_f$ contains kinetic terms for massless fermions and fermion-gauge boson couplings:

$$\mathcal{L}_f = \bar{L}\gamma^\mu \left(i\partial_\mu - g\frac{\tau_3^i}{2}W_\mu^i - g'\frac{Y}{2}B_\mu\right) L + \bar{R}\gamma^\mu \left(i\partial_\mu - g'\frac{Y}{2}B_\mu\right) R \tag{1.15}$$

Where L,R denote left and right handed fermions and g,g' the coupling constants for isospin τ_3 and hypercharge Y, respectivly. It can be seen that right handed fermions interact only by their hypercharge while left handed fermions inherit an additional non-vanishing isospin component which couples to the SU(2) gauge fields.

All particles in the Yang-Mills theories discussed so far contain only massless particles. This is in contradiction to the observed massive vector bosons [18] $W^\pm$, Z and the fermion masses. Yet it is crucial that the gauge bosons remain massless at high energies in order to keep the theory renormalizable. The concept of electroweak symmetry breaking allows to fulfil both requirements at the same time. In the presented approach the symmetry breaking is induced by introducing an additional complex scalar field $\phi = \binom{\phi^+}{\phi^0}$ with associated potential:

$$V(\phi) = \mu^2 \phi^\dagger \phi + \lambda(\phi^\dagger \phi)^2 \tag{1.16}$$

The potential adds additional interaction terms: $\mathcal{L}_\phi$ for gauge bosons and $\mathcal{L}_{Yukawa}$ for fermions to the Lagrangian. The potential has a non-vanishing vacuum expectation value for $\mu < 0$: $\phi_{min} = \frac{1}{2}\binom{0}{v}$, which breaks the SU(2) symmetry and creates particle masses bellow the electro-weak scale $v \approx 246$GeV. The consequences of the new field are described briefly bellow:

- $\mathcal{L}_\phi$ contains terms for the interaction between the scalar field and SU(2) $\times$ U(1) gauge fields [13]:

$$\mathcal{L}_\phi = \left| \left(i\partial_\mu - g\frac{\tau_3^i}{2}W_\mu^i - g'\frac{Y}{2}B_\mu\right)\phi \right|^2 - V(\phi) \tag{1.17}$$

ϕ can be approximated linearly for energy scales below v :

$$\phi \approx \begin{pmatrix} 0 \\ v + h(x) \end{pmatrix} \tag{1.18}$$

and equation 1.17 can be written as:

$$\mathcal{L}_\phi = \frac{v^2}{8} \left[g^2 \left((W_\mu^1)^2 + (W_\mu^2)^2 \right) + \left(g W_\mu^3 - g' B_\mu \right)^2 \right] + \mathcal{L}_h \tag{1.19}$$

After the symmetry breaking the fields in equations 1.12 and 1.19 can be reordered into the massive gauge bosons of the weak force $W^\pm, Z$, the massless photon field A_μ of the electromagnetic force, and a new massive scalar particle, the Higgs boson. The mass terms can be read off from equation 1.19:

$$W_\mu^\pm = \frac{1}{\sqrt{2}}(W_\mu^1 \mp i\, W_\mu^2) \qquad\qquad m_W = \frac{g\, v}{2} \tag{1.20}$$

$$Z_\mu = \frac{1}{\sqrt{g^2 + g'^2}}(g\, W_\mu^3 - g' B_\mu) \qquad\qquad m_Z = \frac{v}{2}\sqrt{g^2 + g'^2} \tag{1.21}$$

$$A_\mu = \frac{1}{\sqrt{g^2 + g'^2}}(g'\, W_\mu^3 - g\, B_\mu) \qquad\qquad m_A = 0 \tag{1.22}$$

and the additional term $\mathcal{L}_h$ in 1.19 describes higgs self interaction terms.

- The Yukawa term $\mathcal{L}_{Yukawa}$ describes the coupling between scalar field and fermions. For the first generation $\mathcal{L}_{Yukawa}$ is given by[8] [13]:

$$\mathcal{L}_{Yukawa} = -(\Gamma_u^{mn}\, \bar{q}_{m,L}\, \tilde{\phi}\, u_{n,R} + \Gamma_d^{mn}\, \bar{q}_{m,L}\, \phi\, d_{n,R} + \Gamma_e^{mn}\, \bar{l}_{m,L}\, \phi\, e_{n,R} + \Gamma_\nu^{mn}\, \bar{l}_{m,L}\, \tilde{\phi}\, \nu_{n,R}) \tag{1.23}$$

where the fermion field use a chiral representation. The Γ_{mn} matrix elements describe the coupling for left handed doublets (n, m) and right handed singlets. For $\phi = \phi_{min}$ the fermion terms take the form:

$$\frac{f_f\, v}{\sqrt{2}}\, (\bar{f}_L\, f_R + \bar{f}_R\, f_L) \tag{1.24}$$

where fermion mass terms $m_f = -\frac{f_f v}{\sqrt{2}}$ proportional to the Yukawa coupling appear for the previously massless fermions [9].

Observations from previous experiments [20, 21] can be described with great precision within the theory of electro-weak symmetry breaking and the recent discovery of a Higgs like boson at the LHC experiments CMS and ATLAS with a mass of about 126 GeV [22, 23] gives strong evidence that the broken symmetry can be explained by the Brout–Englert–Higgs mechanism [10], as it was presented in this section.

---

[8]Additional terms with the same structure exist for the other generations.

[9]The Yukawa coupling between the higgs field and fermions is not required for EW symmetry breaking but measurements at the LHC indicate that the discovered boson is not fermiophobic. Yet massless fermions are required for a renormalizable field theory

[10]The discovery of the higgs boson lead to a nobel price in 2013 for the theoretical description of the BEH mechanism [24]

Neutral Drell-Yan Process at LO

The neutral Drell-Yan process[11] describes the production of a lepton pair with opposite sign in hadron collisions [25]. It is the main background in the following analysis and directly influences the later introduced extra dimension signal by interference. At leading order only one constituent of every proton participates in the hard interaction. Following the approach presented in section 1.2.2 the description focuses on the electro-weak cross section in the center-of-mass (cms) frame [3, 26]:

$$\hat{\sigma}(q\bar{q} \to l\bar{l}) = \frac{1}{16\pi\hat{s}^2} \overline{|\mathcal{M}(q\bar{q} \to l\bar{l})|}, \tag{1.25}$$

where $\mathcal{M}$ represents the squared Feynman amplitude summed over final state spins and averaged over initial spins and colours. $\mathcal{M}$ can be calculated using the EW Feynman rules [12](see e.g. [12]):

$$\mathcal{M}(q\bar{q} \to l\bar{l}) = T_\gamma^{q\bar{q}} + T_Z^{q\bar{q}} + T_{Z\gamma}^{q\bar{q}} \tag{1.26}$$

with contributions from photon, Z-boson and inference terms resulting in a differential cross section:

$$\frac{d\sigma}{d\Omega} = \frac{\pi^2\alpha^2}{768} \cdot \left\{ \left(c_1 + |D_z(\bar{s})|^2 \cdot \hat{s}^2 \cdot \left[c_2 + c_3 \cdot \left(1 - \frac{m_Z^2}{\hat{s}} \right) \right] \right) \cdot (1 + \cos\theta^*)^2 \right.$$
$$\left. + \left(c_1 + |D_z(\bar{s})|^2 \cdot \hat{s}^2 \cdot \left[c_4 + c_5 \cdot \left(1 - \frac{m_{Z^2}}{\hat{s}} \right) \right] \right) \cdot (1 - \cos\theta^*)^2 \right\}, \tag{1.27}$$

with partonic cms energy $\hat{s} = (p_1+p_2)^2$ and Z-boson mass m_Z and θ^* defined as the scattering angle of the positively charged muon in the dimuon cms frame. Expressions for the Z-boson propagator $|D_z(\bar{s})|$ and constants c_i can be found in appendix A.

1.2.3. The Higgs Mass Hierarchy Problem
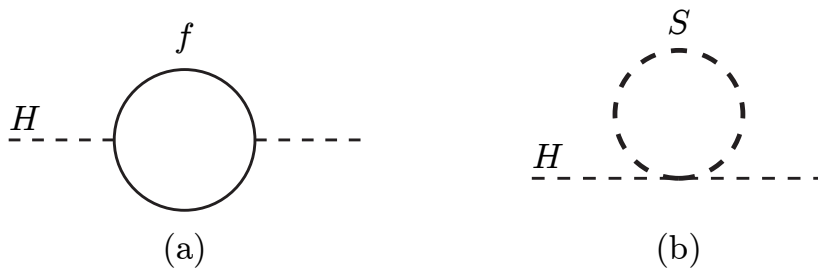
Figure 1.2.: Feynman graphs for one loop corrections to the higgs mass from: a) fermions and b) bosons. Graphic taken from [16].

.

The measured higgs mass of 126 GeV is built-up from the bare higgs mass and higher

---

[11]From here on Drell-Yan will denote always the neutral Drell-Yan process, references to the charged Drell-Yan process appear always as the full description.

[12]The Feynman graph for the s-channel LO Drell-Yan process is shown in figure 2.2.

order corrections:

$$m_h^2 = m_0^2 + \Delta m_h \tag{1.28}$$

An evaluation of the correction reveals that the higgs mass is sensitive to loop corrections from heavy particles. At loop level contributions from fermions and bosons, see figure 1.2, are given by [16]:

$$\Delta m_h = -\frac{|\lambda_f|}{8\pi^2}\Lambda_{UV}^2 \qquad\qquad \text{for fermions} \tag{1.29}$$

$$\Delta m_h = \frac{\lambda_S}{16\pi^2}\left(\Lambda_{UV}^2 - 2m_S^2\ln\frac{\Lambda_{UV}}{m_S}\right) \qquad\qquad \text{for bosons} \tag{1.30}$$

where λ_f denotes the higgs-fermion-fermion triple coupling and λ_S the higgs-higgs-boson-boson quartic coupling constants. Λ_{UV} represents an ultraviolet cut-off from previous integrations, which marks the validity range of the SM. In the absence of physics beyond the standard model (BSM) this cut-off is given by the Planck mass $M_{pl} \approx 1 \cdot 10^{19}$GeV, where effects of quantum gravity need to be taken into account.

For fermions only the top fermion contributes significantly and the leading order contributions from equation 1.29 and 1.30 can be summarized by [27]:

$$\Delta m_h^2 = \frac{3 \cdot \Lambda^2}{8 \cdot \pi^2 v^2}\left(m_h^2 + 2m_W^2 + m_Z^2 - 4m_t^2\right) \tag{1.31}$$

It can be seen that the bare Higgs mass needs to be about 20 orders of magnitude grater than the measured value to cancel the corrections except for the comparably tiny measured higgs mass, if no BSM physics emerges up to the Planck mass. One may argue that the value of m_0 is not restricted within the theory and thus no contradictions exist. Theories which require a *fine-tuning* of the parameters lack a certain *naturalness* and the presented instability of the higgs mass is often referred to as the *higgs hierarchy problem*. Several theories were proposed to fix this problem of the SM, among them are theories with large spatial extra dimensions, like the ADD model studied in this thesis. Additional dimensions could lower the fundamental Planck scale down to $\mathcal{O}(1 - 10\text{TeV})$, which would lower the terms $\propto \Lambda_{UV}$ in equations 1.29,1.30 enough to reach an acceptable fine tuning within the theory. Another popular approach to solve the hierarchy problem are supersymmetric extensions of the SM (SUSY), where a SUSY partner boson (fermion) exists for every SM fermion (boson). The SUSY particle couples with the same strength to the higgs field as the SM particle resulting in a cancellation for terms in equations 1.29, 1.30[13].

---

[13]The logarithmic term in equation 1.30 can be treated during the renormalization [16].

2. Quantum Gravity and Large Extra Dimensions

2.1. An Effective Theory of Quantum Gravity

The standard model of particle physics does not include the effects of gravity. Yet it is possible to quantize the gravitational fields in an approach similar to the quantization of Yang-Mills theory, using the canonical quantization first developed by de Witt and Feynman, together with the background field method by 't Hooft and Veltman [28, 29, 30]. Starting from the Einstein-Hilbert action for a gravitational field with matter density $\mathcal{L}_m$:

$$S = \int d^4x \mathcal{L}_m = \frac{2}{\kappa^2} \int d^4x \sqrt{-g} R \tag{2.1}$$

with Ricci scalar R, determinant g of the metric local tensor $g_{\mu\nu}(\vec{x})$ and a constant $\kappa^2 = 32\pi G_N$, where G_N denotes the gravitational constant. The metric tensor is divided into a quantum field $h_{\mu\nu}$ on top of a flat background field $\eta_{\mu\nu} = diag(1, -1, -1, -1)$:

$$g_{\mu\nu} = \eta_{\mu\nu} + \kappa h_{\mu\nu} \tag{2.2}$$

It is now possible to expand the linearized Lagrangian in terms of the quantum field [31]:

$$\frac{2}{\kappa^2} \sqrt{-g} R = \frac{1}{2} (\partial^\mu h^{\nu\rho} \, \partial_\mu h_{\nu\rho} - \partial^\mu h \, \partial_\mu h - 2 \cdot h^\mu \, h_\mu + 2 \cdot h^\mu \, \partial_\mu h) + \mathcal{O}(\kappa) \tag{2.3}$$

To complete the quantization one may solve the path integral over all possible paths which result in the same final states [28]:

$$Z = \int dh_{\mu\nu} \, \delta(G_\alpha(h)) \, det|\frac{\partial G_\alpha}{\partial \epsilon_\beta}| \, e^{iS} \tag{2.4}$$

it is necessary to choose a fixed gauge constraint $G_\alpha(h)$ and the term $\frac{\partial G_\alpha}{\partial \epsilon_\beta}$ refers to infinitesimal gauge transformations [28]:

$$x'^\mu = x^\mu + \epsilon^\mu(x) \qquad \epsilon \ll 1$$
$$h'_{\mu\nu}(x') = h_{\mu\nu}(x) - \partial_\mu \epsilon_\nu - \partial_\nu \epsilon_\mu$$

The resulting fields can be reordered to obtain the equation of motion for a massless spin-2 particle which couples directly to matter after subtraction of Feynman-DeWitt-Fadeev-Popov ghost fields[1]. The interaction with external fields is mediated by the coupling of the graviton to the energy momentum tensor. An example for this procedure together with representations for the one and two graviton vertices and the energy momentum tensor

---

[1]The gauge fixing is arbitrarily set, and paths, which are equal under gauge transformations are counted multiple times. The resulting non-physical fields are denoted ghost fields

can be found in [28]. It should be noted, that the modelling of the effective field theory showed no conceptual differences to the quantization of Yang-Mills theory (see. [13] for a generic description of Yang-Mills quantization) until this point. Problems with the presented approach arise when one tries to renormalize the theory. The terms at a given order contain higher order derivatives of the field. This structure makes it impossible to renormalize all orders with a single running coupling constant. Yet it is possible to perform a renormalization up to a certain order [28]. In conclusion it is possible to derive a non-renormalizable effective quantum theory of gravity using common approaches for the quantization of a classical field theory, which is able to give direct predictions for quantum gravity corrections beneath the Planck scale.

2.2. Large Extra Dimensions & The ADD Model

Inspired by ideas from string theory **A**rkani-Hamed, **D**imopulus and **D**vali proposed the ADD theory as an attempt to solve the Higgs mass hierarchy problem [15]. The ADD model extends the Kaluza-Klein theory with a couple of additional assumptions:

- All standard model fields are confined to a 4 dimensional brane which is embedded in the (4+n) dimensional space-time called bulk. In the following general coordinates in the bulk $z(x, y)$ will be separated in the 4 dimensional coordinates on the brane x and the remaining n bulk coordinates y. With Indices $\hat{\mu}, \hat{\nu} \in (1, ..4 + n)$ for the general coordinates and $\mu, \nu \in (1, ..4)$ $i, j \in (5, ..4 + n)$ for the brane and remaining coordinates respectively. Fields in the bulk are also marked with an additional hat.

- Gravity can propagate in all dimensions

- The surface-tension of the brane is expected to be small. This assumes that the (4+n) dimensional metric $g_{\hat{\mu}\hat{\nu}}$ is flat for distances $L \ll \frac{1}{M_{pl}^{(4+n)}}$ [32]. This requirement reflects that effects from the dynamic between brane and bulk are neglected.

- All extra dimensions are assumed to be compactified on a torus with common Radius R. This assumption relates the four dimensional Planck mass irectly to the radius of the extra dimension and the fundametnal Planck mass $M^{(4+n)}$ via $M_{pl}^2 = (2 \cdot \pi \cdot R)^n \left(M^{(4+n)}\right)^2$.

The formulation of the ADD fields follows the approach presented in section 2.1. Starting again from equations 2.1, 2.3 with the replacements $M_{pl} \to M_{pl}^{(4+n)}$. In addition variables and indices are marked with a hat symbol if they are replaced by their $(4 + n)$ dimensional counterpart (e.g. $\mu, \nu \to \hat{\mu}, \hat{\nu}$) :

$$\frac{2}{\hat{\kappa}^2}\sqrt{-\hat{g}}\hat{R} = \frac{1}{2}(\partial^{\hat{\mu}}\hat{h}^{\hat{\nu}\hat{\rho}}\partial_{\hat{\mu}}\hat{h}_{\hat{\nu}\hat{\rho}} - \partial^{\hat{\mu}}\hat{h}\partial_{\hat{\mu}}\hat{h} - 2\hat{h}^{\hat{\mu}}h^{\hat{\mu}} + 2\hat{h}^{\hat{\mu}}\partial_{\hat{\mu}}\hat{h}) + \mathcal{O}(\kappa) \qquad (2.5)$$

following [31] it is now possible to impose the de Donder gauge condition

$$\partial^{\hat{\mu}}(\hat{h}_{\hat{\mu}\hat{\nu}} - \frac{1}{2}\eta_{\hat{\mu}\hat{\nu}}\hat{h}) = 0 \qquad (2.6)$$

2. Quantum Gravity and Large Extra Dimensions

to derive the equation of motion using the $(4+n)$ dimensional D'Alambertian:

$$\Box_{4+n}(\hat{h}_{\hat{\mu}\hat{\nu}} - \frac{1}{2}\eta_{\mu,\nu}\hat{h}) = 0 \tag{2.7}$$

the quantum field $\hat{h}_{\hat{\mu}\hat{\nu}}$ can be decomposed into [31]:

$$\hat{h}_{\hat{\mu}\hat{\nu}} = V_n^{-\frac{1}{2}} \begin{pmatrix} h_{\mu\nu} + \eta_{\mu\nu}\,\phi & A_{\mu i} \\ A_{\nu i} & 2\phi_{ij} \end{pmatrix} \tag{2.8}$$

with the volume of the compactified dimensions V_n. The new fields can be expanded in their modes:

$$\zeta_{\alpha\beta} = \sum_{\vec{k}} \zeta_{\alpha\beta}^{\vec{k}} \exp \frac{2\pi i \vec{k} \cdot \vec{y}}{R}, \qquad \vec{k} = (k_1, \ldots, k_n) \tag{2.9}$$

where $\zeta_{\alpha\beta}$ represents $h_{\mu\nu}$, $A_{\nu\mu}$ or $\phi_{i,j}$.

A redefinition of the fields is necessary to derive the physical fields $\tilde{h}_{\mu\nu}, \tilde{A}_{\mu\nu}, \tilde{\phi}_{\mu\nu}$. This redefinition is related to a spontaneous symmetry breaking of a geometric symmetry [31] and the fields can be reorganised to one massive spin-2 particle, $(n-1)$ massive vector bosons and $\frac{n(n-1)}{2}$ massive scalar bosons per KK-mode. To study the coupling of the KK states to ordinary matter one can use the already introduced canonical quantization of the $3+1$ dimensional Einstein-Hilbert action for the SM Lagrangian on the induced metric:

$$\mathcal{S} = \int d^4x \sqrt{-g}\, \mathcal{L}(\hat{g}, SM) \tag{2.10}$$

where g is the induced 4-D metric $g_{\mu\nu} = \kappa(h_{\mu\nu} + \eta_{\mu\nu}\phi)$ and $\phi = \phi_{ii}$ the trace of the field ϕ. The action can be expanded for $\kappa \ll 1$ in first order using:

$$\sqrt{-g} = 1 + \frac{\kappa}{2}h + 2\kappa\phi$$
$$\hat{g} = \eta^{\mu\nu} - \kappa h^{\mu\nu} - \kappa\eta^{\mu\nu}\phi$$

switching to the physical fields $\tilde{h}_{\mu\nu}, \tilde{\phi}_{\mu\nu}$ and using the definition of the energy-momentum tensor $T_{\mu\nu}$ as it is worked out in [31]:

$$T_{\mu\nu} = \left(-\eta_{\mu\nu}\mathcal{L} + 2\frac{\delta\mathcal{L}}{\delta g^{\mu\nu}}\right)_{g=\eta}, \tag{2.11}$$

one can derive the final formulation for the action:

$$\mathcal{S} = -\kappa \sum_{\vec{k}} \int d^4x (\tilde{h}^{\mu\nu,\vec{k}}\, T_{\mu\nu} + \omega\,\tilde{\phi}^{\vec{k}}\, T^{\mu}{}_{\mu}) \tag{2.12}$$

where the vector boson modes completely decouple from the SM fields and scalar modes (dilaton modes) couple only through their trace. The dilaton contributions are neglected in the following as suggested in [32], where it is pointed out, that the trace of the energy-momentum tensor vanishes for conformal theories when the equations of motion are imposed.

14

The mass gap between the graviton modes is given by [32]:

$$\Delta m = \frac{\Gamma(\frac{n}{2})(M_{pl}^{(4+n)})^{2+n}}{2\,\pi^{n/2}\,M_{pl}^2\,m^{n-1}} \tag{2.13}$$

For a choice of parameters in the energy region of interest ($n = 4 - 8$, $M_{pl}^{(4+n)} = 4\text{TeV}$, $m = 1\text{GeV}$) the mass gap ranges between $\mathcal{O}(10^{-15}eV) - \mathcal{O}(200eV)$. Thus it will not be possible to distinguish individual KK-modes with the current experimental resources, yet the sum of all modes can be observed as a non resonant-enhancement of the studied process [31]. This is illustrated in figure 2.1 where several KK-modes are shown on a flat background before and after a convolution with a Gaussian distribution. The Gaussian reflects the effects of a limited mass resolution where the mean corresponds to the central value of the graviton resonance and $\sigma = 1$ is chosen to simulate a realistic detector response. A comparison with figure 7.1 shows that the ADD spectrum produced with `PYTHIA8` fits well to this reduced description of the process.
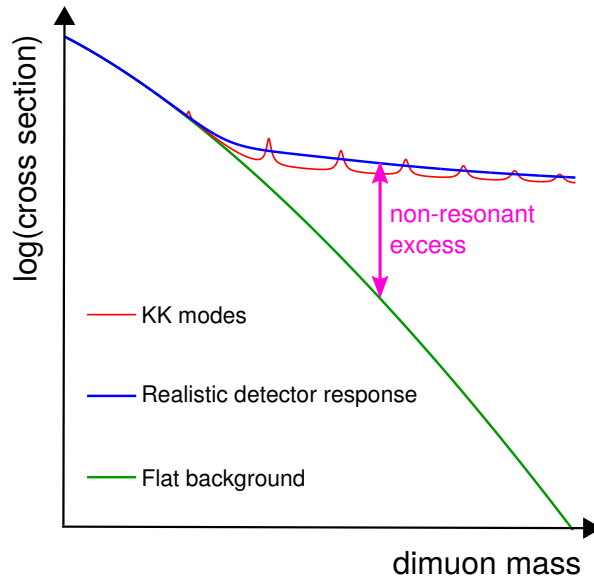
Figure 2.1.: Illustration of several KK-modes on a flat background.

2.2.1. Virtual Graviton Exchange

This thesis focusses on the s-channel exchange with a dilepton final state in quark-quark annihilation and gluon fusion. The corresponding Feynman graphs, together with the leading order Drell-Yan contributions are presented in figure 2.2. The brackets indicate the summation in the calculation of the matrix element. The initial and final states for the DY and ADD production in the quark-quark annihilation are the same, this makes it necessary to include interference effects between both graphs in cross sections calculations for the studied process. The scattering amplitude for the tree-level virtual graviton exchange can be expressed as [33]:

$$\mathcal{A} = S(s)\left(T_{\mu\nu}T^{\mu\nu} - \frac{T_\mu{}^\mu T_\nu{}^\nu}{n+2}\right) \tag{2.14}$$

2. Quantum Gravity and Large Extra Dimensions

where the function S denotes the sum over all KK-modes and s is the center of mass energy.
As pointed out in the last section the mass gap between the KK-modes is much smaller
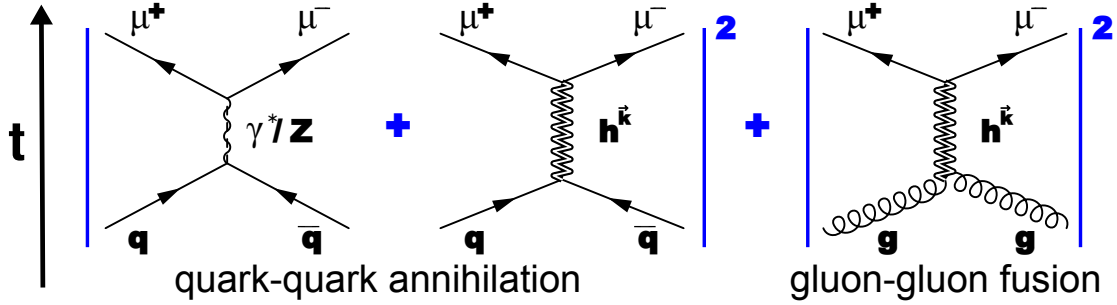
Figure 2.2.: Feynman graphs for SM LO Drell-Yan process and graviton exchange in quark-quark annihilation and gluon fusion. The brackets indicate the summation in the matrix-element for the process $qq \to ll$. Figure taken from [3].

than the experimental resolution and the summation in $S(s)$ can be replaced by an integral and solved using the narrow width approximation [33]:

$$S(s) = \frac{1}{M_{pl}^2} \sum_{\vec{k}} \frac{1}{s - m_{\vec{k}} + im_{\vec{k}} \Gamma_G(m_{\vec{k}})} \approx \frac{\pi^{n/2} \Lambda^{n-2}}{\Gamma(n/2)(M_{pl}^{(4+n)})^{2+n}} F_n\left(\frac{s}{\Lambda^2}\right) \tag{2.15}$$

It is necessary to introduce an ultraviolet cut-off Λ for more than one extra dimension, in order to deal with the divergence of the integral. This parameter is not fixed by the theory itself but it is assumed to be smaller than the fundamental Planck scale $M_{pl}^{(4+n)}$ [32]. The implementation in the available Monte Carlo (**MC**) simulation software `PYTHIA8` [34, 35] uses a low energy limit $s \ll \Lambda$ where equation 2.15 can be simplified to [33]:

$$S(s) = \begin{cases} \frac{\pi^{n/2}}{(1-n/2)\Gamma(n/2)} \frac{\Lambda^{n-2}}{\left(M_{pl}^{(4+n)}\right)^{2+n}} = \frac{4\pi}{\Lambda_T^4} & n > 2 \\ \frac{\pi}{\left(M_{pl}^{(4+n)}\right)^4} \ln\frac{s}{\Lambda^2} & n = 2 \\ \frac{-i\pi}{(M_{pl}^{(4+n)})^3 \sqrt{s}} & n = 1 \end{cases} \tag{2.16}$$

The approximation in equation 2.16 makes it possible to estimate the scattering amplitude with only one free parameter Λ_T for $n > 2$ [32, 33]. This is known as the GRW (Giudice, Rattazzi, Wells) parameter convention. The later results will also be interpreted in terms of the HLZ (Han, Lykken, Zhang) parameter convention, which is equivalent to the GRW convention except for the definition of the ultraviolet cutoff [36]. The results in the GRW convention depend not only on the cutoff M_s, called the string scale, but also on the number of additional dimensions, which makes a physical interpretation easier. Both conventions can be translated into each other for the case $n > 2$ via[3]:

$$\Lambda_T^4 = \frac{n-2}{2} M_s^4 \tag{2.17}$$

The case $n = 2$ is described in [31] and further discussed in section 11.

16

The squared Feynman amplitudes for the leading order contribution and the SM Drell-Yan interference terms can be found in [26]. The spin-2 graviton exchange and the interaction of spin 1-gluons in the gluon gluon interaction terms introduce new terms with an angular distribution different from the standard model Drell-Yan expectation. It is thus possible to use the angular distribution to differentiate a hypothetical non-resonant excess in the dilepton spectrum from other models with a similar signature, e.g. Unparticles [37] or contact interactions [38]. The spin structure for ADD and SM contributions is further studied in section 7.

Results from Previous searches

Torsion Balance Experiments The best current limits on Newton's law in the sub millimetre range are obtained with torsion balance experiments. The general principle for these experiments is to place a torsion pendulum with at least two test bodies close to a rotating attractor[2][39, 40]. The torsion of the pendulum is sensitive to local distortions of the gravitational field and is able to measure accelerations of a test body with relative precisions up to $\sim 10^{-13}$[40]. The results from torsion balance experiments are usually parametrized as limits on an additional Yukawa term in the gravitational potential caused by an additional massive boson:

$$V(r) = \frac{-G \cdot m_1 \cdot m_1}{r} \left(1 + \alpha e^{\frac{-r}{\lambda}} \right)$$

It was worked out in [41] that the first KK-mode dominates the contributions for deviations in the gravitational potential. The commonly used parameters can be identified with $\lambda = R$ and $\alpha = 8n/3$ [39], where R denotes the radius of the torodial compactified extra dimensions and n the number of extra dimensions. The radius for potential extra dimensions needs to be smaller than approximately $R \approx \frac{1}{\pi} 10^{-17 + \frac{32}{n}}$ cm, in order to lower the fundamental Planck scale $M_{pl}^{(4+n)}$ down to 1 TeV [39]. Such a scenario is assumed in figure 2.3 and it can be seen that scenarios with 2 extra dimensions are ruled out, and the limits can be expanded up to $M_{pl}^{(4+n)} \geq 3.2$ TeV [40]. The case $n = 1$ requires $R \sim \mathcal{O}(10^{15}$ m$)$ and is in contradiction to astrological observations [42]. Scenarios with $n = 3$ extra dimension would require values of $R \approx 3 \cdot 10^{-8}$ cm to lower the Planck scale down to 1 TeV and are far beyond the reach of current torsion balance experiments.

Collider Results Various searches have been performed with collider experiments until now, e.g. from all LEP experiment [49], the D0 experiment at the Tevatron [50] and most recently with the LHC experiments CMS [51] and ATLAS [52]. The most stringent lower limit is given by the ATLAS collaboration using 7 TeV data [52], where a combination of dielectron, dimuon and diphoton channels exclude $\Lambda_T < 3.4$ TeV. Results from these searches are further discussed in section 11.1 in the light of the results obtained by the search presented in this thesis.

Cosmological Constraints Several cosmological observations can be used to place limits on the fundamental Planck scale dependent on the number of extra dimensions. The most

---

[2]Great experimental effort is necessary to place the experiment in an electrical isolated vacuum and reduce electrostatic forces between components.
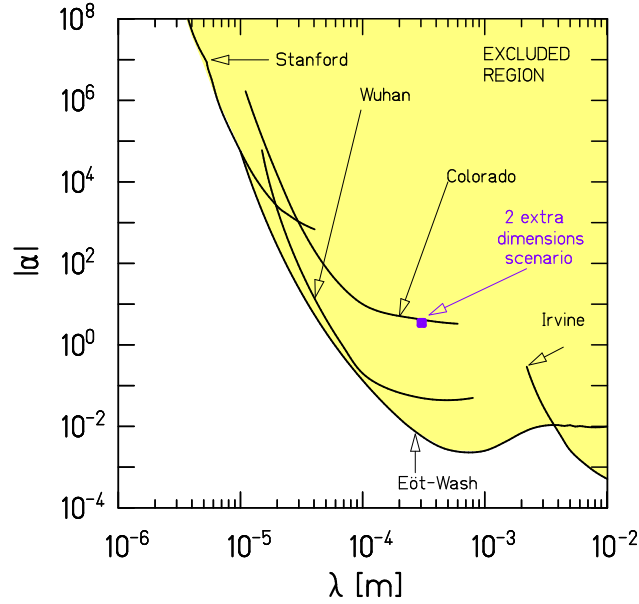
Figure 2.3.: Tests for Newton's inverse square law with torsion pendulum experiments. Distortions of the gravitational potential are parametrized as an additional Yukawa term $\alpha e^{\frac{-r}{\lambda}}$. Solid lines indicate results from the collaborations Eöt-Wash [40, 39, 43], Irvine [44, 45], Wuhan [46], Colorado [47] and Stanford [48]. Graphic adapted from [40].

stringent levels are found from supernova explosions and neutron star supernova remnants [53, 54]. The temperature in supernova cores can be sufficiently high to produce real graviton emission from light KK-modes dependent on the size of the extra dimensions. This would significantly change the supernova cooling process and thus decrease the emitted neutrino flux [53, 54]. Measurements of the supernova explosion SN1987A can be interpreted as limits on the fundamental planck scale $M_{pl}^{(4+n)} > 25(2.4)\,\text{TeV}$ for $n = 2(3)$ extra dimensions[54]. Most of the gravitons produced in a supernova explosion would be trapped inside the neutron star remnant. The decay of gravitons would therefore give additional excess heat via the decay $G_{KK} \to \gamma\gamma$, which would increase the observed surface temperature [53, 55]. Strong constraints $M_{pl}^{(4+n)} > 1700\,(76)\,\text{TeV}$ for $n = 2\,(3)$ extra dimensions are given in [53, 55] from observations of the neutron star PSR J0952+07. It should be noted that the calculation of neutron star heating by graviton decays and the measurement of neutron star surface temperatures struggle with large uncertainties compared to earth bound experimental searches. The exact numbers are uncertain within a factor of a few [55], yet it can be concluded that cosmological observations exceed the discovery potential of earth bound experiments if the number of extra dimensions is smaller than four.

3. Experimental Setup

The experimental data analysed in this thesis was recorded with the Compact Muon Solenoid (**CMS**) experiment at the Large Hadron Collider (**LHC**) particle accelerator, located at the *Organisation européenne pour la recherche nucléaire* (**CERN**) near Geneva, Switzerland. An aerial view on the CERN facilities is shown in figure 3.1 with the indicated position of the LHC. The CERN and its main experiment LHC is a global project and collaborators from more than 600 institutes contribute [56]. The resources of the Worldwide LHC Computing Grid (**WLCG**) are used to store, reconstruct and further process the measured detector signals in computing sites located in 36 countries around the world.

Figure 3.1.: Aerial view on the CERN facilities with the position for the LHC and the main experiments ALICE, ATLAS, CMS and LHCb drawn upon. Picture taken from [57].

3.1. Large Hadron Collider

The Large Hadron Collider is a circular particle accelerator for proton-proton and heavy ion collisions with a maximum design center of mass energy of $\sqrt{s} = 14\,\text{TeV}$ for proton proton interactions [58, 59]. This thesis uses only data from proton-proton collisions and the following description will focus on aspects of the LHC relevant for this case. The LHC is located underground in a circular tunnel with a circumference of 27 km and accelerates bunches of $\sim 10^{11}$ protons in two beam-pipes. The protons are accelerated up to an energy of 450 GeV in the acceleration chain consisting of Linac2, Proton Synchrotron Booster (PSB), Proton Synchrotron (PS), and Super Proton Synchrotron (SPS) before injection into the LHC main ring [59]. Both beams are accelerated in opposite directions and brought to collision at four interaction points which are surrounded [1] by the experiments ALICE [60], ATLAS [61], CMS and LHCb [62]. ATLAS and CMS are designed as multi-purpose particle detectors. ALICE is designed to measure heavy ion collisions while LHCb focuses on B meson production. The beams are bent onto their trajectory by 1 232 superconducting dipole magnets with a field strength up to 8.3 T. In addition several thousand correction and focusing magnets are installed around the ring to modulate the beam properties. The magnets are made of niobium-titanium Rutherford cables and rely on a continuous cooling with fluid helium at temperatures of 1.9 K to preserve the superconductivity at high currents. The key performance parameter for a particle accelerator is its integrated luminosity $\mathcal{L}$, it serves as a normalization factor between the measured number of events N and theoretical predictions in the form of cross sections σ for a process:

$$N = \mathcal{L} \cdot \sigma \tag{3.1}$$

Thus the probability to produce a rare process rises linearly with the luminosity. Assuming relativistic particle velocities and head-on collisions of gaussian shaped beam profiles one can describe the luminosity for a circular particle collider by:

$$\frac{d\mathcal{L}}{dt} = \frac{N_p^2 \cdot n_b \cdot c}{4\pi \cdot \sigma_x \cdot \sigma_y \cdot l} \tag{3.2}$$

where l is the circumference of the ring, c the speed of light, N_p the number of particles per bunch, n_b the number of bunches per beam direction and σ_x, σ_y the standard deviations of the normal distributions describing the beam area transverse to the beam direction. In 2012 the LHC reached peaks in the instantaneous luminosity up to $7.7\,\text{nb}^{-1}/\text{s}$ [63]. The search presented in this thesis uses the complete dataset recorded at $\sqrt{s} = 8\,\text{TeV}$ during Run I in 2012. The LHC outperformed most of its goals during this data taking period and delivered an integrated luminosity of $23.3\,\text{fb}^{-1}$ at the CMS detector, see figure 3.2.

---

[1] At least in parts, LHCb uses an asymmetric geometry.

CMS Integrated Luminosity, pp
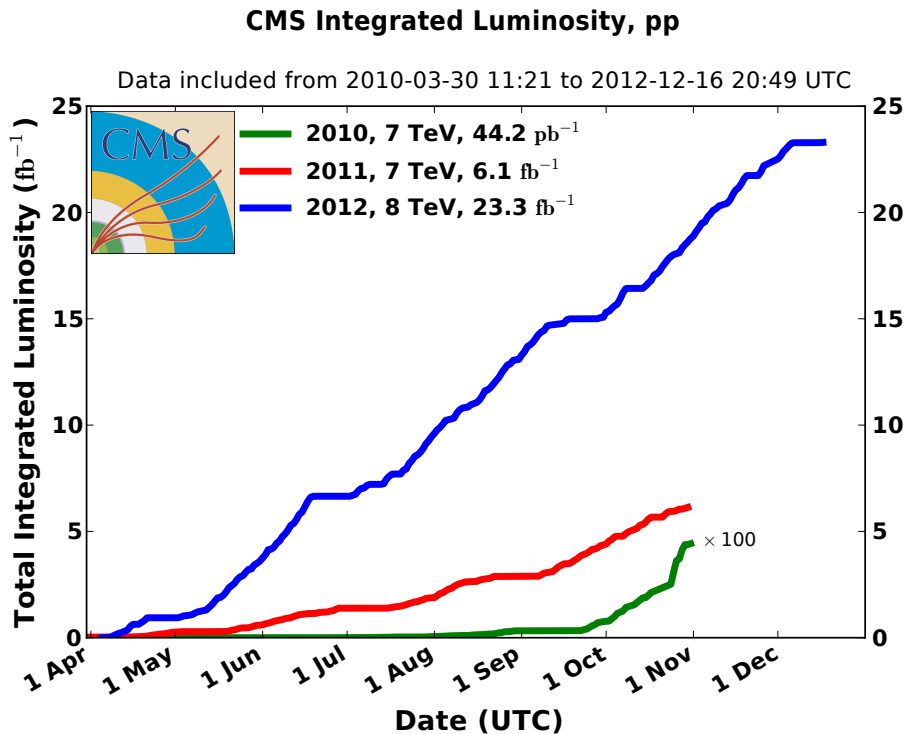
Figure 3.2.: Integrated luminosity for the three data taking periods in 2010, 2011 and 2012 at the CMS detector. Picture taken from [64]

3.2. Compact Muon Solenoid

The CMS experiment [65] is designed as a general purpose particle detector. It combines several systems for calorimetry and track measurements to identify and measure several particles within an event[2] together with global detector properties of the event.

CMS has a cylindrical shape with a length of 22 m and a diameter of 14 m. Momenta of charged particles are measured by their bending in a magnetic field, which is provided by a superconducting solenoid magnet with an almost uniform magnetic field of 3.8 T. The solenoid is made of a 4 layer winding using reinforced NbTi cables, which are cooled with liquid nitrogen. The magnetic field flux outside the coil is controlled by an 10 000 t iron yoke. A schematic cutaway view of the CMS detector can be seen in figure 3.3. CMS is separated into a barrel region (subdivided into five wheels) and two endcap regions. All detector components surround the interaction point in an onion-like geometry. The pixel track detector is installed closest to the interaction point followed by the strip-tracker, electro-magnetic calorimeter (ECAL), hadronic calorimeter (HCAL), solenoid and muon system. This thesis depends on the precise reconstruction of highly energetic muons, where the calorimeters play only a minor part. The following description will therefore describe ECAL and HCAL only briefly and focus on the relevant detector parts for muon track measurements: tracker and muon system.

---

[2]In the following an event will denote either a bunch crossing which produced a triggerable interaction or the measured data for a such an interaction.

CMS DETECTOR

Total weight	: 14,000 tonnes
Overall diameter	: 15.0 m
Overall length	: 28.7 m
Magnetic field	: 3.8 T

STEEL RETURN YOKE
12,500 tonnes

SILICON TRACKERS
Pixel (100x150 μm) ~16m² ~66M channels
Microstrips (80x180 μm) ~200m² ~9.6M channels

SUPERCONDUCTING SOLENOID
Niobium titanium coil carrying ~18,000A

MUON CHAMBERS
Barrel: 250 Drift Tube, 480 Resistive Plate Chambers
Endcaps: 468 Cathode Strip, 432 Resistive Plate Chambers

PRESHOWER
Silicon strips ~16m² ~137,000 channels

FORWARD CALORIMETER
Steel + Quartz fibres ~2,000 Channels

**CRYSTAL
ELECTROMAGNETIC
CALORIMETER (ECAL)**
~76,000 scintillating PbWO₄ crystals

HADRON CALORIMETER (HCAL)
Brass + Plastic scintillator ~7,000 channels

Figure 3.3.: Cutaway view of the CMS detector, taken from [66].

3.2.1. CMS Coordinate System

The coordinate system adopted by CMS has its origin at the nominal interaction point [65]. The x-axis points towards the center of the accelerator ring, the y-axis upwards in the detector cavern and the z-axis in the direction of the beam (pointing towards the Jura mountains western of the cavern). Two coordinates are defined in the xy plane: the radial coordinate r and the azimuthal angle ϕ measured from the x-axis. The polar angle is defined in the r-z plane and substituted by the pseudorapidity $\eta = -\ln\tan(\theta/2)$. This is motivated by the fact that the pseudorapidity is equal to the particle rapidity ψ, $\tanh\psi = v_z/c$ in the high energy limit $m \ll E$, where v_z denotes the particle velocity in z direction.

3.2.2. Calorimeters

CMS incorporates an electro magnetic and a hadronic calorimeter to measure the energy deposited by particles while traversing the detector [65]. Both calorimeter systems use scintillation light produced by the particles and cover enough radiation lengths for electro magnetic and hadronic processes to ensure that almost all particles (except for muons and neutrinos) deposit their complete energy within the detector [65]. The complete knowledge about all energy deposited can be used to determine global event parameters, e.g. the missing

transverse energy [67][3].

ECAL

Electromagnetic calorimetry is an essential part for the reconstruction of electrons and photons. It also helps to improve the measurement of hadronic jets with a strong electro magnetic component. The ECAL is divided into a barrel region ($|\eta| < 1.479$) and two endcap discs at each site of the detector, which cover a region up to $|\eta| < 3.0$.

A particle traversing the detector creates scintillating light in several of the 75,848 lead tungstate $PbWO_4$ crystals[4] proportional to the deposited energy. The scintillating light is measured with avalanche photo-diodes in the barrel and a mixture of avalanche photo-diodes and -triodes in the endcap regions. The material budget covers up to 25 radiation lengths[5] X_0 around the interaction point. Studies with test beams show that the ECAL energy resolution can be parametrized by a stochastic, noise and constant term:

$$\frac{\sigma(E)}{E} = \frac{2.8\%}{\sqrt{E(\text{GeV})}} \oplus \frac{12\%}{E(\text{GeV})} \oplus 0.3\% \tag{3.3}$$

The constant term increases due to limited accuracy in monitoring temperature, voltage and crystal transparency during the data taking. The energy resolution studied with $Z \to ee$ events during the 2012 data taking period and ranges between 1.5% to 5% depending on η, see figure 3.4, this and additional performance results can be found in [68].

HCAL

The hadronic calorimeter [69, 65] (HCAL) is designed to measure the deposited energy and direction of flight for hadronic jets. It is divided into the four subsystems: hadron barrel (HB), endcap (HE), outer (HO) and forward (HF). Barrel and endcap systems are located within the solenoid. The subsystems are further divided into smaller wedge shaped blocks (HCAL towers) which use a sandwich structure of brass absorber and scintillating plastic tiles. The scintillation light is read and summed up using optical fibres. The number of covered hadronic radiation lengths[6] λ_I varies in different η-regions with a minimum of 11.8 λ_I.

Hard interactions in a proton collider are often accompanied by one or more hadronic jets, see section 1.2.2. A precise measurement of jets is thus not only important for dedicated jet analyses, but also plays a key role in the reconstruction of global event parameters.

The jet p_T resolution was studied using the imbalances in the transverse plane for dijet events [70], see figure 3.4.

3.2.3. Track Detectors

The trajectories of charged particles (tracks) are measured in the inner tracking system and muon system. The inner tracker consists of silicon pixel and strip detectors. With an active

---

[3]The missing transverse energy is defined as the sum of all particle momentum vectors projected on the transverse plane

[4]61200 in the barrel and 7324 in each endcap.

[5]The radiation length is defined as the average distance a electron travals until its energy is reduced to $1/e$ of the inital value.

[6]The hadronic interaction length λ_I is defined as the average distance between two strong interactions.
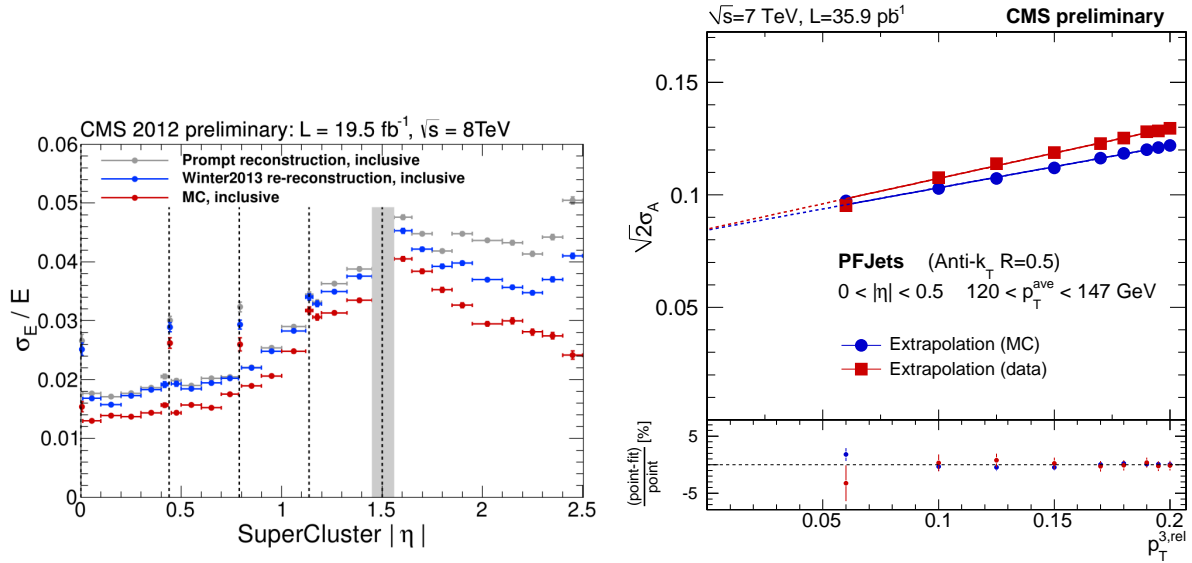
Figure 3.4.: Left: ECAL energy resolution measured with $Z \rightarrow ee$ events during 2012, picture taken from [68]. Right: Jet energy resolution measured by momenta imbalances in the transverse plane for dijet events $p_T^{ave} = p_T^{Jet1} + p_T^{Jet2}$ during 2011 at $\sqrt{s} = 7\,\text{TeV}$, where $\sqrt{2}\sigma_A = \sigma(p_{T,jet})/p_{T,jet}$. The resolution is shown for a average imbalance $120\,\text{GeV} < p_T^{ave} 147\,\text{GeV}$ dependent on the soft activity in the dijet event, which is estimated with $p_T^{3,rel} = p_T^{Jet3}/p_T^{ave}$. Picture taken from [70].

silicon area of around $200\,\text{m}^2$ it is the largest silicon based tracker built yet. Outside the calorimeters (and in parts outside the yoke) multiple systems are installed to measure high energetic muons which traverse the whole detector. These detectors are referred to as the muon system. The material budget installed in front of the muon system is high enough to ensure that only a small fraction of the muon system signals stem from a particle other than a muon.

Inner Tracker

The inner tracker surrounds the interaction region for distances $4.4\,\text{cm} - 116\,\text{cm}$ covering a region up to $|\eta| < 2.5$. The inner tracker is further subdivided into a silicon pixel and a silicon strip detector. The pixel detector consists of $1\,440$ pixel modules arranged in three pixel layers in the barrel region and 2 discs on each endcap. A cut-away view into the tracker is shown in figure 3.5. Each pixel has a size of $100\,\mu\text{m} \times 150\,\mu\text{m}^2$ in $r - \phi$ and z direction respectively. In total the pixel detector covers an area of $1\,\text{m}^2$ using around 66 million pixels. In addition to track measurements it is also used to determine the luminosity during data taking, the procedure is further discussed in section 8.1.1.

Distances between $20\,\text{cm} - 116\,\text{cm}$ are covered with $15\,148$ strip modules. The strip modules consist of single silicon strips with varying size of typically $10\,\text{cm} \times 80\,\mu\text{m}$.

Pixel and strip tracker use the same principle to measure tracker hits: a pair of connected p-doted and n-doted semiconductors operated with reverse voltage create a depletion zone with only few free charge carriers between them. Free charges created by ionizing radiation

within the depletion zone lead to peaks in the current between the semiconductors and can be used to identify a hit in a module.

A continuous cooling below $0°$ C,even between data taking periods, is crucial to reduce the effect of radiation damage in the harsh conditions near the interaction points.

The event rates during data taking exceed the accessible computing and storage resources by orders of magnitude and it is necessary to quickly decide if an event should be saved for later analysis. Pre-reconstructed tracks in the inner tracker play a major role in the last steps of this so called triggering, see section 3.2.4. The tracking efficiency in the p_T range $(1 - 100)$ GeV was studied in 2012 by the CMS tracker group and showed to be close to 100% for the full η range [71]. Further description of the track reconstruction from single hits can be found in section 4.1.

TEC Endcap
9+9 disks

PXL
Pixel Detector
3 layers, 2+2 disks

TOB
Outer Barrel
6 layers

Tracker
Support
Tube

TIB
Inner Barrel
4 layers

TID
Inner Disks
3+3 disks

~2.4m
L~5.4m
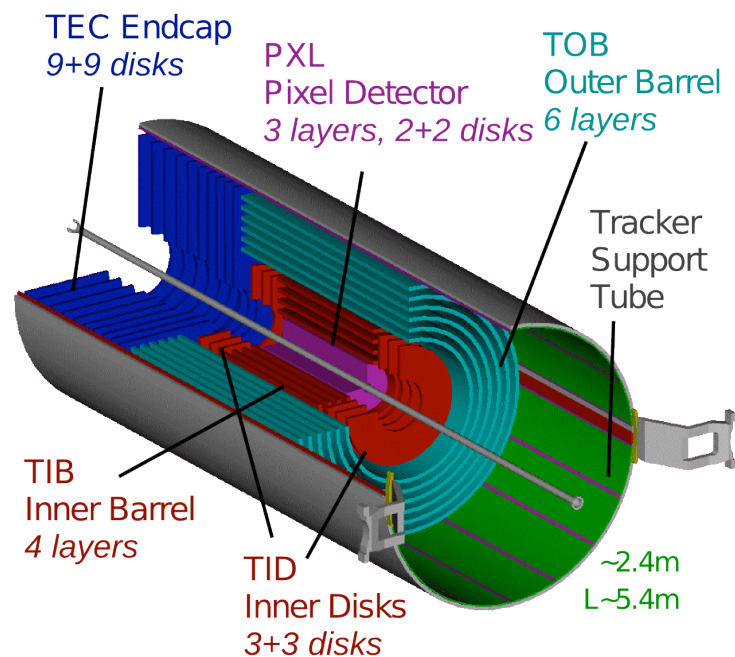
Figure 3.5.: Left: Scheme of the CMS inner tracker, picture taken from [71].

Muon System

The higgs decay $H \to ZZ \to 4\mu$ was among the so called "golden" channels for a higgs discovery and its clear signature with almost no background was one of the key elements to establish the existence of a new particle [72]. In addition, signatures with high energetic muons are common in a wide range of theories beyond the standard model (e.g. ADD, SUSY). These examples show the relevance for precise muon measurements in the CMS physics program and its central importance is implied by the experiment's middle name. The CMS muon system [73, 65] was designed to fulfil these requirements using 3 types of gaseous detectors: drift tubes (DT), cathode strip chambers (CSC) and resisitive plate chambers (RPC).

A charged particle traversing a detector component produces ionized atoms or molecules and primary electrons from the gaseous active medium (e.g. $Ar + CO_2$ in DTs). The voltage

3. Experimental Setup

between cathode and anode element is set high enough to allow the creation of an avalanche by primary electrons. The resulting anode and cathode signal in multiple muon system elements (stations) can be used to reconstruct particle tracks. The material budget in front of the muon system exceeds 16 radiation lengths leading to only negligible punchthrough for non-muon particles and it covers the full region up to $|\eta| < 2.4$ without acceptance gaps[7]. Figure 3.6 shows the upper right quarter of CMS, it can be seen that the muon system is separated into 5 wheels in the barrel and 4 endcap disks on each side. All muon system
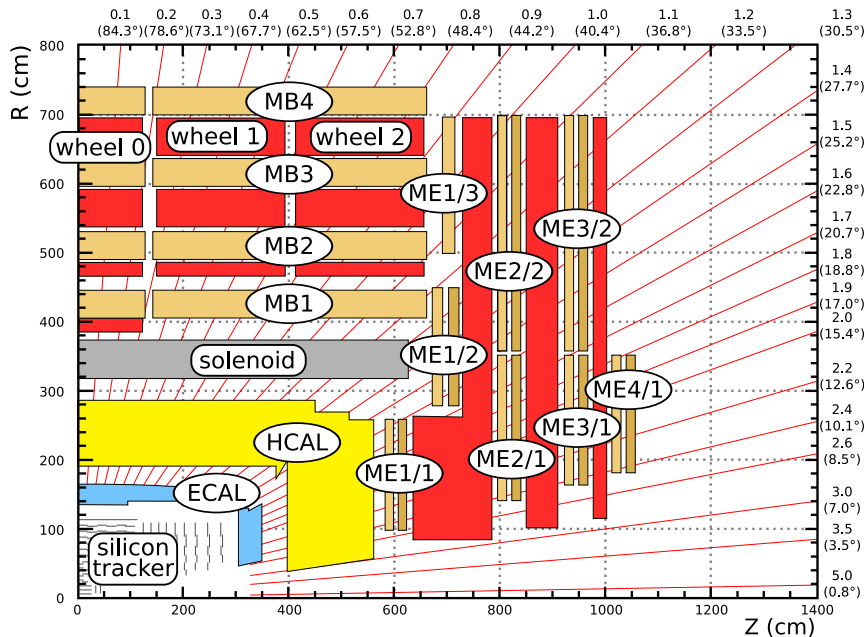
Figure 3.6.: Scheme of one quarter of the muon system, with labels for muon barrel stations (MB) in 3 wheels and muon endcap chamber (ME). Red lines indicate regions of same η [74].

detector components have a short response time and contribute in the first trigger stage, they are described briefly below:

Drift Tubes (DT): DTs are used in the barrel region, where the neutron induced background is low and the magnetic field is almost uniform. A DT contains several layers of drift cells. The cells are of rectangular shape with a cross section of $13 \times 42\,\mathrm{mm}^2$. Cathode strips and field shaping electrode strips are positioned on opposing sides and a 2.4 m anode wire is placed in the middle of the cell. A sketch for a single drift cell is shown in figure 3.7, together with lines where the time between initial ionization and anode signal is equal (isochrones). It can be seen, that the time of flight is approximately linear to the distance between primary ionization and anode wire. This additional timing information can be used to further improve the spatial resolution, once a track is associated with a bunch crossing. The single wire resolution is found to be better than $250\,\mu$m. Drift cells in each DT are

---

[7]The acceptance of a detector describes experimental restrictions to the kinematic properties within an event, e.g. p_T thresholds or detector parts shadowed by cabling.

positioned along the $r - \phi$ plane or in z direction to measure tracks with high precision in all angular directions.

Cathode Strip Chambers (CSC): CSCs are installed in both endcaps. During data taking the endcap regions have high muon rates, high background and non-uniform magnetic fields. CSCs fulfil the requirements of fast response time, fine segmentation and radiation resistance in these harsh conditions. Each CSC contains several layers of multiwire proportional chambers. Within a chamber cathode strips are installed along the r-direction while anode wires are installed with constant values[8] for r and θ. Cathode and anode strip signals are used to measure the direction in the r and ϕ plane, respectively. A single CSC is able to provide an off-line spatial-resolution between $75\,\mu\text{m} - 150\,\mu\text{m}$ with a 99% efficiency to find tracks in the first-level trigger, see section 3.2.4. The combination of several CSC layers ensures that muons are almost always matched to the correct bunch crossing.
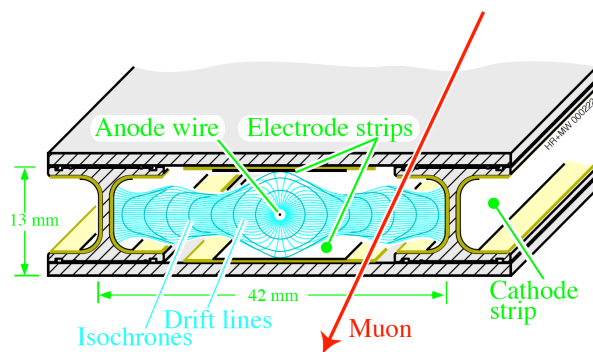
Figure 3.7.: Sketch of a drift cell with visualized drift lines and isochrones (lines where the time of flight is equal for primary electrons). Picture taken from [65].

Resistive Plate Chambers (RPC): RPCs are installed in both barrel and endcap region and serve as a dedicated muon triggering system. They consist of two cathode planes with a layer of anode strips installed between them. The signal distribution along the RPCs strips is used to determine the track position. Several layers of RPC can be used to produce a fast complementary p_T measurement with excellent time resolution. RPC hits are also used in later reconstruction stages.

3.2.4. Triggering and Data Acquisition

The collision rate inside CMS reached values up to $5 \cdot 10^8$ Hz in 2012 [75], which exceeds the available resources for data storage and processing by several orders of magnitude. It is thus necessary to quickly decide if an event is considered interesting and should be further processed and stored or discarded. CMS incorporates a dedicated triggering and data acquisition system (DAQ) [65] for this purpose, the structure of the system is shown in figure 3.8.

---

[8]Cathode wires are tilted at an additional angle close to the solenoid to corrects for changes in the drift velocity by the magnetic field.

3. Experimental Setup

The triggering process happens in two stages, first the level 1 (L1) trigger reduces the event rate to around 100 kHz using only basic information from calorimeters and muon stations in specially designed Application-Specific Integrated Circuits (ASICS) and more flexible Field Programmable Gate Arrays (FPGA). For muons basic track segments are constructed from several DTs and CSCs and combined with track candidates from RPCs found by matching pre-defined signal patterns to get a first p_T estimate. The processing time for this task is restricted to about $1\,\mu s$ per event. The single muon L1 trigger with the lowest p_T requirements was `SingleMu14`, with $p_T > 14 GeV$ [65]. A comparison for the triggering efficiency studied with Z events is shown in figure 3.9 dependent on p_T, η and ϕ for the 2011 and 2012 data taking period. It can be seen that the L1 triggers reached efficiencies up to 95% after turn-on effects close to the p_T threshold. This trigger is restricted to the region $|\eta| < 2.1$ as a compromise between a small p_T threshold and the high rates for large $|\eta|$. The drop of about 1% between 2011 and 2012 data can be explained by a new p_T assignment algorithm in the CSC track finder algorithm, which was necessary to keep the p_T threshold stable at significantly higher rates [76]. During 2012 L1 trigger rates of 100 kHz were further reduced to 400 Hz [77] in a second stage referred to as high level trigger (HLT). The HLT uses a computer farm located on the surface near the main detector to process events with a reconstruction similar to the one used in the off-line reconstruction and is able to use information from the inner tracking. This allows to perform a global muon fit combining muon candidates from inner tracker and muon system to get a reliable estimate of the muon p_T. The threshold on the muon p_T is adjusted to fit the available computing and storage resources of about 1 GB/s. The final event reconstruction is performed off-line using the WLCG, which is explained in the next section.
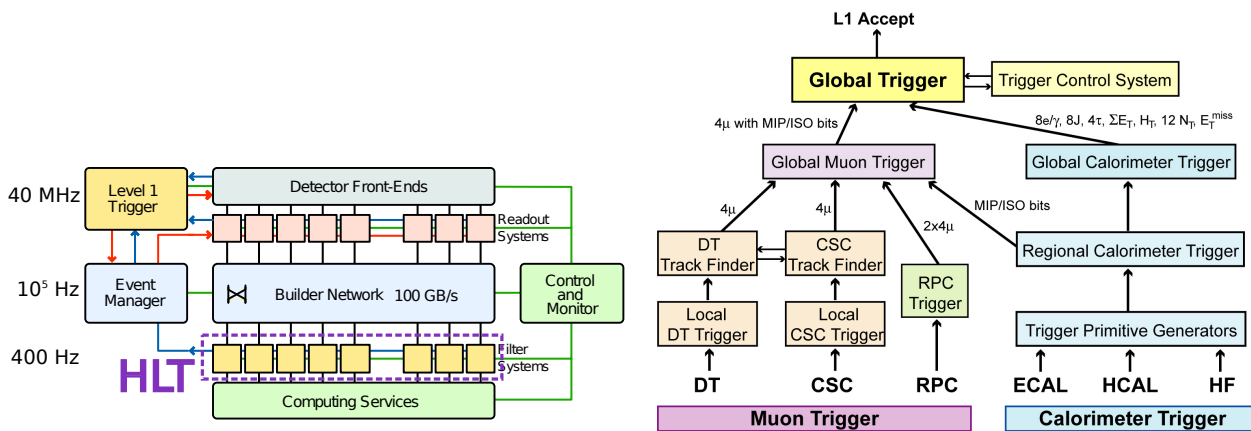
Figure 3.8.: Architecture of the DAQ sytem (left) and L1 trigger (right). Picture taken from [65].

28
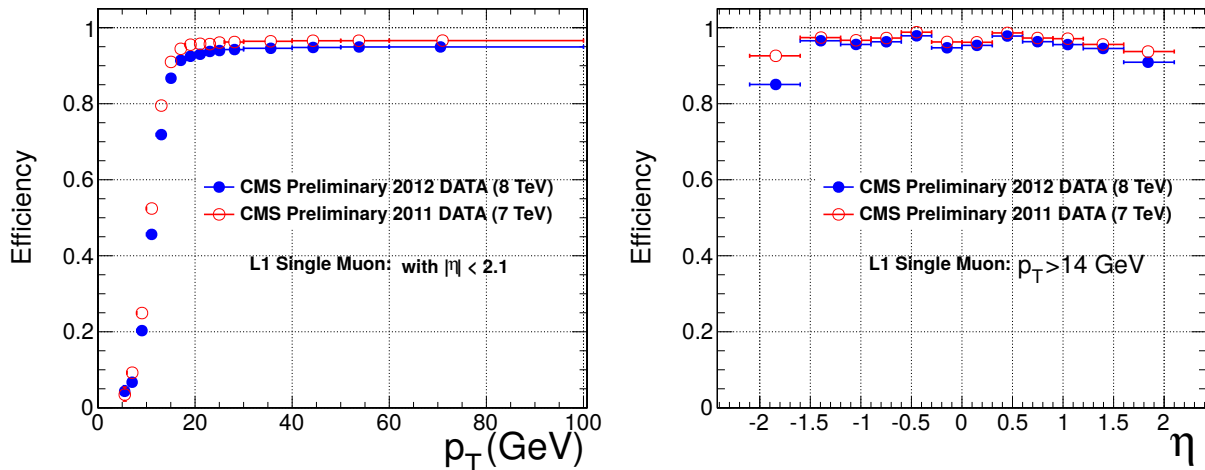
Figure 3.9.: Trigger performance for the L1 trigger `SingleMu14` in different η regions (upper row) and dependent on p_T (lower left) and ϕ (lower right). Graphics adapted from [76]

3.3. Computing Infrastructure and Software Framework

The data produced by the experiments is stored and further processed in the WLCG [78], also known as GRID. The GRID is organized in a hierarchical architecture with three main levels (Tiers), as shown in figure 3.10. The Tier0 center is located at CERN and stores the experimental data output directly to tape while a second independent copy is shared among 12 Tier1 sides in 11 different countries. Tier0 and Tier1 sites are connected by 10Gbit/s links which use special research networks[9] and the commercial networks of the world wide web. Tier-1 sites are also used to reconstruct measured data and provide computing time for event simulations including a full detector simulation when no new measurements are available. The last level consists of more than a hundred Tier2 sites which are dedicated to event simulations and physics analyses.

A detailed simulation of the detector is crucial in most physics analyses and a common software framework, CMSSW [80], is developed and used among CMS collaborators for this and other computational tasks. Within CMSSW events from Monte Carlo generators pass a complete detector simulation implemented in GEANT4 [81] to generate a digitized detector response in the same data format as it is used for recorded data. This allows to perform the event reconstruction with the same tools for both simulation and data. Within the Aachen CMS group, several analyses groups joined to develop the ACSUSYSkimmer [82], an application within CMSSW to perform the event reconstruction and create ROOT [83] n-tuples containing all relevant information for analysis with high level physics objects. This allowed to share datasets among analyses and reduces the CPU time and disk space requirements because sets are only reconstructed once and updated only once if changes in the reconstruction need to be applied. Most computing tasks in collider physics need to be repeated for a great number of events, where each event can be seen as independent. The ACSUSYSkimmer uses the resources of the GRID to run reconstruction tasks with up to

---

[9]e.g. the *Deutsches Forschungsnetz* `https://www.dfn.de`
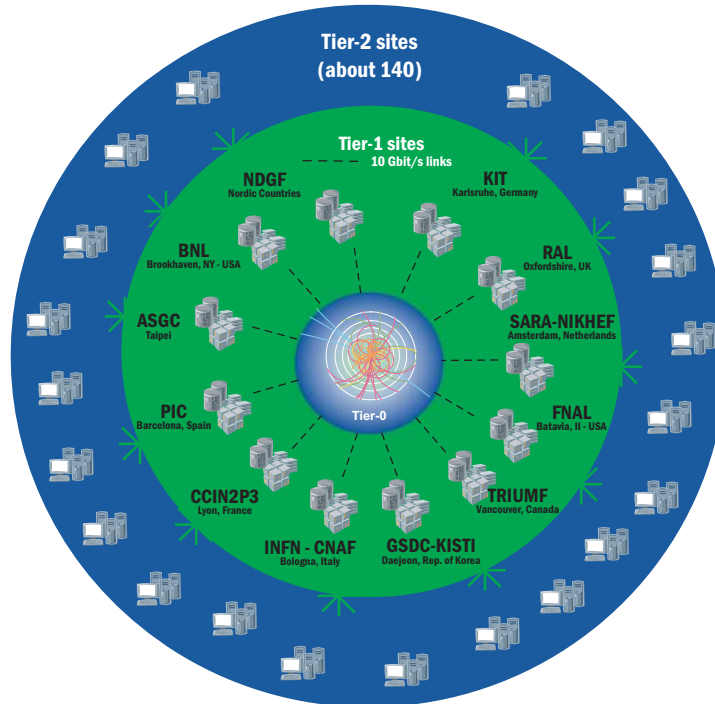
Figure 3.10.: Architecture of the WLCG with three levels (Tiers) [79].

several thousand CPU cores in parallel depending on the GRID utilization by other tasks. The necessary calculations for this thesis would have taken several decades of computing time on a single machine with currently available CPUs and could be finished within days using the GRID.

4. Muon Reconstruction

The CMS detector saves detector signals for all triggered events, as described in the last section. A reconstruction of high level physics objects is necessary to compare the measured data with theoretical predictions. This chapter starts with a short description of the general method to reconstruct tracks in CMS, followed by a brief introduction to the different muon reconstruction algorithms in CMS. The following analysis uses the TuneP method which combines all available algorithms.

4.1. Track Reconstruction

The tracks in CMS use the parameters $x, y, x', y', \lambda, q/p$ at a reference surface $z = z_r$ to describe the helix shape of a charged particle in a partly inhomogeneous magnetic field $\vec{B}(x, y, z)$. Here x', y' represent the derivative w.r.t z, λ the angle between magnetic field and the tangent to the trajectory and q/p the charge momentum ratio. This approach makes it possible to take distortions from the "free particle" trace due to energy loss in material and multiple scattering into account. The set of surface positions is limited to fixed distances from the beam axis with sensitive material. The reconstruction of tracks from hits in several detector regions can be described in four steps: seeding, trajectory building, trajectory cleaning and trajectory smoothing. Steps 2-4 represent an implementation of an extended Kalman filter algorithm with an intermediate cleaning of tracks taking into account the current progress in the track reconstruction. The Kalman filter is a bayesian minimum variance estimate for linear stochastic systems with a known state space, it is used as the last step in the standard reconstruction algorithms. As long as effects from multiple scattering and measuring uncertainties can be assumed to be gaussian, the result from the Kalman filter is equal to the maximum likelihood estimator, without requiring the computational complex inversion of large covariance matrices (a pedagogical introduction to Kalman filter techniques in the context of particle track fitting can be found in [84]).The exact implementation of the algorithm is explained in detail in [85] and will be described only briefly below:

Track seeding The seeding for muon objects uses a hit-based approach where a hit-pair or hit-triplet is used to reconstruct track seeds with a geometry which is compatible with the beam spot in the tracker. Muon DTs and CSCs build seeds based on patterns of one or more segments in the muon sub detectors based on rough geometric criteria [85]. For DT seeds with segments in MB1 or MB2 are assumed to be produced at the interaction point. A first estimate for the transverse momentum is calculated from the bending angle between vertex direction and matched muon station segments[1][85]. If the DT seed has only segments in MB3 and MB4 the difference in bending angle between segments in both stations is used to estimate p_T [85]. CSCs and overlap regions use the difference in ϕ direction between the first and second (or third) segment to estimate the candidate p_T [85].

---

[1]The average p_T is used if a track seed can be build from a MB1 and a MB2 segment [85].

Trajectory building The Trajectory finding and fitting is performed using a combinatorial Kalman filter algorithm with an intermediate cleaning stage. Starting from a track seed the algorithm calculates a probability density and the corresponding covariance matrix for the position of a hit on the next surface. This calculation includes the equation of motion and effects from scattering and energy loss in the detector material. This prior distribution is then updated with the information from a matching hit on the next surface. The resulting posterior distribution is used as the starting point for the next step.

Trajectory cleaning Ambiguities among all produced trajectories are resolved especially for tracks which share a large fraction of their hits while a maximum number of independent tracks is kept.

Trajectory smoothing The remaining tracks are again fitted stepwise, but this time from the outermost hit towards the primary vertex. This step can use the information from the complete covariance matrix gathered in the trajectory filtering step. The covariance matrix includes information about all following steps and allows to produce a robust result, where the influence from mismatched hits can be minimized.

4.2. Muon Reconstruction Algorithms

A set of muon reconstruction algorithms exists for different purposes: "tracker" and "standalone" algorithms reconstruct muon candidates only with information from the tracker or muon system, respectively, while the "global" algorithm combines information from tracker and standalone fits to fit the muon with hits from all parts of the detector [85]. Physics analyses are mainly interested in the particle properties close to the interaction point, and adding additional tracks and detector parts does not necessarily improve the quality of the fit. This can be explained by effects like electro-magnetic showering which may significantly alter the properties of high-p_T muons while traversing the detector. Special algorithms were developed to reduce the influence from such effects: the tracker-plus-first-muon-station (TPFMS) algorithm [86] uses only information from the tracker and the first muon station to reduce the effects from later occurring showers. A second approach is the "picky" algorithm [87] which ignores hits in stations with a high occupancy based on the χ^2/NDF between hit and previously reconstructed track, where the thresholds depend on the type of muon chamber. Finally the TuneP algorithm was developed to choose the best suited algorithm for each muon. The TuneP algorithms shows significantly better results compared to the other algorithms in studies with cosmic muons, see figure 4.1. The procedure to choose was adjusted in 2012 [88] and the most recent steps are summarized below [2]:

- It is first determined if the p_T measurement from the previously introduced algorithms is precise enough. The relative uncertainty $\frac{\delta p_T}{p_T}$ needs to be smaller than 0.25 for the result to be marked as valid. The algorithm with the smallest $\frac{\delta p_T}{p_T}$ is chosen to be valid and the threshold is lowered to $\left(\frac{\delta p_T}{p_T} \right)_{min} + 0.15$ for the other algorithm if no other algorithm fulfils the initial requirement.

---

[2]The description relies on the implementation in the CMSSW source code as it is currently not part of any official publication. Some information about the recent updates can be found in [88]

- The picky muon is the default choice and replaced by the tracker fit if the measurement is invalid.

- If tracker and picky are valid, the picky fit is used unless $P(picky) - P(tracker) > 17$, where P is defined as the negative logarithm of the probability to get the same or a smaller χ^2 for the reconstructed track:

$$P(\chi^2, NDF) = -\log\left(\int_0^{\chi^2} \frac{t^{\frac{NDF}{2}-1}e^{\frac{-t}{2}}dt}{\Gamma(\frac{1}{2}NDF)\cdot 2^{\frac{NDF}{2}}}\right)$$

- If neither picky nor tracker algorithms give valid results the TPFMS algorithm is chosen.

- Global muons are chosen if all other options give invalid results.

- If another algorithm than TPFMS is chosen, the choice is changed to TPFMS if $P(\text{chosen}) - P(\text{TPFMS}) > 40$, where P is defined as above.

- Low energy muons should always be reconstructed with the tracker because of the material budget up to the muon stations. If the selected algorithm up to this point or the tracker fit results in $p_T < 200\,\text{GeV}$ for the muon, the tracker fit is chosen.
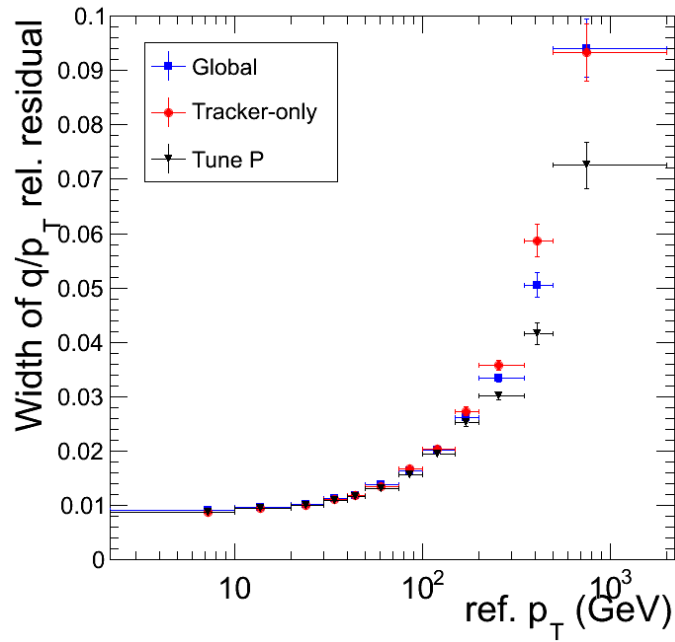
Figure 4.1.: Width of distribution of relative residuals for the lower and upper leg of a cosmic muon traversing the detector. Graphic taken from [89].

5. Event Selection

The selection of events with two high energetic muons happens in two stages. The observed muon rates during data taking are too high to save all events with two muons and a first selection happens during the data taking by the event triggering, see section 3.2.4. The applied triggering requirements for this search are discussed in the first part of this chapter. The online selected dataset is further analysed off-line, where more time is available for a detailed analysis of the detector signals. A set of cut based selection criteria is applied in the presented approach to obtain a sample which consists almost purely of irreducible background sources. The selection requirements are described in the second section of this chapter.

5.1. Trigger

The aim of this analysis is to find a non-resonant excess in the high mass tails of the invariant mass distribution for muon pairs, and contributions from events with small p_T muons are negligible. It is thus desirable to use a trigger with as loose requirements as possible to keep the sources of bias from the triggering to a minimum, even if this trigger has a relatively large p_T requirement. During 2012 the un-prescaled[1] single muon trigger with the lowest p_T threshold and no isolation criteria was `HLT_Mu40_eta2p1`. It had a rate of typically $21\,\text{Hz}$ with a p_T threshold of $40\,\text{GeV}$ [77], The acceptance in η is limited to $|\eta| < 2.1$ to reduce the data rate to an acceptable amount. The single muon trigger efficiency was studied in data events using the tag-and-probe method[2] in the Z region. The results are listed in table 5.1 for different η regions [91] together with data to simulation ratios. The measured single trigger efficiency translates into efficiencies of 97% or higher for events with two high-p_T muons. The trigger efficiency for dimuon events was studied with high mass simulations [92] and shown to be flat for masses up to $3\,\text{TeV}$ with values between 96% and 98%, see figure 5.1. The efficiency is about 1%-2% lower compared to the $7\,\text{TeV}$ search [3, 93]. Two effects are known which may cause this drop [92]. The triggering routines in CSC level 1 triggers changed to a new p_T assignment algorithm in 2012 which trades a $\mathcal{O}(1\%)$ loss in efficiency for a significantly reduced trigger rate [76, 92], as explained in section 3.2.4. The high level trigger introduced new cuts on the χ^2/NDF for the reconstruction and the longitudinal distance dz (see figure 3.7 for a description of dz) [92].

---

[1]For some triggers only every pf-th event is recorded to reduce the data rate. These triggers are referred to as prescaled triggers with prescale factor pf.

[2]see e.g. [90] for a description of the method

η-region	efficiency $\pm$ stat (%)	Data/MC ratio
$\lvert\eta\rvert < 0.9$	94.13 ± 0.02	0.98
$0.9 < \lvert\eta\rvert < 1.2$	84.27 ± 0.07	0.96
$1.2 < \lvert\eta\rvert < 2.1$	82.66 ± 0.05	0.99

Table 5.1.: Single muon efficiencies in data and data to MC ration for different eta regions estimated with the tag-and-probe method in the Z resonance [91].
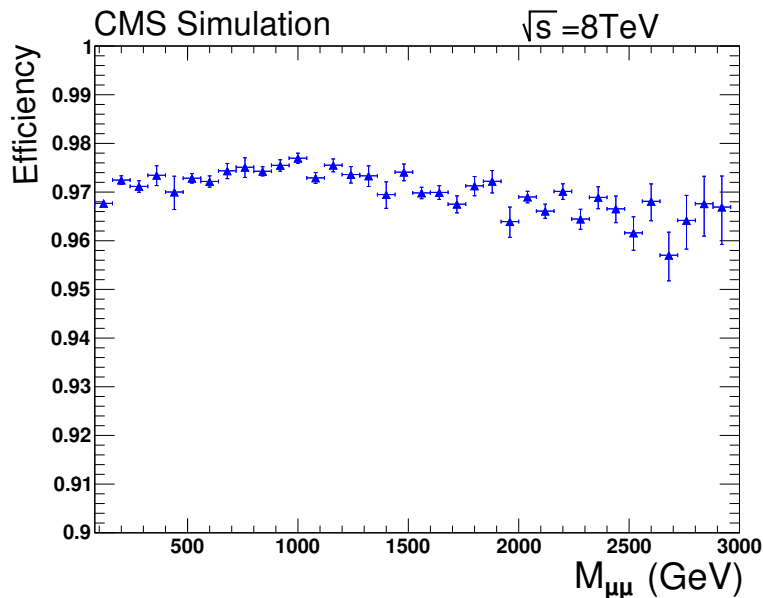
Figure 5.1.: Efficiency for the single muon `HLT_Mu40_eta2p1` HLT trigger for genuine dimuon events. This trigger is used in the following analysis. Picture taken from [92].

5.2. Cut Based Selection

Each event is required to pass a set of selection criteria developed by the CMS muon physics object group (POG[3]) with additional analysis specific cuts on the muon pair. If more than two muons fulfil the following criteria, the two muons with the highest p_T are chosen to calculate the invariant mass of the event. The used cuts are listed in table 5.2 and summarized below:

Primary Vertex: At least one well offline-reconstructed primary vertex is required. A well reconstructed vertex has at least 4 tracks associated to it being located within $\lvert z\rvert < 24\,\text{cm}$ and $\lvert r\rvert < 2\,\text{cm}$ of the nominal interaction point (IP). This cut helps to reduce the numer of events where a cosmic muon passes the tracker region of the detector during a bunch-crossing, misidentified as a muon pair.

Trigger Requirements The analysis uses the unprescaled single muon trigger with the

---

[3]Physics object groups (POGs) are formed within CMS to develop reconstruction and selection recommendations for physics objects in a centralized approach.

lowest p_T-threshold which does not impose any additional requirements for the muon isolation: `HLT_Mu40_eta2p1`, as described in 5.1. The acceptance is restricted to muons with $p_T > 40$GeV and $|\eta| < 2.1$. An additional offline cut $p_T > 45$GeV is applied to avoid influences from trigger-turn on effects. Within the analysis one of the selected muons is required to be reconstructed within the trigger acceptance and matched to the reconstructed muon trigger object within $\Delta R = \sqrt{\Delta\phi^2 + \Delta\eta^2} < 0.2$, while the second muon is allowed to be reconstructed up to $|\eta| < 2.4$.

Impact parameter The transverse impact parameter d_0 of the muon tracker-track w.r.t. the primary vertex needs to be smaller than 2 cm. The longitudinal distance is required to be $d_Z < 5$ mm, see fig. 5.2 for a sketch explaining the parameters d_0, d_Z.

Muon Reconstruction Each muon is required to be reconstructed as both a tracker and a global muon (see subsection 4.2). The relative error for the transverse momentum measurement $\delta p_T/p_T$ is required to be smaller than 0.3, based on the reconstruction.

Track quality Each muon is required to be reconstructed in all parts of the detector including: At least one valid pixel hit and more than five tracker layer hits in the global muon track fit. The reconstructed muon needs to be matched to segments in at least two muon stations.

Isolation Each selected muon needs to be isolated in order to reduce contributions from muons created in jets. A cut on the relative tracker isolation $\text{Iso}_{\text{trk,rel}} < 0.1$ is applied, where $\text{Iso}_{\text{trk,rel}}$ is defined as the sum of the transverse momenta of all tracks within a cone of $\Delta R < 0.3$ (excluding the muon track) divided by the p_T of the muon.
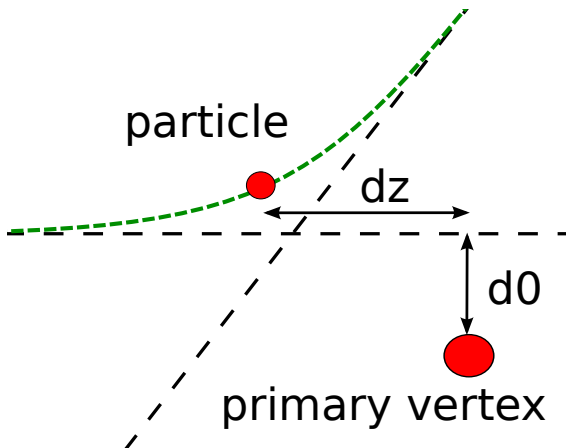
Figure 5.2.: Sketch for parameters d_0 and d_z w.r.t to the primary vertex
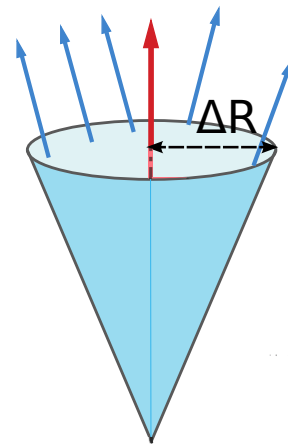
Figure 5.3.: Illustration of the Isolation calcultaion. The Isolation is calculated by adding all tracks within the isolation cone. Graphic adapted from [94].

Opposite sign Both muons are required to have opposite charges.

Kalman filter fit quality

The tracks for both muons are re-fitted using Kalman filter methods as implemented in CMSSW (see section 4.1 for a description of the Kalman algorithm) where a common vertex is set in the filtering algorithm initialization for the seed track. The curvature for the studied muons with p_T of several hundred GeV is extremely small and adding additional information about the vertex position can improve the invariant mass resolution in the high mass tails. The kinematic properties from the re-fit are then used to calculate the invariant mass of the two muon system for the final distribution. Finally a cut on the re-fit $\frac{\chi^2}{ndf}$ is applied to ensure a high quality of the fit.

Cosmic cut Highly energetic cosmic muons traversing the detector from top to bottom can be misidentified as a muon pair. In order to reduce this influence a cut on the 3D angle $\alpha < \pi - 0.2$ between the muon pair is applied. A sample of cosmic events selected by inverting the cosmic cut and dropping the requirements for a primary vertex on d_0 and d_z while keeping the rest of the selection as described above was produced in [92]. The distributions for the dimuon invariant mass and ϕ are shown in fig. 5.4.
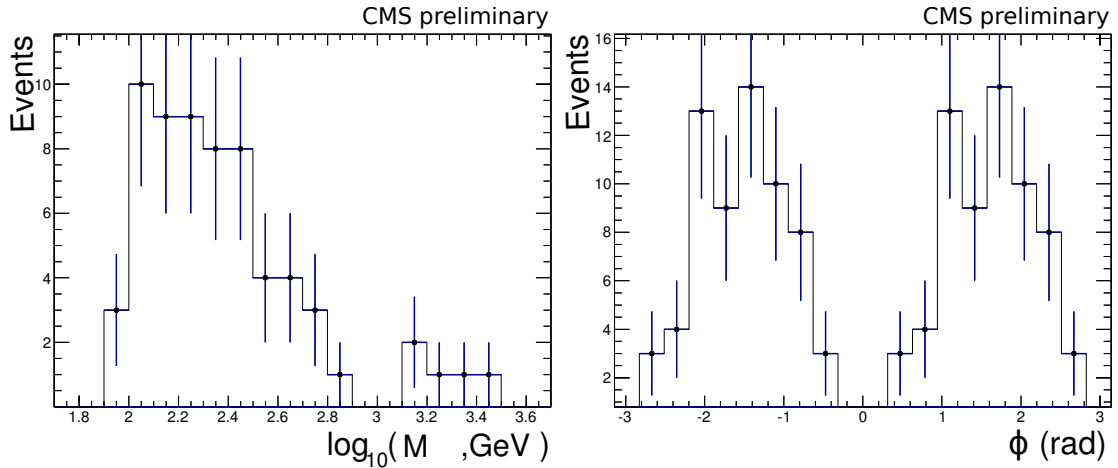
Figure 5.4.: Dimuon mass and ϕ distribution for a cosmic sample with full selection but inverted cosmic cut and without primary vertex cuts. Figure taken from [92].

	Cut	**Cut category**
single muon	$p_T > 45\text{GeV}$	Trigger & acceptance
	One muon matched to HLT trigger object within $\Delta R = \sqrt{\Delta\phi^2 + \Delta\eta^2} < 0.2$	
	One muon in $|\eta| < 2.1$, both muons $|\eta| < 2.4$	
	Common vertex with $|z| < 24\,\text{cm}$, $|r| < 2\,\text{cm}$	Primary vertex
	≥ 1 pixelhit, ≥ 6 track layers	Track quality
	Hits in ≥ 2 muon chambers	
	≥ 1 muon identified as tracker and global muon	Muon reconstruction
	relative error p_T measurement $\delta p_T / p_T < 0.3$	
	Isolation $\sum p_T / p_{T_\mu} \leq 0.1$ in R=0.3 cone	Isolation
	Impact parameter $d_0 \leq 0.2\,\text{cm}$ and $d_z \leq 5\,\text{mm}$	Cosmic veto
muon pair	Muon pair 3D-angle $\alpha < \pi - 0.02$	
	$\chi^2/ndf < 10$ Kalman filter refit with fixed vertex	Refit quality

Table 5.2.: Summary of applied cuts.

6. Background Processes

Several background sources are considered to contribute to the dimuon mass spectrum, where the SM model Drell-Yan process dominates and is the only relevant background source in the high mass region. The following description thus focuses on this process and other sources are only summarized briefly. A summary of all used MC samples and the corresponding cross sections can be found in table 6.2 while the expected number of events in different mass regions is summarized in table 10.1. The exact data set paths of the used MC samples may be of interest for readers who are members of the CMS collaboration, they are listed in appendix B.

6.1. Drell–Yan Process

As mentioned above the Drell-Yan process is the dominant background in the region of interest in the dimuon spectrum. The corresponding Feynman graph is shown in figure 6.1. The exact description of this process is crucial not only for a exact estimate of the background contributions in the signal region but also to gain confidence in the reconstruction method for high-p_T muons. Signal regions above $\sim 1 \text{TeV}$ struggle with limited statistics and frontier experimental conditions as no reference processes[1] exist to calibrate measurements at such energies. Previous studies indicate negligible ADD signal contributions up to masses of several hundred GeV [95, 96, 97]. A good agreement within the assigned uncertainties between SM expectation and the number of observed events for low dimuon masses is thus necessary to provide enough confidence in the analysis approach before it is possible to proceed with statistical inference from observations at the highest observed masses. In addition, higher order corrections are important with possible corrections of up to $\sim 30\%$ in the TeV region. The simulation of the Drell-Yan background in LO and NLO is discussed below together with NNLO corrections in QCD and NLO in EW-theory:

Drell-Yan at LO
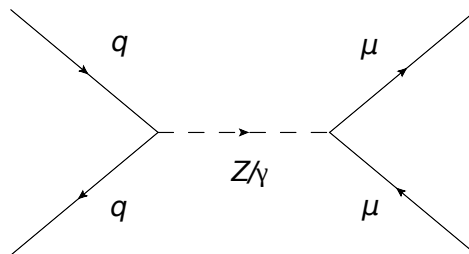
Figure 6.1.: Feynman graph for the leading order Drell-Yan process

---

[1]Apart from indirect methods e.g. cosmic studies as discussed in section 4.2.

6. Background Processes

The Drell-Yan process influences the ADD signal by interference in LO (born level) as described in section 2.2.1. It was simulated on generator level with `PYTHIA8` [34], without any additional detector simulation. The leading order contributions are implemented in various MC generators, `PYTHIA8` was chosen to ensure consistency in comparison with the LO DY contribution in the signal production, which also uses `PYTHIA8`. Contributions from initial (ISR) and final state (FSR) real photon emission are included in the simulation, again to ensure consistency with the signal simulation. The LO sample does not enter the final evaluation of the observed spectrum, but serves mainly as a baseline in the evaluation of higher order corrections and ADD contributions in the following sections. The LO contributions in different mass regions are listed in table 6.1 where the following requirements are made: one muon is within $|\eta| < 2.1$, the second muon is within $|\eta| < 2.4$ and both muons have $p_T > 45\,\text{GeV}$. This selection reflects the trigger acceptance cuts, see section 5.2.

DY (LO) $\to \mu\mu$, $\mathcal{L} = 20.6$ fb^{-1}					
Mass Region [TeV]	0.40–0.60	0.60–0.90	0.90–1.30	1.30–1.70	> 1.80
Expected events	1176±34	247.3±15.7	40.91±6.39	5.52±2.35	1.21±1.10

Table 6.1.: Number of expected events in 2012 for different mass regions for the LO Drell-Yan Process. Acceptance cuts reflecting the trigger η limitations ($|\eta| < 2.4$, $|\eta_1 < 2.1|$ or $|\eta_2 < 2.1|$ and $p_T > 45\,\text{GeV}$ threshold are applied. The errors describe only statistical uncertainties.

Drell-Yan at NLO and Higher Order Corrections
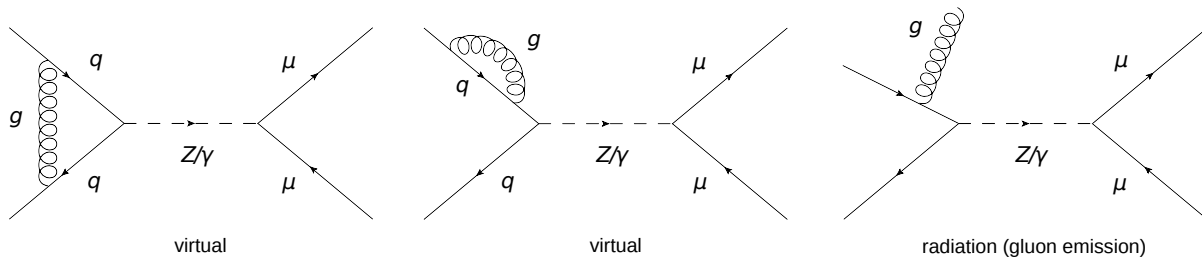
Figure 6.2.: Some example Feynman graphs for the QCD next-to-leading order Drell-Yan process. Two examples for vitual gluon exchange (left) and real gluon emission (right) are shown [3].

Calculations at NLO in QCD introduce new terms for virtual gluon exchange and real gluon emission; results from previous studies [3] indicate non-negligible contributions from these terms. Some examples for corresponding Feynman graphs are shown in figure 6.2. The Drell-Yan contributions at NLO in QCD are calculated with the `POWHEG` [98] event generator, which does not perform a parton showering and hadronsiation itself and is interfaced with `PYTHIA6` [99] for this task. For the main simulation the PDF set CT10 [100] is used, the uncertainty arising from this choice is discussed in section 8.3. The `POWHEG` sample is

simulated in different mass regions separately to ensure high statistics in the tail regions, the corresponding samples are listed in table 6.2. The obtained spectrum is corrected for NNLO QCD and NLO EW corrections and finally normalized to the number of observed events in the mass region $60\,\text{GeV} < M_{\mu\mu} < 120\,\text{GeV}$ observed in the full dataset. The motivation for this normalization is described below. The efficiency for the selection in section 5.2 was studied with the POWHEG sample and is found to be flat with a value close to 80% w.r.t to the total number of events and close to 90% w.r.t. to triggered events in the mass region from $1\,\text{TeV}$ up to $2.5\,\text{TeV}$, see figure 6.3.
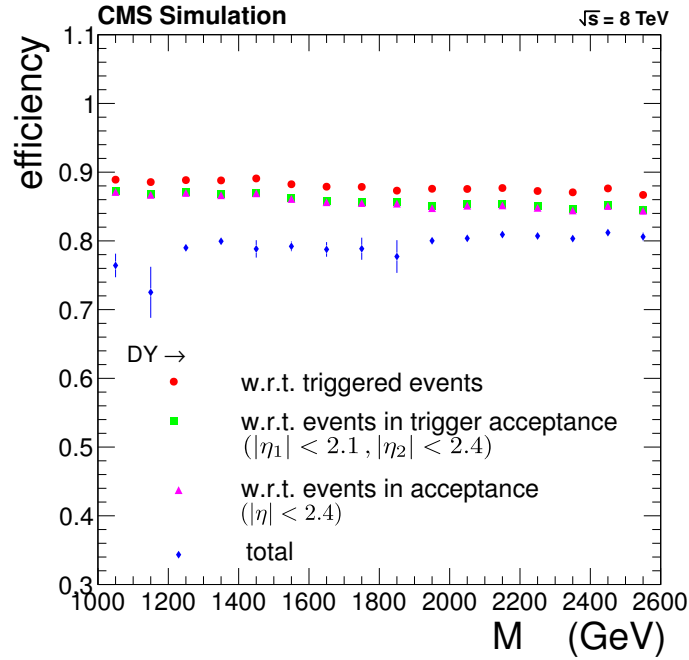
Figure 6.3.: Efficiencies of the POWHEG sample for the full selection w.r.t. to: the total Drell-Yan contributions, events in the acceptance $|\eta| < 2.4$, events in the trigger acceptance $|\eta_1| < 2.1$, $|\eta_2| < 2.4$ and triggered events.

NNLO QCD corrections
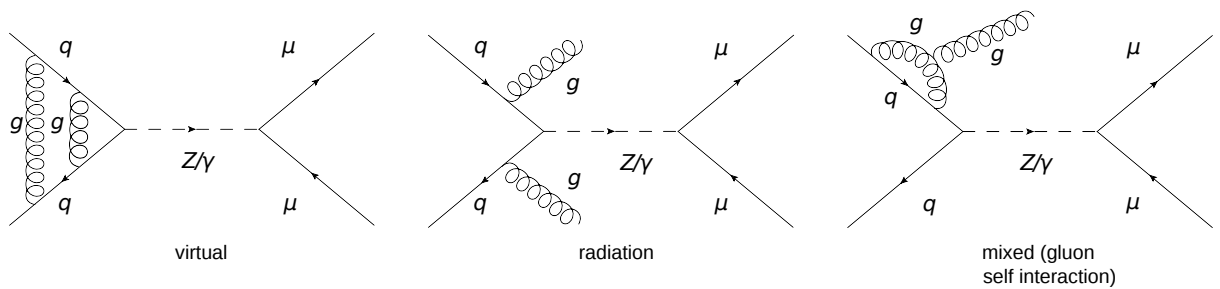
Figure 6.4.: Some example Feynman graphs for NNLO contributions [3].

6. Background Processes

Previous studies [3, 101] indicate corrections of less than 5% from NNLO QCD contributions. Feynman graphs with examples for virtual gluon exchange, gluon radiation and gluon self interaction terms are shown in figure 6.4. Gluon self interaction terms are not included until NNLO. The cross section generator `FEWZ` [102] is used to estimate NNLO corrections in QCD. A Monte Carlo cross section generator is only able to calculate cross sections at certain parameter points (here mass points) in contrast to an event generator like `PYTHIA6` or `POWHEG` which simulates the hard interaction and provides the full particle content and the related particle properties. No available event generator produces Drell-Yan events at NNLO and cross section generators like `FEWZ` give the best technical available predictions. Within the calculation acceptance cuts $|\eta_{\mu_1}| < 2.1$, $|\eta_{\mu_2}| < 2.4$ and $\mathrm{p_T} > 45\,\mathrm{GeV}$ are applied and the simulation uses the PDF set CT10 in accordance with the `POWHEG` QCD NLO simulation. The `POWHEG` cross section is scaled with the `FEWZ` NNLO to NLO ratio of 1.024 at the Z-peak. The scaling is only applied to the final event yield and does not account for other NNLO effects, e.g. changes in the acceptance. The evolution of the NNLO/NLO ratio (k-factor) was studied in [103] and is used to evaluated the uncertainty arising from the use of a flat scaling factor, this is discussed in section 8.2.1.

NLO EW corrections
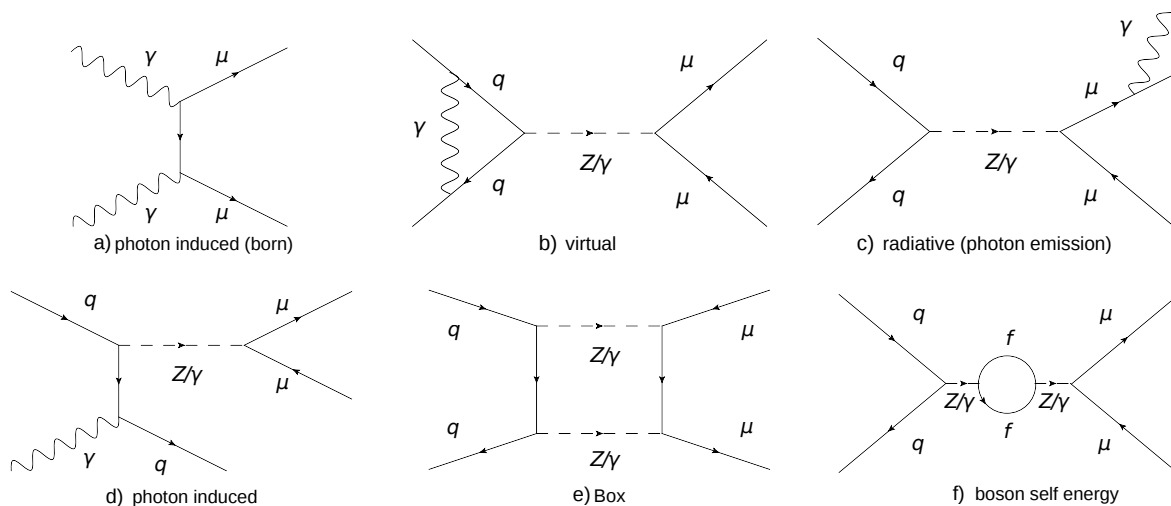
Figure 6.5.: Feynman graphs for additional contributions to the LO DY process of order α a) of order α^2 with additional photons (top row) and additional heavy bosons (lower row). Graphics adapted from [3].

EW graphs with two photons in the initial state (some order of α as LO process) and additional graphs of with one additional order in (α) are known to contribute about 10% percent to the Drell-Yan process at high masses [3]. The electro-weak corrections can be separated into three categories, where labels correspond to the example Feynman graphs in figure 6.5:

- Born level production of a lepton pair with two photons in the initial state, one example graph is shown with label a).

42

- Graphs with additional photons of order α^2. Example graphs are shown with label b) for virtual photon exchange, real photon emission (FSR) c) and graphs with a photon in the initial state d). Special interest lies on processes with at least one photon in the initial state a) and d) and the combined contributions from these graphs will be denoted as photon induced (PI) diagrams from here on. Previous studies [3, 104] found them to partially cancel other contributions.

- Graphs with additional heavy vector bosons. Box diagrams e) contain four particle interactions and introduce Sudakov factors of the form $\ln(\hat{s}/M_{W,Z}^2)$ to the amplitude. The corresponding corrections are found to be more than an order of magnitude greater than boson-self interaction contributions f). This is calculated in [105], where it is also shown that box diagrams with two W dominate the contributions.

Previous ADD studies [3] used the event generator `HORACE` [106] to calculate mass dependent cross section corrections at $\sqrt{s} = 7\,\mathrm{TeV}$, and this study was repeated at $8\,\mathrm{TeV}$. The new calculations were mostly performed by Sebastian Thüer and complemented by cross checks from the author of this thesis. Similar to `POWHEG` it is not possible to directly simulate QCD parton showers and the hadronisation in `HORACE`. They are not included in the presented results, but it has been found that the corresponding contributions are negligible when `HORACE` is interfaced with `HERWIG` [107] for the parton showering. The choice to use `HORACE` was mainly motivated by its capability to interface PDF sets which include photon contributions in order to simulate photon induced processes. The DGLAP equations [19, 18] are used to evolve measured PDF contributions to other energies (see section 1.2.2) and they only contain QCD interactions in the general version. The momentum distribution for photons in the hadron appears only in an extended version of the DGLAP equation which is rarely used and contains EW effects. The following approach aims to produce all EW corrections with the CT10 PDF set to ensure consistency with the `POWHEG` NLO sample, yet CT10 does not contain photon PDFs and MRST2004QED [108] is used to calculate photon induced contributions separately. For the combination of both results cross sections for three scenarios are simulated in seven mass bins with a width of $300\,\mathrm{GeV}$ from $200\,\mathrm{GeV}$ to $800\,\mathrm{GeV}$ and $400\,\mathrm{GeV}$ up to $2000\,\mathrm{GeV}$ with `HORACE`:

LO: Leading order production with photon final state radiation (FSR) simulated with the CT10 PDF set.

NLO$_{\mathbf{EW}}$: Simulation of the Drell-Yan process at NLO in EW with PDF set CT10. No photon induced graphs are included.

PI: Photon induced processes simulated with the MRST2004QED PDF set. The sample contains only events with at least one photon in the initial state.

The mass dependent cross section after acceptance cuts for the three scenarios are shown in figure 6.6 and used to calculate two separate correction factors w.r.t the `POWHEG` estimate **NLO$_{\mathbf{QCD}}$** for NLO in EW without PI and with PI separately:

k_1: This factor accounts for the the EW corrections without PI. The effects of FSR are already included in the `POWHEG` sample and the **LO** with FSR cross section estimate is subtracted to prevent double counting from FSR. The resulting estimate is normalized

to the `POWHEG` estimate in order to get a meaningful correction factor. The resulting correction factor is given by:

$$k_1 = 1 + \frac{\mathrm{NLO_{EW}} - \mathrm{LO}}{\mathrm{NLO_{QCD}}}$$

k_2: The photon induced correction factor is obtained by simply scaling the PI contributions to the `POWHEG` estimate:

$$k_2 = 1 + \frac{\mathrm{PI}}{\mathrm{NLO_{QCD}}}$$

Both obtained processes are assumed to be independent at high energies and their contributions are summed up to get an overall NLO EW correction factor k_3.

$$k_3 = 1 + \frac{\mathrm{NLO_{EW}} + \mathrm{PI} - \mathrm{LO}}{\mathrm{NLO_{QCD}}} = 1.01 - 0.042 \frac{M_{\mu\mu}}{\mathrm{TeV}}$$

A linear fit is used to interpolate between masses. The results for all contributions are shown in figure 6.6 together with the fitted function. The final Drell-Yan mass spectrum is corrected with the functional form obtained from the fit in the following plots and in the statistical evaluation of the results. As expected the results are similar to the previously obtained results in [3] and follow the general trend observed in comparisons with different generators [104] (A direct comparison is difficult as other results do not aim to correct cross sections with different PDF sets set but calculate all contributions with one PDF set.)

Normalization to the Z Resonance

A normalization to the Z resonance is used to substitute the luminosity measurement (see section 9.1) and cancel the differences between data and simulation for the experimental acceptance, trigger and offline efficiencies in first order. This leaves only a residual dependency for those quantities in p_T [92]. The impact of PDF uncertainties is also reduced by this approach [92, 103]. The normalization is calculated in [92] and the obtained normalization factor is used for this analysis. The normalization uses the same data set, MC samples and selection criteria as used in this analysis. Only the trigger requirement is changed to the pre-scaled trigger `HLT_Mu24_eta2p1` due to the low efficiency of the otherwise used trigger with a high $p_T > 40\,\mathrm{GeV}$ acceptance cut. Accordingly the offline p_T threshold is reduced to $27\,\mathrm{GeV}$. The prescale factor varied over time with a maximum of $pf_{max} = 300$ during data taking. Events are taken out at random $P(\mathrm{discard}) = 1 - pf/pf_{max}$ to adjust all samples to a common prescale factor. Events are counted in the mass region $60\,\mathrm{GeV} < M_{\mu\mu} < 120\,\mathrm{GeV}$ and non Drell-Yan backgound sources are estimated with Monte Carlo simulations and subtracted. The combined efficiency times acceptance for the prescaled trigger and the off-line selection is found to be 32.6% in simulations. The data-to-simulation efficiency scale factor accounting for both the online (triggering) and the off-line event selection is 0.987 ± 0.011 relative to the NNLO-corrected POWHEG sample, where the error is the combination of the statistical and systematic uncertainties.

The sources of systematic uncertainties are further discussed in section 8.2.3.
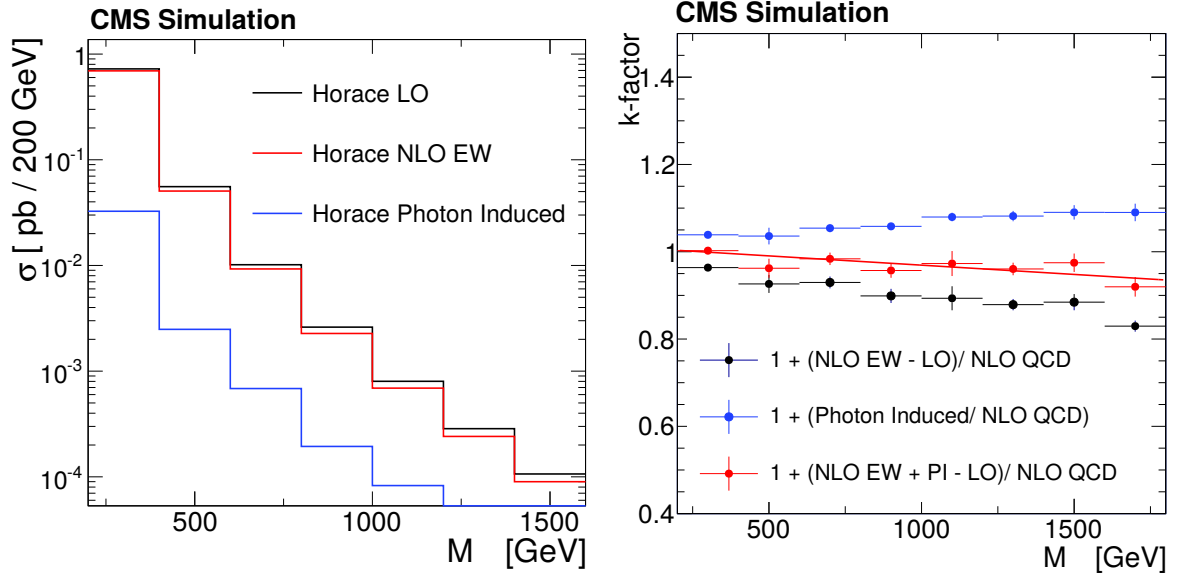
Figure 6.6.: (Left) cross sections of Drell-Yan→ $\mu\mu$: LO with final state photon emission (black), NLO in EW without photon induced graphs (red) and photon induced graphs (blue) only. (Right) resulting correction factors for NLO EW (black), photon induced (blue) and combined NLO EW and photon induced (red) w.r.t. to the POWHEG NLO QCD sample.

Evaluation of the Drell-Yan Simulation

This section aims to evaluate the corrections for the NLO QCD Drell-Yan simulation with POWHEG, which were introduced in the last sections and compares the final spectrum to the *LO* estimate with PYTHIA8. The two muon invariant mass distributions is shown in **??** for three cases:

1. POWHEG NLO QCD after the hard interaction including initial and final state radiation (ISR+FSR) for events with both muons within $|\eta| < 2.4$.

2. PYTHIA8 LO after the hard interaction (generated mass) for events with both muons within $|\eta| < 2.4$.

3. PYTHIA8 LO after the hard interaction (generated mass) including initial and final state radiation (ISR+FSR) for events with both muons within $|\eta| < 2.4$.
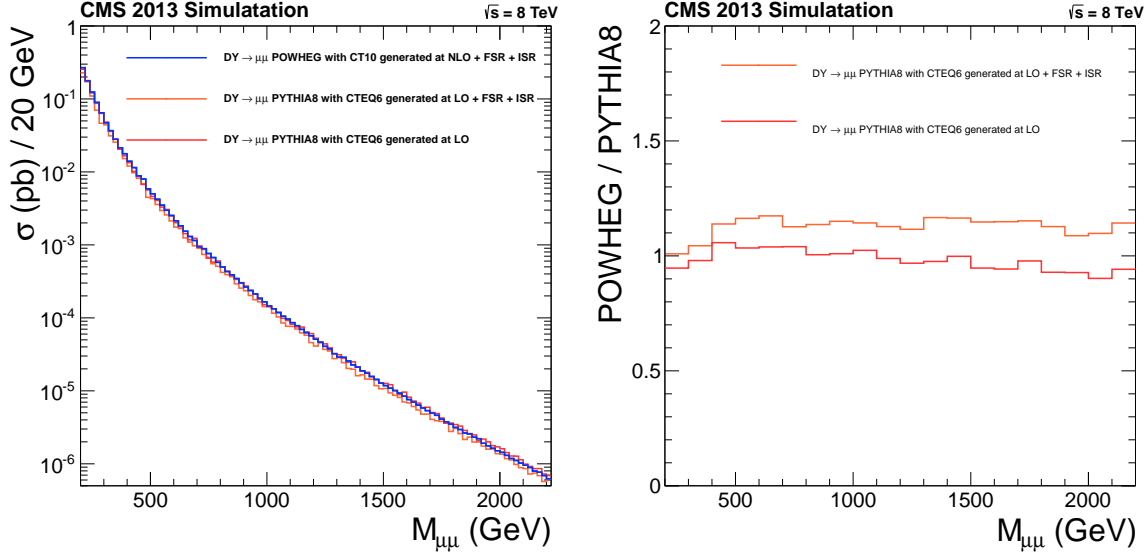
Figure 6.7.: Drell-Yan cross section dependent on the generated mass for: PYTHIA 8 at LO and POWHEG at NLO QCD before and after the full selection is applied. A detailed description of the used sample is given in the description above.

6.2. Non Drell-Yan Backgrounds

The combined contribution from non-DY background sources is found to be less than 10% in the studied mass region. Cosmic rays, secondary muons from multijet events and SM processes with final state muons in the hard interaction (prompt muons) are considered:

Non-Prompt Backgrounds:

Cosmic rays   As described in section 5.2 highly energetic muons which pass the detector near to the interaction point may fake a muon pair. The expected contributions in figure 5.4 are found to be well suppressed by the applied cuts on impact parameter d_0, d_z and the muon pair 3D-angle α in the studied mass region [92]. Events with small values for α were studied event-by-event to decide if an event is a cosmic candidate based on the muon timing and impact parameter. It is found that no cosmic event candidate remains above $\alpha = 2.5$ mrad [92]. There are 16 (9) cosmic event candidates with $M_{\mu\mu} > 120$ (200) GeV if the cuts on d_0, d_z and α are dropped. The contributions in the final selection are expected to be negligible as the cut on α is found to be 99% efficient at rejecting cosmic ray muons [109].

QCD Multijet Events   The cross sections for QCD multijet events are large and muons steming from jets may be identified as a dimuon event. A high statistics PYTHIA6 QCD sample with an increased fraction of events with high p_T muons was used to check the influence of this background and was found to be negligible. This result is confirmed by a data-driven approach to estimate contributions from events with two jets in [92], which estimates 0.1 events above 600 GeV with the same selection applied as in this analysis.

SM Background with Prompt Muons:

Diboson: The production of WW, WZ, ZZ pairs grows for center of mass energies above $m_{W,Z}$, where WW contributions dominate. All diboson samples were simulated with `PYTHIA6` using the CTEQ6L1 [110] PDF set, and cross sections corrected to NLO.

Top: Top pair production $t\bar{t}$ and single top production. Single top contribution comprises the associated production of tW, t and s channel tW and the charge conjugate $\bar{t}W$. The $t\bar{t}$ production clearly dominates the top processes and contributes as one of the main background sources for masses above $2m_t$. The event yield for $t\bar{t}$ events above $1\,\mathrm{TeV}$ was studied with an additional tail sample in [111] with a similar selection as in the presented approach. The result in [111] is used to estimate the number of events in the following plots and the interpretation of the expected spectrum. Only negligible contributions from $t\bar{t}$ events are expected for masses above $1.6\,\mathrm{TeV}$ from this sample. All top samples were produced with `POWHEG`, where the CT10 [100] PDF set is used for $t\bar{t}$ and CTEQ6L1 [110] for single top production. Cross sections are corrected to NNLO.

W+jets: The charged Drell-Yan process with an associated jet containing a high p_T muon may be interpreted as a dimuon pair. Contributions from this process were estimated with a high statistics MC sample produced with `MadGraph` and are expected to be negligible above $1\,\mathrm{TeV}$. The monte carlo estimate is again confirmed by the data-driven studies in [92] which estimate 1.0 ± 0.4 events above 600GeV.

Process	Generator	Selection	cross section σ (pb)	Events 10^6	PDF set
WW	`Pythia6`	−	54.8 (NLO)	9.96	CTEQ6L1
ZZ	`Pythia6`	−	17.3 (NLO)	9.80	CTEQ6L1
WZ	`Pythia6`	−	33.2 (NLO)	10.00	CTEQ6L1
$\bar{t}W$	`Powheg`	−	11.1 (NNLO)	0.493	CTEQ6L1
tW	`Powheg`	−	11.1 (NNLO)	0.498	CTEQ6L1
$t\bar{t}$	`Powheg`	−	234 (NNLO)	21.6	CT10
$W + Jets$	`MadGraph`	−	36257 (NNLO)	18.3	CTEQ6L1
$DY \rightarrow \tau\tau$	`Powheg`	$M_{\tau\tau} > 20$GeV	1915 (NLO)	1.51	CT10
$DY \rightarrow \mu\mu$	`Powheg`	$M_{\mu\mu} > 20$GeV	1915 (NLO)	24.5	CT10
$DY \rightarrow \mu\mu$	`Powheg`	$M_{\mu\mu} > 120$GeV	11.89 (NLO × 1.024)	1.00	CT10
$DY \rightarrow \mu\mu$	`Powheg`	$M_{\mu\mu} > 200$GeV	1.485 (NLO × 1.024)	1.00	CT10
$DY \rightarrow \mu\mu$	`Powheg`	$M_{\mu\mu} > 400$GeV	0.1086 (NLO × 1.024)	1.00	CT10
$DY \rightarrow \mu\mu$	`Powheg`	$M_{\mu\mu} > 500$GeV	$4.415 \cdot 10^{-2}$ (NLO × 1.024)	1.00	CT10
$DY \rightarrow \mu\mu$	`Powheg`	$M_{\mu\mu} > 700$GeV	$1.102 \cdot 10^{-2}$ (NLO × 1.024)	1.00	CT10
$DY \rightarrow \mu\mu$	`Powheg`	$M_{\mu\mu} > 800$GeV	$5.491 \cdot 10^{-3}$ (NLO × 1.024)	1.00	CT10
$DY \rightarrow \mu\mu$	`Powheg`	$M_{\mu\mu} > 1000$GeV	$1.180 \cdot 10^{-3}$ (NLO × 1.024)	1.00	CT10
$DY \rightarrow \mu\mu$	`Powheg`	$M_{\mu\mu} > 1500$GeV	$1.171 \cdot 10^{-4}$ (NLO × 1.024)	1.00	CT10
$DY \rightarrow \mu\mu$	`Powheg`	$M_{\mu\mu} > 2000$GeV	$2.218 \cdot 10^{-5}$ (NLO × 1.024)	1.00	CT10

Table 6.2.: Summary of simulated background samples.

7. Monte Carlo Signal Production

The dilepton production via virtual graviton exchange in the ADD model is implemented in leading order in `PYTHIA8` [34, 35]. Within the generator the GRW parameter convention is used to generate ADD events depending on the model parameter Λ_T together with the LO Drell-Yan estimate and the corresponding interference terms, see section 2.2.1. Mass dependent cross sections are simulated for Λ_T between 1.5TeV and 4.9TeV in 0.1TeV steps. `PYTHIA` contains a vast set of partly correlated parameters to ensure a good agreement in the simulated parton showering. Special option sets (tunes) are derived from fits to experimental data, more information on tunes can be found in the Pythia8 online manual [112]. The tune 4C [113] was used to simulate the ADD signal sample, it is based on early CMS data for hadronization parameters. A comparison between `PYTHIA8` with tune 4C and other simulators can be found in [114].

A comparison of the LO Drell-Yan expectation and the ADD signal for several choices of Λ_T is shown in figure 7.1. Only seven representative parameter points were simulated with the full detector simulation and served as benchmark point for the expected signal efficiency. They are listed in table 7.1 with their LO cross sections. Efficiencies for the applied selection are shown in figure 7.1 for an ADD sample with $\Lambda_T = 3.6$TeV with respect to:

- The total number of events.

- Events with both muons within the detector acceptance $|\eta| < 2.4$.

- Events with at least on muon that fulfils the trigger acceptance requirements $|\eta| < 2.1$

- Triggered events.

The efficiency is found to be flat with a value close to 80% w.r.t to the total signal and close to 90% w.r.t. to triggered events in the mass region from 1TeV up to 2.5TeV. Higher values show no further structure, but are limited by the statistics in the MC samples. The Drell-Yan efficiencies in figure 6.3 show similar values as it is expected from the related process signatures. A relative uncertainty of 3% is assigned to the efficiency w.r.t to the total signal cross section in the following calculations.

ADD signal ($G+Z/\gamma$+interference) $\to \mu\mu$, $M_{\mu\mu} > 1050$GeV							
Λ_T (TeV)	1.6	2.4	3.6	4.0	4.4	4.8	5.2
σ (pb)	1.45	0.0587	$5.92 \cdot 10^{-3}$	$4.63 \cdot 10^{-3}$	$4.18 \cdot 10^{-3}$	$3.92 \cdot 10^{-3}$	$3.80 \cdot 10^{-3}$

Table 7.1.: Benchmark ADD samples simulated with the full detector simulation.
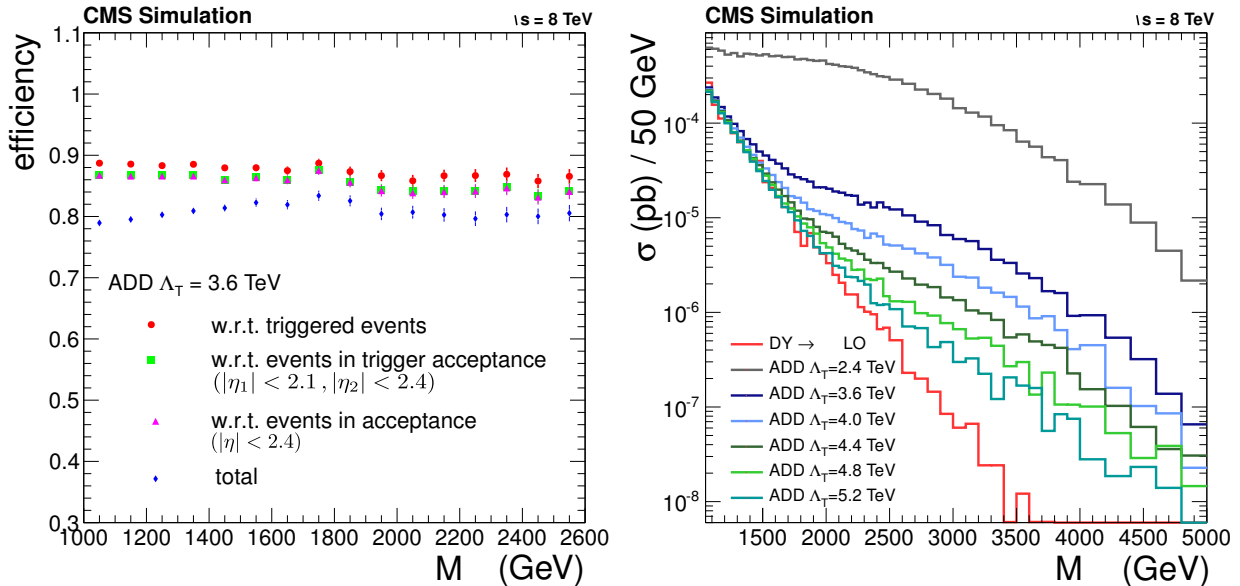
Figure 7.1.: (Left) Efficiencies for the full selection w.r.t. to : events from the complete signal (total), events in the acceptance $|\eta| < 2.4$, events in the trigger acceptance $|\eta_1| < 2.1$, $|\eta_2| < 2.4$ and triggered events for $\Lambda_T = 3.6$TeV. (Right) Mass dependent cross sections for ADD signals for different values of Λ_T, in comparision with the LO Drell Yan process.

7.1. NLO QCD Corrections

The NLO QCD corrections to the ADD dilepton production are known to similarly comparable to the SM Drell-Yan process. The exact calculations can be found in [115]. The authors of this publication kindly agreed to perform specific calculations for the 7 TeV ADD search [3], where acceptance and PDF settings were set to agree with approach in [3] and this analysis, see figure 7.2. This simulation relies on the newly developed MC Generator `aMC@NLO` which is based on `MadGraph5` [116] and incorporates various additional libraries to extend it. A publication with a general description of the framework will soon be available [117]. The observed turn-on effect is related to the position of the lightest KK-modes dependent on M_s. The 7 TeV analysis concluded to use a flat NLO/LO k-factor 1.3. This choice is rather conservative as the simulated corrections reach from 1.3 to 1.8 in the studied mass region in figure 7.2. Yet it should be emphasized that the ADD model does not intend to be a detailed model of new physics but rather a reference model for a set of extra dimensional models with flat brane physics. The conservative k-factor should reflect that the NLO contributions may be smaller for more detailed models. Recent results calculated with `aMC@NLO` at $\sqrt{s} = 8$ TeV show no significant changes within the model uncertainties compared to the 7TeV estimate [118]. The final results in section 9 are interpreted both with the ADD LO cross section and with a flat k-factor of 1.3 for NLO QCD contributions.
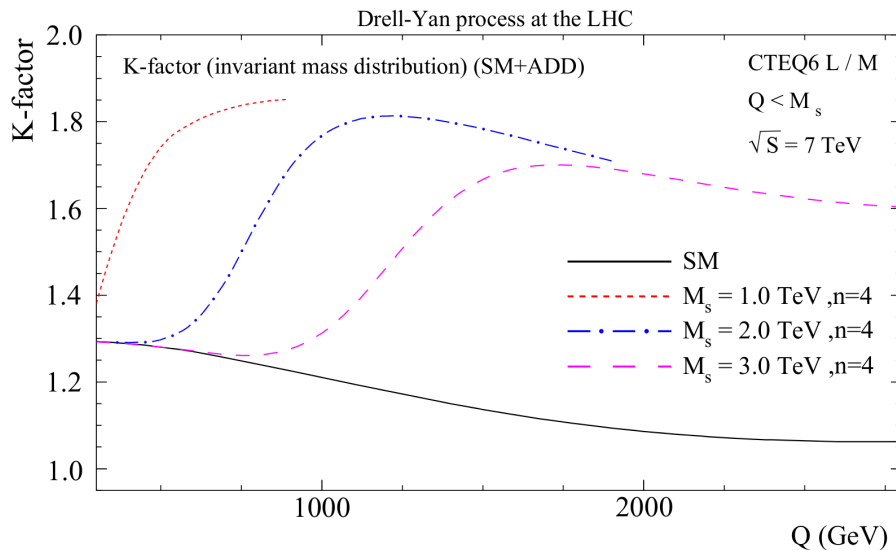
Figure 7.2.: Mass dependent k-factor for ADD models at $\sqrt{s} = 7$TeV [3].

7.2. Angular Distribution

Higher masses for the graviton resonances and the differences in the theoretical angular distribution as described in section 2.2.1 were studied for MC samples including the full detector simulation and single muon selection criteria [1] as described in the last section. The pseudo-rapidity distribution for a representative ADD sample with $\Lambda_T = 3.6$TeV and the SM DY expectation is shown in figure 7.3 for dimuon masses $M_{\mu\mu} > 1000\,\text{GeV}$ and $M_{\mu\mu} > 1050\,\text{GeV}$ respectively. It is already visibly that a potential ADD signal would tend towards central values in the η_1-η_2 plane but the separation between signal and background is rather small for this projection of the angular distribution. The angular distribution for θ^* defined as the scattering angle of the positively charged muon in the dimuon cms frame, as introduced in section 1.2.2 dependent on the dimuon invariant mass is shown in figure 7.3. A possible separation using θ^* was studied in in previous searches for extra dimensions, e.g. [50]. It can be seen that the ADD sample tends more towards small values for $\cos(\theta^*)$. The number of events in the region with the highest signal to background ratio is much smaller than 1 if the expected signal cross section is scaled with the recorded integrated luminosity. The angular distribution was studied in a late stage of this work and cross section estimates were only stored with information about the angular distribution for the benchmark points, it was unfortunately not possible to re-simulate the signal estimate with a sufficiently small separation in Λ_T to quantify the potential to improve the results with this approach within the given time scope. Yet only small improvements are expected as the background expectation is already close to zero for dimuon masses with a clear signal to background separation.

---

[1]No dimuon cuts, e.g. cosmic angle cuts are applied.
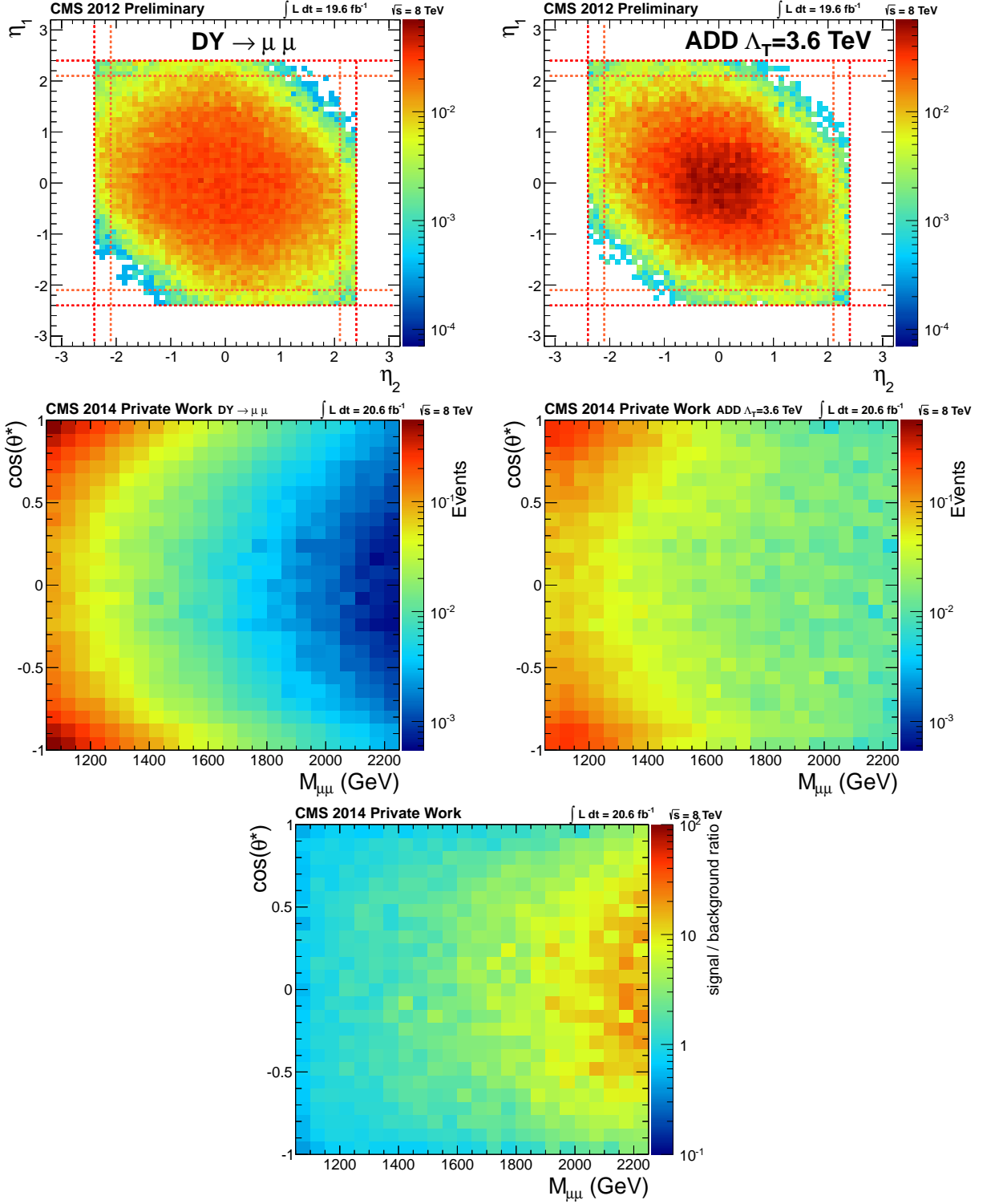
Figure 7.3.: (Upper row) Pseudo-rapidity distribution η for selected muon pairs for the SM Drell-Yan process (left with $M_{\mu\mu} > 1000\,\text{GeV}$) and ADD sample with $\Lambda_T = 3.6\text{TeV}$ (right with $M_{\mu\mu} > 1050\,\text{GeV}$). Acceptances for the muon system and the muon trigger are indicated by red and yellow lines, respectivlely.

(Middle row) Number of expected events dependent on the dimuon invariant mass $M_{\mu\mu}$ and $\cos(\theta^*)$ for the SM Drell-Yan process (left) and ADD sample with $\Lambda_T = 3.6\text{TeV}$ (right) scaled to an integrated luminosity of $20.6\,\text{fb}^{-1}$. The full selsection as described in section 5.2 is applied.

(Lower row) Signal (ADD) to background (Drell-Yan) ratio.

8. Systematic Uncertainties

Various sources of systematic uncertainties were studied and the results are described in this chapter. The contributions can be separated into three categories:

- **Global:** Global uncertainties describe effects which are not directly related to the studied process and influence the whole event. For this search experimental uncertainties in the luminosity measurement and possible effects from high detector occupancies (pileup) are considered.

- **Background Simulation:** The simulation of the background uses one of several possible PDF sets and the uncertainty of this choice is studied with various sets. Additional uncertainties arise from the corrections applied to the Drell-Yan background, namely: Z-peak normalization, NNLO QCD and NLO EW corrections.

- **Muon Reconstruction:** Experimental uncertainties in the muon reconstruction arise from limited knowledge about the resolution and absolute scale in p_T measurements for high energetic muons. Uncertainties in the simulation of the muon system alignment further influence the track measurement.

8.1. Global Uncertainties

8.1.1. Luminosity

The pixel detector of the inner tracker is used to measure the luminosity during data taking. The per bunch crossing instantaneous luminosity L is proportional to the number of collisions per crossing κ [119]:

$$\nu \, \kappa = L \, \sigma_T$$

with the revolution frequency of $\nu = 11246 \mathrm{Hz}$ and total inelastic cross section σ_T [119]. κ and σ_T can not be estimated directly, but can be related to the accessible parameters: $\langle n \rangle = \kappa \, n_1$ for the average number of pixel clusters per event and the visible cross section $\sigma_{vis} = \sigma_T \, n_1$. Both parameters are related via the the average number of clusters per inelastic collisions n_1. Using σ_{vis} and $\langle n \rangle$ the luminosity L can be expressed as [119]:

$$L = \frac{\nu \, \langle n \rangle}{\sigma_{vis}}$$

In this equation $\langle n \rangle$ is measured during data taking and σ_{vis} is estimated in special LHC runs with large bunch separation using van der Meer scans [120]. During the 2012 Run it was possible to measure the luminosity with an uncertainty of $2.5\%(\mathrm{sys}) \pm 0.5\%(\mathrm{stat.})$ using this method [119]. Both errors are added in quadrature to obtain the total luminosity uncertainty of 2.6% for the limit calculation. This uncertainty mainly influences the signal prediction as the luminosity dependence for the dominant Drell-Yan background is cancelled by the Z-peak normalization.

8.1.2. Pileup

Pileup describes the effects from secondary interactions (in-time- pileup) and interactions from previous or following bunch crossings (out-of-time pileup). Many analyses try to account for this influence by producing Monte Carlo events with a predefined distribution for the number of underlying events[1] and minimum bias events[2] added to the hard interaction. The initially produced distribution is then re-weighted to match the number of well reconstructed vertices observed in detector measurements [123]. Previous iterations of this analysis at 7 TeV proved to be robust against pile-up, which means that the reconstruction quality for the highly energetic muons seems independent of higher detector occupancy [3]. Yet the steeply increasing luminosity during data taking in 2012 made a cross-check necessary to show that this assumption is still valid. The following data-driven approach was used as described bellow:

- The data sample is divided into a "low" and "high" pileup sub-sample dependent on the the number of primary vertices within the event. The cut intends to select approximately $\frac{2}{3}$ of the sample as low pileup events [3] , as shown on the left side of figure 8.1.

- The ratio of invariant mass distributions high / low is calculated.

No mass dependency for the ratio is observed, as it can be seen from the left plot in figure 8.1. This cross check confirms the choice to omit pile up corrections and the corresponding systematic uncertainties.
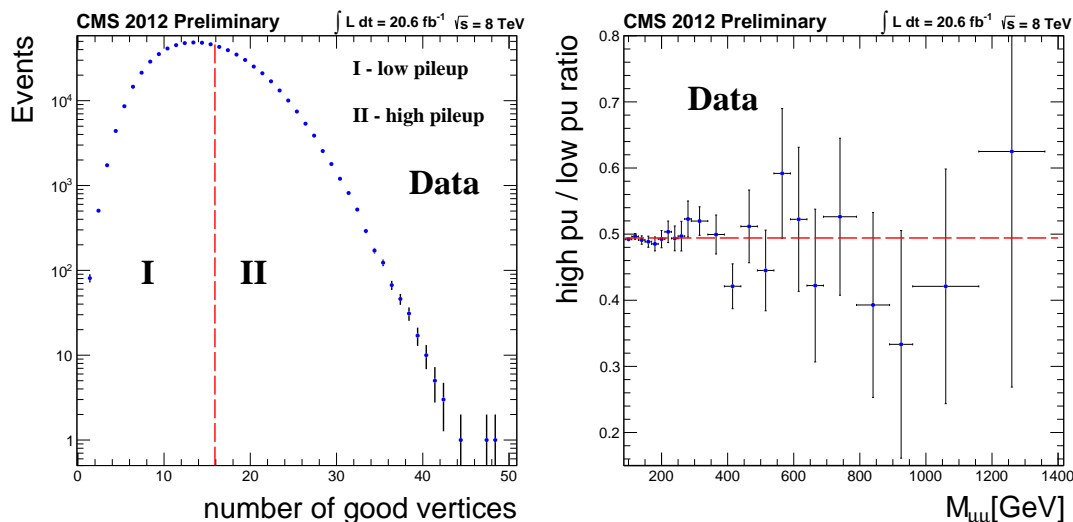
Figure 8.1.: (Left) Number of well reconstructed primary vertices (see section 5.2) divided in a low and high pileup sub-sample. (Right) Ratio of invariant mass distributions for the low and high pileup sub-samples.

---

[1]Underlying events contain beam-beam remnants from semi-soft or soft multi parton interactions [121]. Particles produced in semi-soft interactions contain hard interactions with only a small $p_T \lesssim 2$ GeV [122].

[2]Minimum bias is a generic term for events recorded with a loose trigger in order to record the largest possible fraction of the overall inelastic cross section [121].

[3]The number of vertices is an integer number, the closest cut to the desired separation of events is sixteen, leading to ratios of 0.699, 0.301 for low and high selection, respectively.

8.2. Drell-Yan Corrections

The following descriptions evaluate the uncertainties arising from the corrections to the Drell-Yan NLO QCD process introduced in section 6.1.

8.2.1. QCD NNLO Corrections

The used flat NNLO/NLO QCD k-factor takes only corrections at the Z-peak into account. The k-factor is found to be flat in simulations with FEWZ[103]. Three mass points at $1\,\mathrm{TeV}$, $1.5\,\mathrm{TeV}$ and $2\,\mathrm{TeV}$ were produced and the variations in the k-factor was found to be smaller than 3%. This value is used as a constant uncertainty on the Drell-Yan background expectation.

8.2.2. NLO EW Corrections

The estimated NLO EW k-factor in section 6.1 is influenced by the choice of the PDF set and various systematic uncertainties within the simulation of the hard interaction. The recently released version 3 of FEWZ added NLO EW calculations including photon induced diagrams. Dimitri Burilkov kindly agreed to perform cross checks on the k-factor using version 2 and 3 of FEWZ. EW corrections are only implemented in version 3 and the ratio of both versions may serve as an estimate for the expected EW contributions, the result is shown in figure 8.2. It should be noted that all processes are calculated with the pdf set MRST2004QED in FEWZ, while the estimation in 6.1 aims to correct the spectrum w.r.t. the POWHEG estimate using CT10 PDFs. An uncertainty of 5% is assigned to the used k-factor to account for the observed differences w.r.t. the cross check results and previous studies [104, 124].

8.2.3. Z-peak Normalization

Two dominating sources of systematic uncertainty contribute to the data to simulation ratio used to normalize to the Z resonance.

- The fraction of Z events in the acceptance is small compared to heavier and thus more central signals. Recent studies estimate a systematic uncertainty of about 1.9% on the Z-boson acceptance [125].

- The evolutions of the triggering and reconstruction efficiency from the Z-peak to masses of $2\,\mathrm{TeV}$ are estimated by 2.5% in simulations with high mass Z' events, with an acceptance comparable to our signal. This factor reflects the residual changes from the Z-peak to high masses.

Both uncertainties are combined into an overall normalization related uncertainty of 3%.
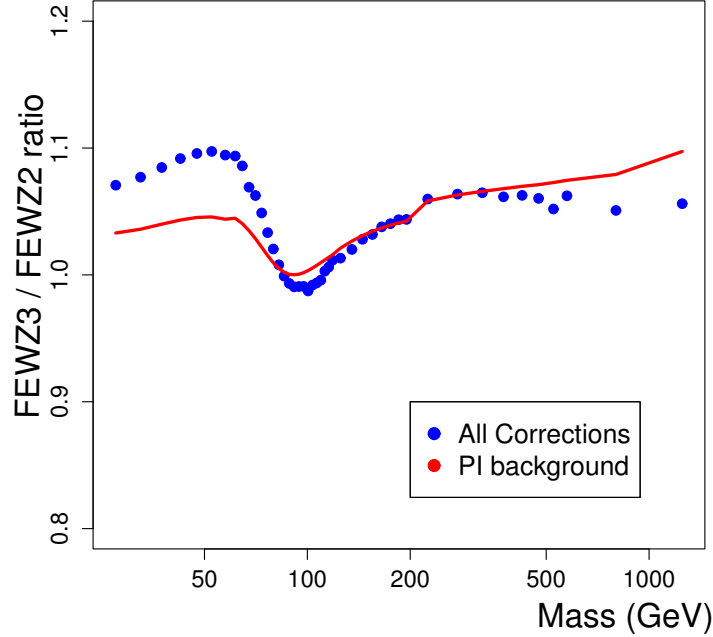
Figure 8.2.: `FEWZ` version 3 to 2 ratio for the Drell-Yan process. Version 3 includes the full NLO contributions with photon induced processes (red), while version 2 contains only QCD NLO contributions. Calcultations kindly provided by Dimitri Bourilkov.

8.3. Parton Distribution Functions

Uncertainties in the $M_{\mu\mu}$ distribution arising from parton distribution functions were studied by the Z′ group in a dedicated analysis[4] at NNLO [103]. Both approaches followed the PDF4LHC [126] recommendations. The NNLO pdf sets MSTW08, CTEQ12 and NNPDF were used as implemented in `LHAPDF` [127] to calculate cross sections with the Fully Exclusive W and Z package `FEWZ` [128] for the neutral DY process. All cross sections are calculated at 68% confidence level in several mass bins with a width of 100 GeV. The calculated event yield is normalized to the region (60-120)GeV. The cross section calculation applied kinematic cuts of $p_T > 45$GeV and $|\eta| < 2.4$. The resulting central values and confidence limits are then translated into relative residuals from the central value for each PDF set. A two sided envelope for the residuals in all sets is finally determined, and the envelopes are symmetrized: the width divided by two is used as the uncertainty for a given mass point. The results are summarized in table 8.1. A fit is applied to get a continuous estimate for the pdf uncertainty at each mass point:

$$\frac{\delta N}{N}(M) = \left(2.76 + 3.03 \cdot 10^{-3} \cdot \frac{M}{\text{GeV}} + 2.38 \cdot 10^{6} \cdot \frac{M^2}{\text{GeV}^2} \right) \% \qquad (8.1)$$

The fitted functions are shown in figure 8.3 together with the result from table 8.1.

---

[4]This study replaced the previously used internal estimates, which were produced using NLO PDF sets
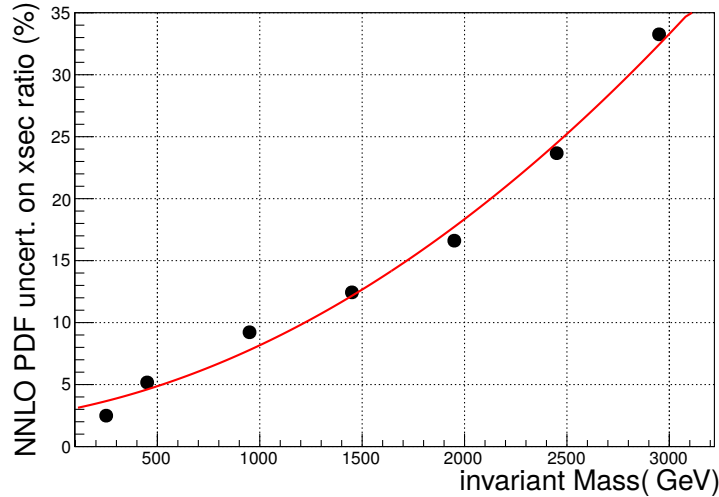
Figure 8.3.: NNLO PDF uncertainties studied with `FEWZ` as a function of the dimuon invariant mass [103].

mass range (GeV)	ratio $\pm$ PDF uncert.	relative uncertainty (%)
200-300	$6.42 \cdot 10^{-4} \pm 1.60 \cdot 10^{-5}$	2.5
400-500	$4.50 \cdot 10^{-5} \pm 2.33 \cdot 10^{-6}$	5.2
900-1000	$1.04 \cdot 10^{-6} \pm 9.58 \cdot 10^{-8}$	9.2
1400-1500	$2.46 \cdot 10^{-8} \pm 3.06 \cdot 10^{-9}$	12.4
1900-2000	$1.37 \cdot 10^{-9} \pm 2.28 \cdot 10^{-10}$	16.6
2400-2500	$1.04 \cdot 10^{-10} \pm 2.47 \cdot 10^{-11}$	23.7
2900-3000	$8.50 \cdot 10^{-12} \pm 2.80 \cdot 10^{-12}$	33.3

Table 8.1.: Results for the cross section calculation normalized to a mass bin from $(60 - 120)$GeV and the corresponding PDF uncertainty for different mass bins. The results were obtained with the PDF4LHC recipe with the NNLO PDF sets: MSTW08,CTEQ12 and NNPDF [103].

8.4. Muon Reconstruction

8.4.1. Muon System Alignment

The reconstruction of high-p_T muons is extremely sensitive to the position of hits and thus relies on the exact knowledge of the muon system geometry during the complete measurement. The effects of uncertainty in the muon system position on the final distribution are referred to as muon alignment uncertainties. During the evaluation of Monte Carlo samples in 2012 an unexpected performance ranking for tracker and TuneP reconstruction algorithms was observed, where the dimuon mass resolution of the tracker-only fit was found to be better than the TuneP fit for high-p_T muons [92]. This unexpected behaviour was traced back to an unintended shift in the ϕ-plane of ≈ 2mm for the muon system in Monte Carlo simulations. The old alignment scenario (`V7A`) was replaced by a new baseline alignment (`V7C1`)

which uses realistic alignment conditions. In addition a sample representing an ideal align-
ment (V7C2) was developed as a benchmark scenario. The influence on the dimuon mass
reconstruction was studied for both background and signal samples, see figure 8.4 and 8.5. A
comparison of the relative dimuon mass resolution is shown in 8.6 for the V7C1 scenario (left)
and V7C2 (right), the effects of muon system alignment is clearly visible and it is concluded
to add a 5% uncertainty on the signal and Drell-Yan background expectation to account for
this effect, which is a rather conservative choice.
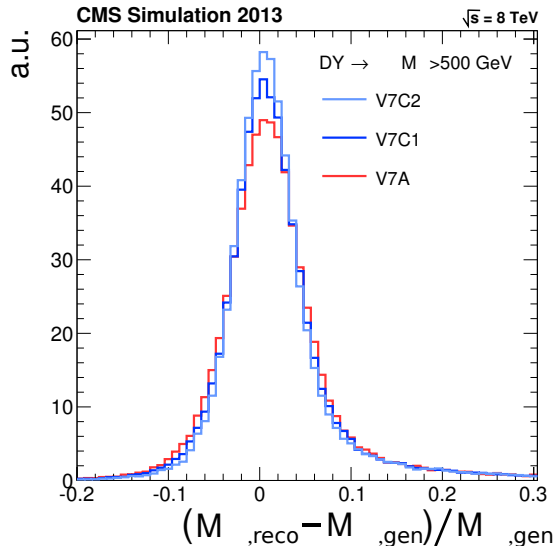
Figure 8.4.: Dimuon mass resolution for
different muon system align-
ment scenarios in Drell-Yan
events with a dimuon mass
above 500 GeV.
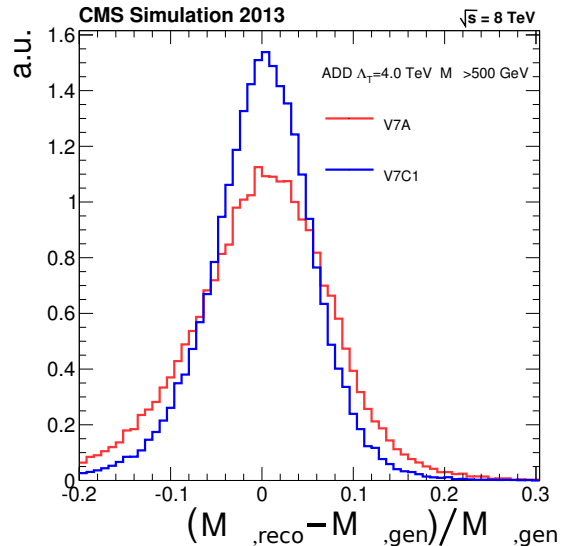
Figure 8.5.: Dimuon mass resolution for
different muon system align-
ment scenarios in ADD signal
($\Lambda_T = 4\,\text{TeV}$) events with a
dimuon mass above 500 GeV.

8.4.2. Muon Momentum Scale

A further source of a systematic uncertainty is the limited knowlege of the absolute scale in
the muon momentum measurement. This muon momentum scale uncertainty was studied by
the muon POG with cosmic events. A cosmic muon traversing the detector near the interac-
tion point is identified as a pair of oppositely charged muons in the standard reconstruction
algorithms. The flip of the charge q happens because the direction of motion is inverted for
the upper muon leg compared to collision data. The reconstructed muon pair is expected to
have an equal momentum as they represent the same particle. A possible shift in the q/p_T
distribution for cosmic events can thus be used to quantify a systematic shift κ in the muon
momentum reconstruction:

$$\frac{q}{p_\text{T}} \to \frac{q}{p_\text{T}} + \kappa.$$

In the ideal case of absence of a scale bias, the distributions for $q/p_\text{T} < 0$ and $q/p_\text{T} > 0$
are expected to be similar with respect to a charge flip for the upper muon (one of the
distributions is mirrored at the y-axis). Both distributions are shown in figure 8.7 for events
from a 2011 cosmic dataset with $p_\text{T} > 100\,\text{GeV}$, where no additional bias is introduced
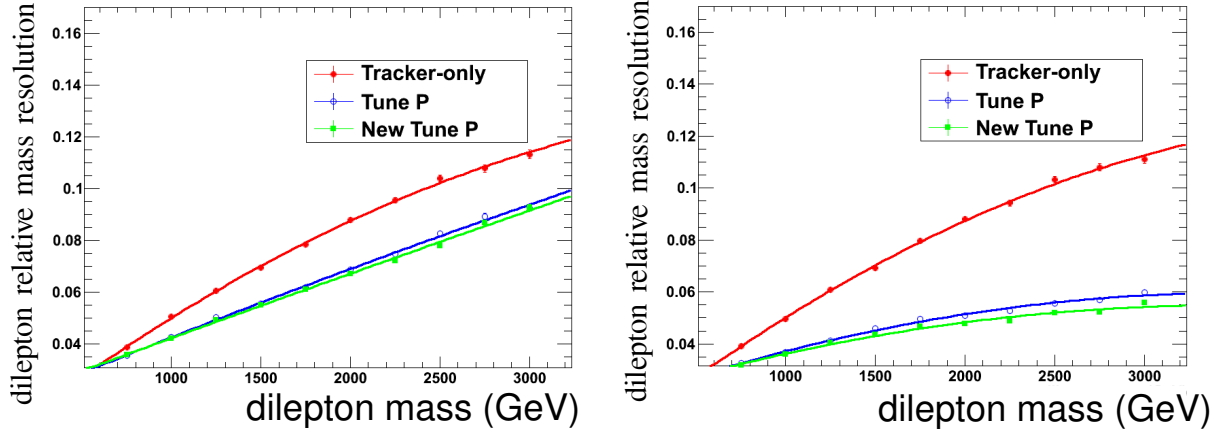
Figure 8.6.: Relative dimuon mass distribution for the V7C1 and V7C2 alignment scenario. Graphic taken from [92].

in the left plot and an artificially enlarged bias $\kappa_{art} = 1 \, \text{TeV}^{-1}$ is introduced on the right plot to help illustrate how the distributions reacts to a constant scale shift. The χ^2 for the
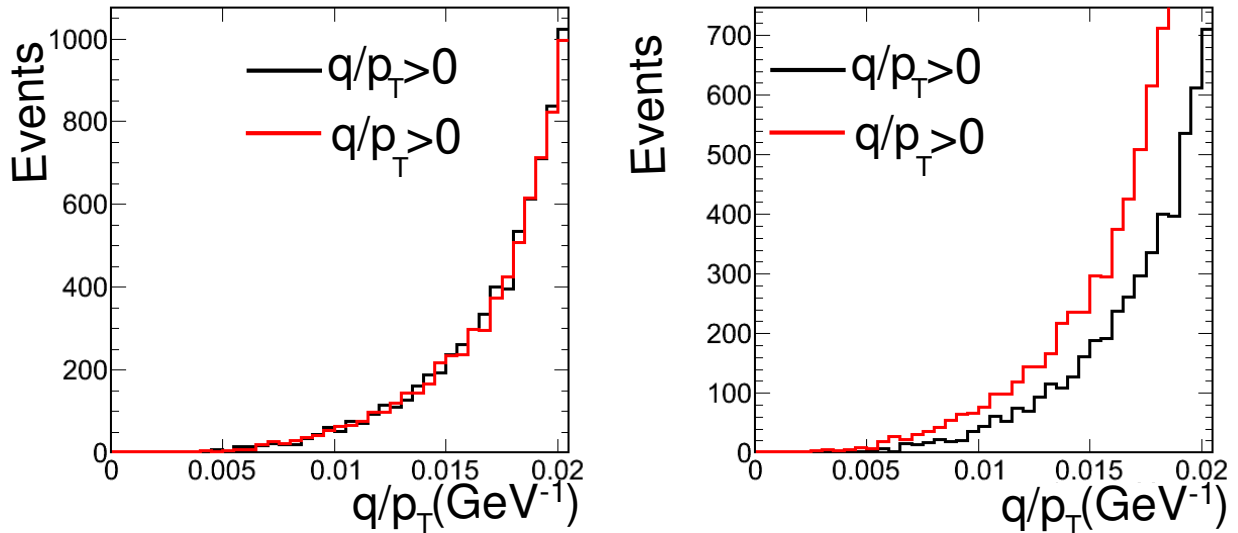
Figure 8.7.: $q/p_t < 0$ distribution in a 2011 cosmic dataset where a cut $p_T > 100 \, \text{GeV}$ is applied left(left). (Right) same data with an atificially injected scale bias $\kappa = 1 \, \text{TeV}^{-1}$. Graphic taken from [129].

distributions in figure 8.7 is then calculated depending on a additional injected shift κ_{inj}. An example χ^2 distribution is shown on the left side of figure 8.8 together with a polynomial fit of order 8. The minimum of the χ^2 distribution represents the linear scale shift, which brings both distributions to the best agreement (as argued before). The observed minimum for the example with an artificial shift is found to be $\kappa_{inj} = -0.95 \, \text{TeV}^{-1} = -\kappa$ (see left side of figure 8.8) and correctly quantifies the artificially introduced bias with a relative error of about 5%. The same method was applied to the cosmic sample without any additional bias and the observed values for κ, which minimizes the corresponding χ^2 distributions is

shown on the left side of figure 8.8 for different ϕ regions, together with the average value for both data taking periods. The observed bias in 2011 is $\kappa = (0.05 \pm 0.05)/\text{TeV}$ [130]. The
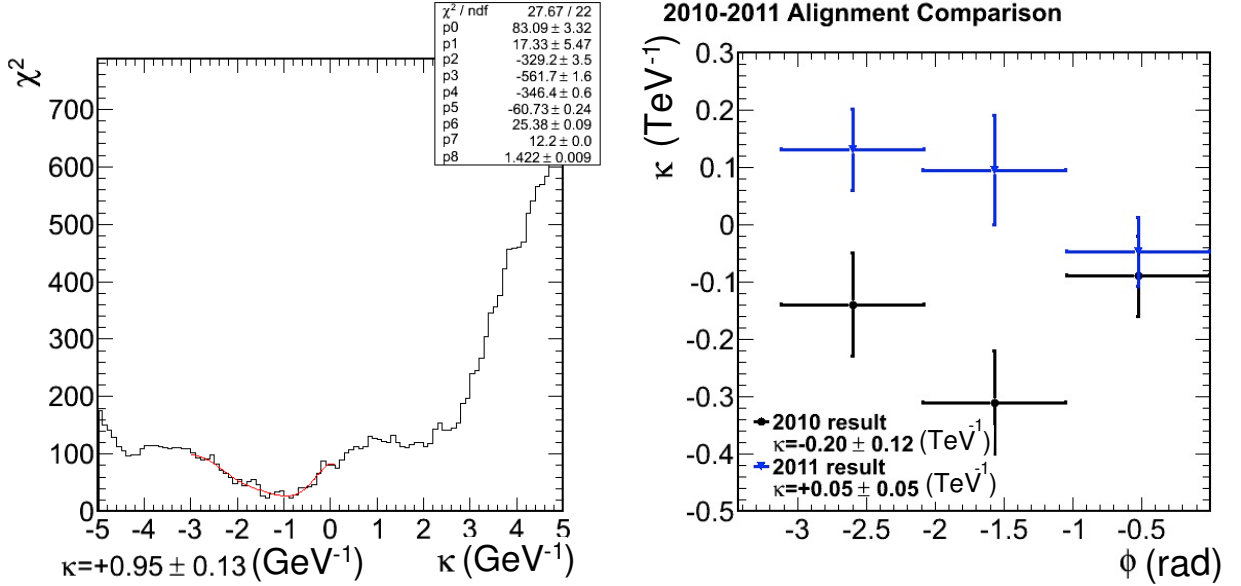
Figure 8.8.: (Left) χ^2 distribution corresponding to $q/\text{p}_\text{T} < 0$ and $q/\text{p}_\text{T} > 0$ from the right plot in figure 8.7, where an artifically injected scale bias $\kappa = 1\,\text{TeV}^{-1}$ is applied [129]. (Right) Observed bias κ for different regions in ϕ, the values dispayed in the lower left side of the plot corresponds to the value for κ averaged over ϕ [130].

reported error corresponds to the shift around the minimum κ which results in an increase by 1 in the χ^2 distribution (MINOS error) [129].

This value for κ is used[5] to rerun the analysis with a shifted value for the observed p_T :

$$\frac{1}{\text{p}_{\text{T,shifted}}} = (1 + \kappa)\,\frac{1}{\text{p}_\text{T}}.$$

The relative difference in the expected event yield for shifted and standard reconstruction in the dimuon mass distribution is used to estimate the scale uncertainty. A downward shift is also considered but it has significantly less effect for a steeply falling spectrum as it is expected for the SM dimuon mass distribution. A fit to the relative difference in the event yield dependent on the lower mass threshold M_{min} is used in the final estimate of the number of background events dependent on the lower dimuon mass threshold M_{min}:

$$\frac{\delta N}{N}(M_{\text{min}}) = 6.95 \cdot 10^{-2} \exp\left(-1.71 \cdot 10^{-4} \cdot \frac{M_{\text{min}}}{\text{GeV}}\right) + 9.98 \cdot 10^{-8} \cdot \frac{M_{\text{min}}^2}{\text{GeV}^2} \tag{8.2}$$

The influence on the expected number of signal events is much smaller due to the flat signal shape and is smaller than $\sim 12\%$ for events with $M_{\mu\mu} > 2\,\text{TeV}$. Muon momentum scale uncertainties turn out to be the dominant systematic uncertainty for both background and signal expectation in the limit calculation.

---

[5]This follows the muon POG recommendations for 2012 data.

8.4.3. Muon Momentum Resolution

The uncertainty arising from the limited knowledge of the p_T resolution distribution was studied with cosmic events similar to the endpoint method described above. When a cosmic muon traverses the detector near the interaction point its upper and lower legs are reconstructed as an opposite-sign dimuon pair. The resolution is estimated as a function of p_T using the width of the relative residuals R, where

$$R(q/p_T) = \frac{(q/p_T)^{upper} - (q/p_T)^{lower}}{\sqrt{2}(q/p_T)^{lower}},$$

see figure 4.1. The uncertainty in the dimuon mass distribution is then studied with Drell-Yan MC samples by smearing $1/p_T$ by a Gaussian distribution of width 0.03. This smearing factor is based on a similar approach used by previous studies e.g. searches for resonances in events with one muon and missing transverse energy [131]. The following procedure aims to validate this factor with the current simulations. The Drell-Yan background sample is binned in η and p_T to study the resolution in different acceptance regions. The resolution in each bin w.r.t. the generated mass is estimated and a gaussian distribution is fitted to the central part of the resolution distribution to obtain the width σ, see figure 8.9. The restriction to the central region is motivated by the non-gaussian tails of the distribution, which are associated to dramatic changes in the muon trajectory e.g. showering while the muon traverses the detector. In the next step the p_T dependency for σ is fitted in each η region using a linear function, two examples are shown in figure 8.10. A summary of results for different η regions is shown figure 8.11. Several conclusions can be drawn from the comparison of these Monte Carlo based results in figure 8.11 and figure 4.1 obtained with data:

- The resolution as a function of p_T is described well by the simulation for high-p_T muons.

- The additional smearing reproduces a worsening of the resolution by about 0.005 for p_T above $500\,\text{GeV}$. This corresponds to a shift by one standard deviation in the highest p_T bin in figure 4.1 and confirms that this additional smearing factor can be used to estimate the resolution uncertainty.

- The $1/p_T$ resolution in simulations for η-regions inaccessible for studies with cosmic muons is slightly worse but still comparable to the region $0 < |\eta| < 0.9$.

- The gaussian smearing influences the resolution comparably in all η-regions.

Implications for the Dimuon Mass Resolution

Now that the validity of the approach is confirmed one is interested how the gaussian smearing influences the dimuon mass resolution. The same general approach as described above was applied to study the resolution in Monte Carlo events, where the sample is divided into mass bins of width $200\,\text{GeV}$ in the previously defined η regions and a gaussian function is fitted to the central region of the relative residuals w.r.t. to the generated mass. An example for this is shown in figure 8.12. The approximation of the p_T dependence uses again a linear
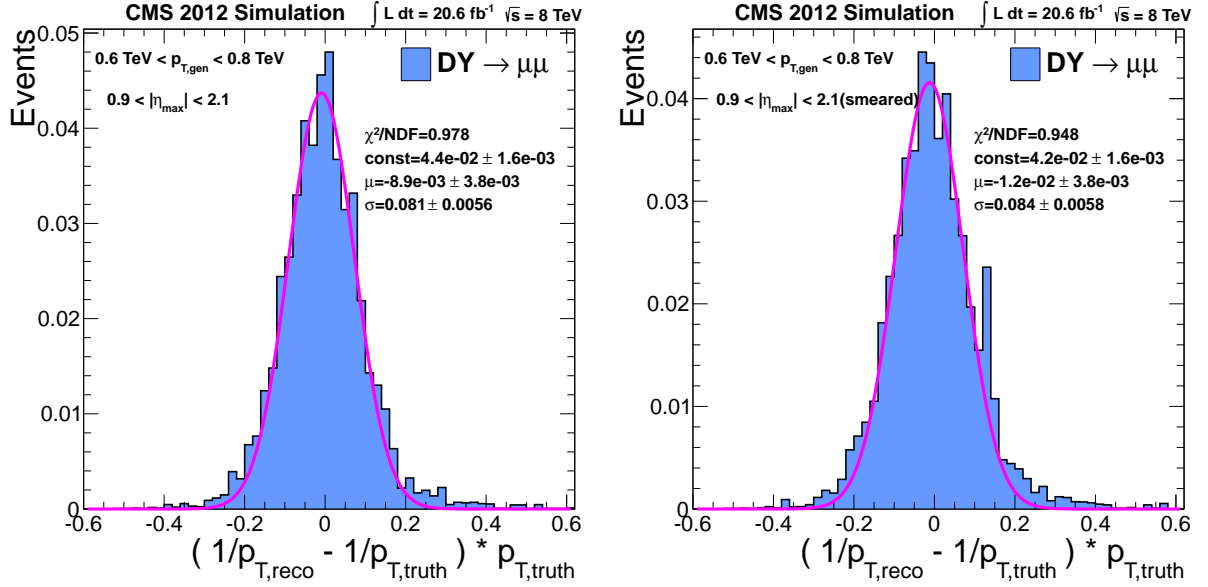
Figure 8.9.: Muon $\frac{1}{p_T}$ resolution in p_T,η bin $0.6\text{TeV} < p_T < 0.8\text{TeV}$, $0.9 < |\eta| < 2.1$ for a DY MC sample with standard (left) and smeared (right) reconstruction. The muons fulfil the single muon selection as described in section 5.2.

fit to the expected resolution in various η bins. A summary of the results is shown in figure 8.13 and it can be seen that the difference in relative resolution between normal and smeared samples varies from about 1% below 1 TeV to about 0.5% at 2 TeV.

For the uncertainty on the expected number of background and signal events the relative difference in the event yield for the invariant mass distribution with a smeared a un-smeared $1/p_T$ distribution is used. The effects for the signal distribution is found to be negligible compared to the model uncertainties. A fit is used to quantify the influence on the Drell-Yan background estimate dependent on the lower mass threshold:

$$\frac{\delta N}{N}(M_{min}) = 6.2 \cdot 10^{-3} + 4.93 \cdot 10^{-5} \frac{M_{min}}{\text{GeV}} + 3.86 \cdot 10^{-9} \frac{M_{min}^2}{\text{GeV}^2} \tag{8.3}$$
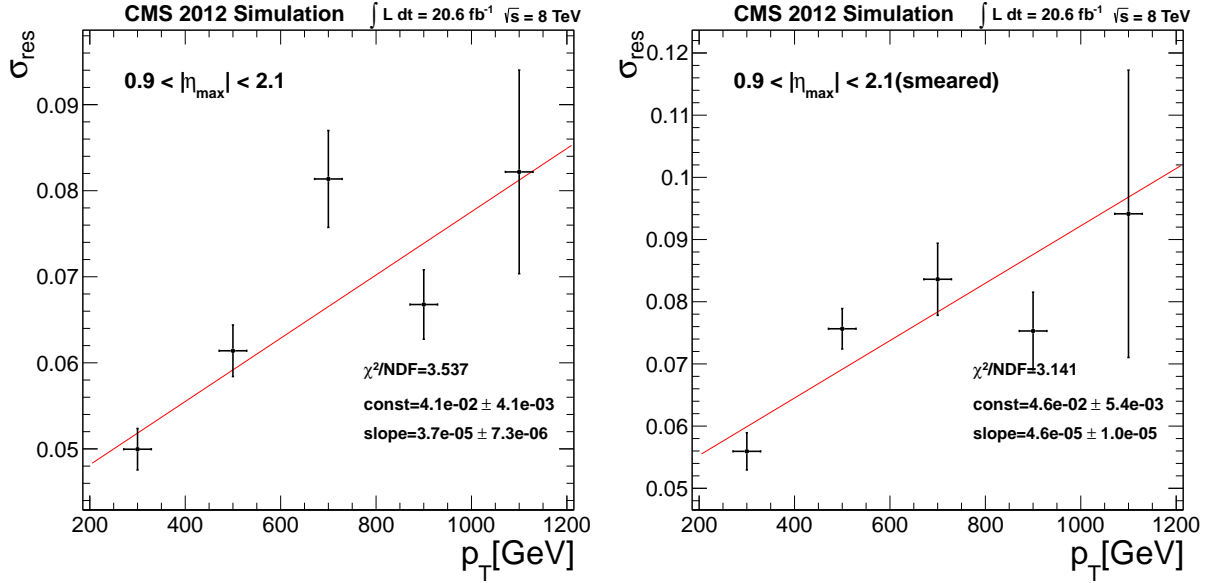
Figure 8.10.: Muon $\frac{1}{p_T}$ resolution fit width depending on p_T for muons in $0.9 < |\eta| < 2.1$ with a linaer fit for standard (left) and smeared (right) reconstruction.
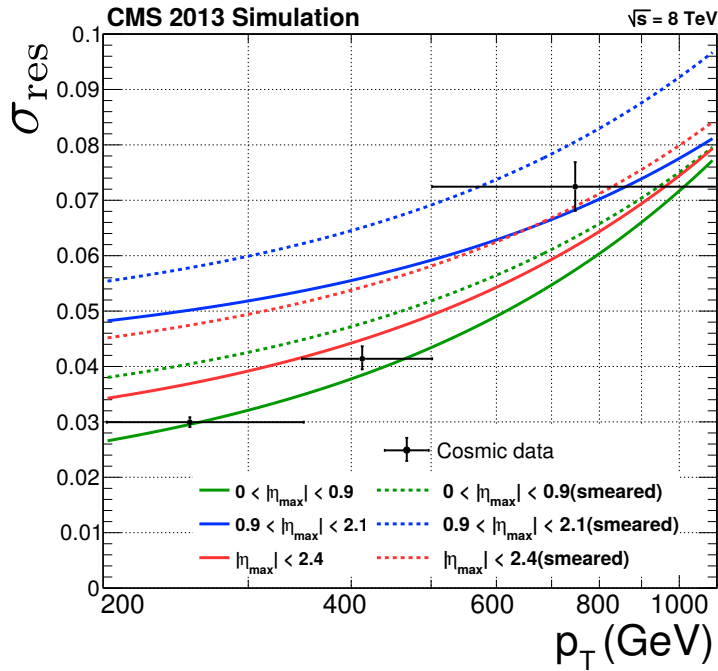
Figure 8.11.: Muon $\frac{1}{p_T}$ resolution width depending on p_T for muons in various η regions and for standard and smeared reconstruction. Also shown are 3 data points extracted from the cosmic dataset shown in figure 4.1 (Points read off with `EasyNData` [132]).
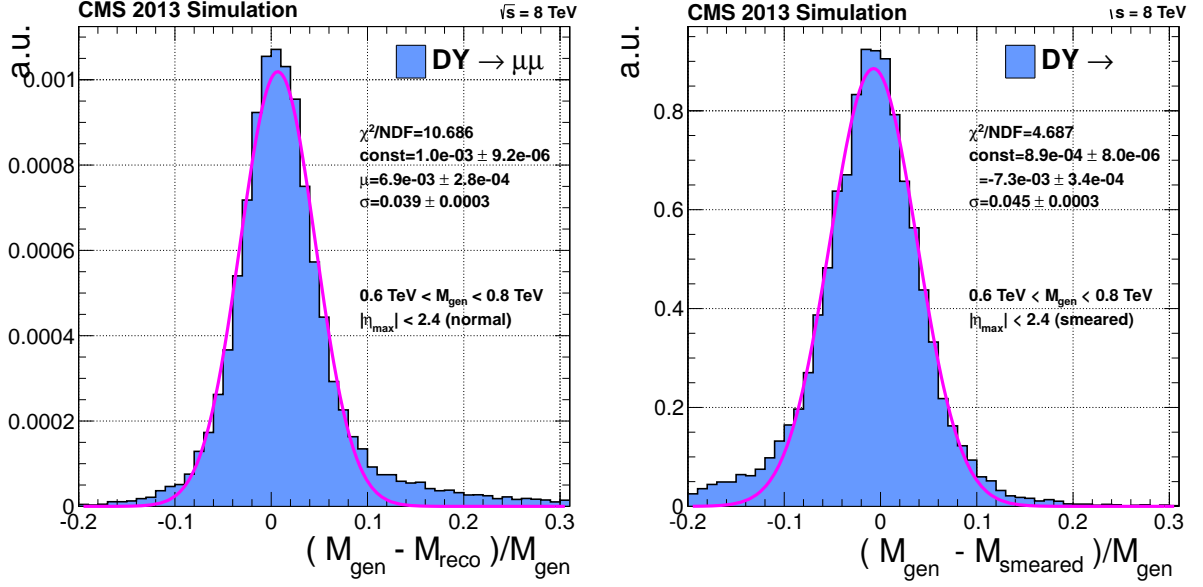
Figure 8.12.: Muon invariant mass relative residual resolution in $(M_{\mu\mu},\eta)$ bin ($0.6\text{TeV} < \text{p}_\text{T} < 0.8\text{TeV}$, $0.9 < |\eta| < 2.1$) for a DY MC sample with standard (left) and smeared (right) reconstruction.
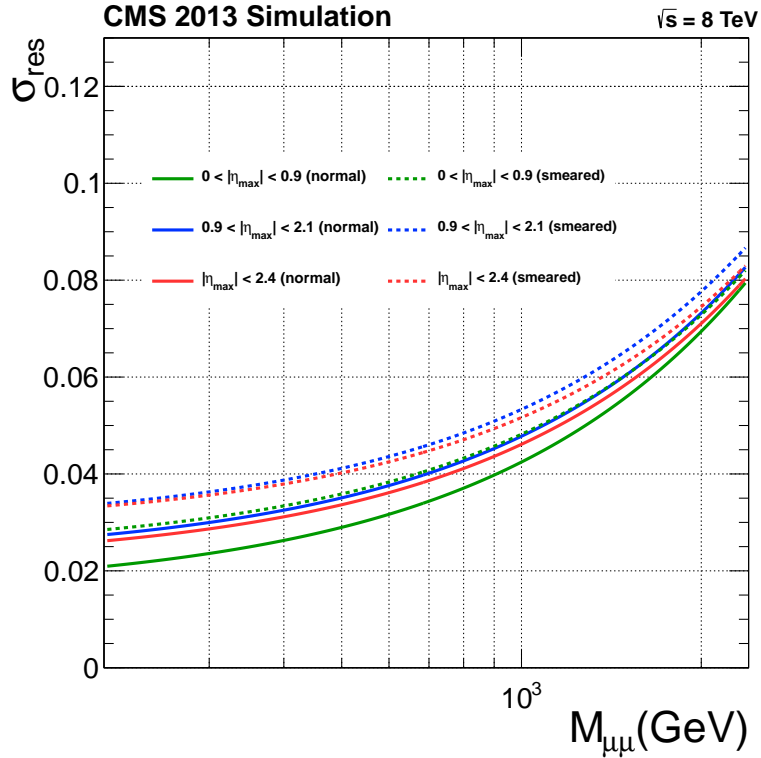
Figure 8.13.: Summary Muon invariant mass relative residual resolutions for different η regions.

9. Expected lower Limits on ADD Parameters

The parameter space of potential extra dimensions in the ADD model is large and the approach in this thesis tries to narrow the experimental allowed region down until (hopefully) only a small region with the parameter choice which is realised in nature is left. The following chapter describes how the number of observed and expected events above a lower mass limit can be used to compute upper limits on the signal cross section and translate them into lower limits on the model parameters Λ_T or alternatively (M_s, n) with a confidence level of 95%, given the case that no hints for a signal exist. A potential signal would appear as a region where the observed limit deviates significantly from the expected limit given the detector sensitivity for the signal. The upper mass threshold is limited by theoretical considerations but its influence on the upper parameter limits is rather small due to the steeply falling background spectrum. The lower mass limit on the other hand can be used to choose an optimal mass region for statistical inference about the ADD model. The theoretical ADD signal production is independent of the lepton flavour. Preliminary results for large extra dimension searches in the dielectron channel by CMS were published in [133]. The actual input for the electron channel in the following chapters was submitted in private communication by Seyed Mohsen Etesami, who studied this channel. The updated results contains only minor changes w.r.t. the published result in [133]. Both analyses were developed in a close collaborative approach and aim to use a consistent description of the ADD signal. Results from both analyses are used to calculate and optimize a combined upper cross section limit for both channels. The optimization results are discussed after a brief description of the used statistical model. All calculations rely on the Higgs combine tool [134], which is based on the RooStats software libraries [135].

9.1. Statistical Model

The choice of a statistical model requires to define how the information from the data should be described and how the description can be used to favour one of several hypotheses. This search describes the data from measurements or Monte Carlo simulations as a single bin counting experiment. Two main arguments motivate this choice instead of a shape-based approach:

- A notable separation between signal and background expectation starts in the region above 1.5 TeV (see figure 7.1). This region has only low statistics and growing uncertainties in the background shape, both from theory and detector effects.

- The ADD model predicts a non-resonant excess which does not provide a structure, e.g. a bump or edge in the spectrum. In addition it is supposed to be treated as a benchmark model for a class of theories with additional dimensions in the framework of an effective field theory. The exact signal shape created by possible extra dimensions in

nature may be quite different from the ADD prediction. Furthermore the results from a single counting experiment allow a easier reinterpretation in case one is interested in a similar model.

The comparison of the "SM" and "SM+ADD" hypothesis is performed in the framework of Bayesian statistics. The choice to use bayesian statistics for hypothesis testing is motivated in section 9.1 together with a brief introduction to the applied concepts in the later sections.

Single Bin Counting Experiment

The statistical model assumes the probability to observe N_{obs} when a events are expected to be described sufficiently well by a Poisson distribution:

$$P(N_{obs}) = \frac{a^{N_{obs}}}{N_{obs}!} \cdot \exp(-a). \tag{9.1}$$

The expectation value a of the distribution is given by the expected number of background and signal events. The sum of both mean values is calculated as:

$$a = \mathcal{L} \prod_i \epsilon_s \cdot \nu_{s,i} \cdot \sigma_s + \prod_j \epsilon_b \cdot \nu_{b,j} \cdot \sigma_b \frac{N_{obs,Z-peak}}{\sigma_{b,Z-peak}} \tag{9.2}$$

where the symbols in equation 9.1 denote:

- ϵ_s signal and ϵ_b background efficiency.

- σ_s signal and σ_b background cross sections.

- $\sigma_{b,Z-peak}$ background cross section in the normalization mass window.

- $N_{obs,Z-peak}$ number of observed events in the normalization mass window.

- $\nu_{i,s}$, $\nu_{j,b}$ Other nuisance parameters with value 1 and systematic uncertainties as described in chapter 8 and listed in 9.1.

A summary of the assigned uncertainties for the above introduced parameters is given in table 9.1 for events above the optimized mass threshold.

Bayesian statistics

The statistical model in this analysis uses a Bayesian approach for statistical inference to draw conclusions about the studied model in light of the measured data. In contrast to a frequentist approach the result does not describe the expected rate at which one would expect a outcome different from the observed result, but how the initial degree of belief in the tested hypothesis should change in the light of additional information D[1] [136, 137]. The initial believe is described by the prior-distribution $\pi(x, \nu)$, it depends on the parameter of interest (POI) x [2] and additional nuisance parameters ν. The product of prior-distribution and

---

[1]e.g. the number of observed events
[2]e.g. the signal cross section

likelihood function $L(D; x, \nu)$ can be used to calculate the posterior-distribution $\Pi(x, \nu|D)$ using Bayes' theorem [136]:

$$\Pi(x, \nu|N) = \frac{L(D; x, \nu) \cdot \pi(x, \nu)}{\int L(D; x', \nu') \cdot \pi(x', \nu') d\nu' dx'} \tag{9.3}$$

If the nuisance parameters are used to model systematic uncertainties, one is mainly interested in the marginal posterior distribution w.r.t. to x:

$$\Pi(x|N) = \frac{\int L(D; x, \nu) \cdot \pi(x, \nu) d\nu}{\int L(D; x', \nu') \cdot \pi(x', \nu') d\nu' dx'} \tag{9.4}$$

In the case of a single bin counting experiment the 95% credible regions for the upper limit on the POI x' can be calculated using the equation:

$$0.95 \overset{!}{=} \int_0^{x'} \Pi(x|D) dx \tag{9.5}$$

All nuisance parameters are modelled as log-normal distribution with mean 1 and a width corresponding to the assigned relative uncertainty. Log-normal distributions can be used to model processes which consist of various independent random processes which can be combined by multiplication. This reflects that the studied uncertainties describe complex effects which are consequences of various underlying independent processes [138].

The prior function for the POI is modelled with a uniform distribution [0,c) in the limit $c \to \inf$. A flat prior ensures a certain objectivity about the model, but still some information about the model enters the distribution as the information that all outcomes are equal likely contains prediction about the expected structure of the state space. It may be argued that a more sophisticated function which minimizes the prior information content may be more suitable and other approaches are currently introduced into high energy physics [139]. The proposed functions are, in contrast to a flat prior, transformation-invariant. This means that the prior function is not affected by redefinitions of the POI. The lack of transformation invariance for flat priors leads to the undesirable effect that a credible region A for a POI x which corresponds to a posterior probability $P(x \in A)$ may result in a different posterior probability for the same dataset if the POI is scaled by a factor $\eta = cx$) (e.g. to change units):

$$P(\eta \in A) = P(x \in c^{-1}A) \neq P(x \in A) \tag{9.6}$$

Despite these disadvantages flat priors are widely used as they result in same or very similar results as a frequentist approach which makes a later comparison with other experimental results easier.

Combination of Search Channels

The introduction of this chapter mentioned a combined limit on the electron and muon channels. Such a combination can be done by replacing the single channel likelihood function

L in equation 9.3 with the full likelihood L_{full}:

$$L_{full}(D, x, \nu) = \prod_{j=1}^{N_{channels}} \prod_{i=1}^{N_{events}} L_j(D, x, \nu). \qquad (9.7)$$

The result obtained with the full likelihood function L_{full} can be further improved if correlations between systematic uncertainties are take into account. A common example for this are PDF uncertainties, where the uncertainty is not influenced by the final state and is thus fully correlated for the electron and muon channel.

Markov Chain Monte Carlo

The number of dimensions in equations 9.3-9.5 rises with the number of nuisance parameters and common methods for numerical integration, which rely on a dynamic adjustment of the sampling area size (e.g. rejection-sampling [136], importance sampling [140]), soon grow to be inefficient. In this analysis Markov-Chain Monte Carlo (MCMC) methods are used to numerically solve these integrals with the Metropolis-Hastings algorithm [141]. Algorithms of this class use correlated random variables, where each random variable is generated according to a symmetric probability density[3] $q(\theta^i, \cdot)$ around the last value. The algorithm can be briefly described in four steps [137][4]:

1. Initialize the iteration with iteration counter 1 at arbitrary seed value θ^i.

2. Generate a new value $\theta^{proposed}$ according to the chosen density $q(\theta^i, \cdot)$ and last chain entry θ^i.

3. Evaluate the acceptance probability $\alpha(\theta^i, \theta^{proposed}) = \min\left\{1, \frac{\pi(\theta^{proposed})}{\pi(\theta^i)}\right\}$, where the integrand is denoted $\pi(\theta)$. Dice a value p between 0 and 1. If $p < \alpha$ add $\theta^{proposed}$ to the chain, otherwise add θ^i again.

4. Add one to the iteration counter and return to step 2 until the convergence criteria are fulfilled.

The chain will reach an equilibrium state independent from the seed value for $n \to \infty$ if the chosen "step" density has a sufficient step width or wide tails. This ensures that a chain may reach all parts of the state space [137].

9.2. Optimization of the Lower Mass Cut

Given the effort which was invested to gather the experimental results it is favourable to gain the maximum information from the data set. The single bin counting experiment has only starting and end points as parameters for a optimization towards this goal. No improvement

---

[3]E.g. a gaussian distributions [134].
[4]This may be called a "slightly drunk sailor" problem, where the sailor reflects for a second if the next step may lead him into the harbour basin

9. Expected lower Limits on ADD Parameters

for the limits is expected when M_{max} is lowered below the theoretical validity range, which leaves the lower mass threshold M_{min} as the only left parameter for a optimization. This section requires to calculate expected upper limits within the statistical model. The expected limit is defined as the median limit in ~ 4500 toy experiments, where the input value for N_{obs} in equation 9.1 is diced according to a Poisson distribution describing the SM expectation. The optimization of the lower mass threshold was performed for the muon and the combined prediction $(e + \mu)$ separately and uses a simplified approach where the calculation is repeated for different values of M_{min} with a fixed distance of $100\,\text{GeV}$. Systematic uncertainties for the choice of PDFs, higher order corrections and luminosity are flavour or even process independent and are thus treated as fully correlated in the calculation of combined limits. All other uncertainties are modelled as uncorrelated.

The expected cross section times branching ratio limits as a function of M_{min} are shown in figure 9.1 for all cases (muon, electron, combined). Steeper drops for higher masses occur when the median expected number of events changes between integer values close to zero. The expected number of background events and the corresponding median from 100k Poisson distributed random numbers as a function of M_{min} are shown on the right side of figure 9.1 effect. The comparison of both plots in figure 9.1 shows that the best cross section limit is reached when the median number of expected events (in 4500 toys) reaches zero. The limit for higher values get gets worse because the signal expectation is further reduced while the background expectation stays constant. It can be seen that electrons are measured with a better resolution at high masses, which results in a slightly better cross section limit for the electron channel [133].
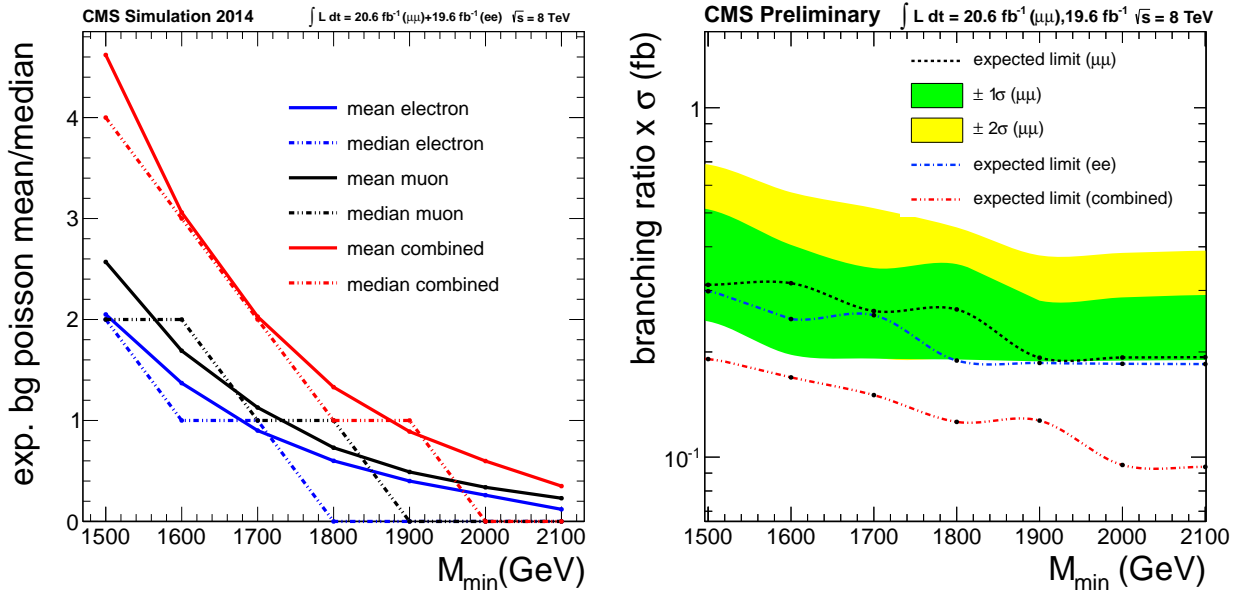
Figure 9.1.: (Left) Mean (solid) and median (dashed) expected number of background events as a function of M_{min}. (Right) Expected cross section limit for a ADD signal: dimuon (black), dielectron (blue) and combined (red) channel. In addition 1σ (green) and 2σ (yellow) uncertainty bands are shown for the dimuon channel. Both statistical and systematic errors are included.

The calculated cross section limits were compared to the ADD signal expectation for

different values of Λ_T. A log-linear fit is used to estimate a more precise value of Λ_T if the expected cross section limit is found in between two of the simulated ADD signal cross sections.

The expected limit was also studied for various choices for the upper mass threshold M_{max}, where the limited validity of the effective theory is taken into account by the constraint $M_{max} \leq \Lambda_T$, $M_{max} \leq M_S$ for the HLZ and GRW conventions, respectively. The expected limit on Λ_T as a function of M_{min} is shown in figure 9.2 for different values of M_{max}. Only values with $M_{max} \leq \Lambda_T$ are included and it can be observed, that the best value can be obtained with the highest allowed value $M_{max} = \Lambda_T$.

Figure 9.2 also includes the limits on Λ_T if the effects from systematic uncertainties are neglected. The PDF uncertainty dominates for the electron channel and is only relevant for the muon channel for smaller values of M_{min} [133]. The muon scale uncertainty rises faster than the PDF uncertainties and the effects from systematic uncertainties are already visible, but still small ($\sim 1\% - 2\%$ on the limit for Λ_T). The combined limit is almost not affected by systematic uncertainties.

The M_{min} value corresponding to the highest expected combined lower limit on Λ_T is then used as the optimized mass cut. The optimized value for different choices of M_{max} is shown in figure 9.2, where $M_{min,opt} = 1.9\,\text{TeV}$ for the muon, $M_{min,opt} = 1.8\,\text{TeV}$ for the electron and $M_{min,opt} = 2.0\,\text{TeV}$ for the combined case can be read off. The optimized M_{min} for the combined channel is used in the calculation of observed limits in the following chapters and the systematic uncertainties on the signal and background expectation for this choice are listed in table 9.1.

Systematic Uncertainty	Value [%] signal		Value [%] background		Comment
	$> 1.9\,\text{TeV}$	$> 2.0\,\text{TeV}$	$> 1.9\,\text{TeV}$	$> 2.0\,\text{TeV}$	
Luminosity	2.6	2.6	-	-	see section 8.1.1
NNLO QCD DY	-	-	3.0	3.0	see section 8.2.1
NLO EW DY	-	-	5.0	5.0	see section 8.2.2
PDF	-	-	20.7	22.1	see section 8.3
Normalization & efficiency	-	-	3.0	3.0	see section 8.2.3
Signal efficiency	3.0	3.0	-	-	see chapter 7
Momentum scale	10.6	11.1	41.0	44.9	see section 8.4.2
Momentum resolution	—	—	11.4	12.0	see section 8.4.3
Muon system alignment	5.0	5.0	5.0	5.0	see section 8.4.1

Table 9.1.: Summary of systematic uncertainties on the signal and background yield for the optimized muon ($e + \mu$ combined) lower mass threshold $M_{min} > 1.9\,\text{TeV}$ ($M_{min} > 2.0\,\text{TeV}$)

9. Expected lower Limits on ADD Parameters
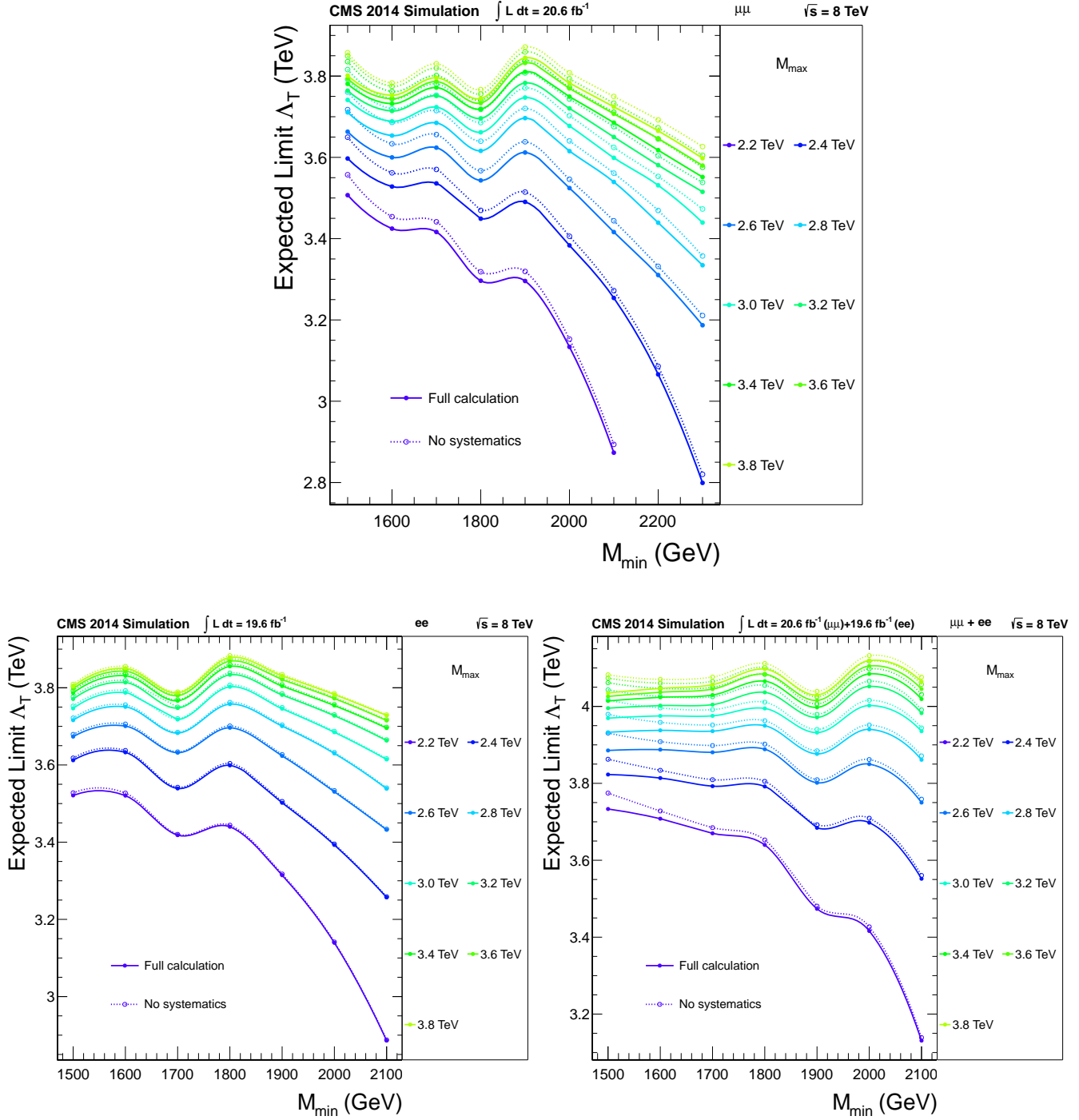
Figure 9.2.: Expected lower limit on Λ_T for the muon channel (upper row), the electron channel (lower left) and the combined $e + \mu$ channel (lower right) as a function of M_{min}. The implemented ADD model has a limited validity and only values with $M_{max} \leq \Lambda_T$ are included.

10. Evaluation of Observed Events with Two Muons

This chapter presents the observed number of events in the full $8\,\mathrm{TeV}$ muon dataset with an integrated luminosity of $\mathcal{L} = 20.6\,\mathrm{fb}^{-1}$. The number of observed events in a bin is assumed to be drawn from a Poisson distribution, and the error bars in the following plots represent a 68% confidence region if the number of observed events is assumed to be the mean of the distribution. The calculation follows one of the approximations discussed in [142] to determine the confidence interval:

$$\left(\frac{1}{2}Q(0.16, 2N_{obs}); \frac{1}{2}Q(0.84, 2(N_{obs} + 1)) \right) \tag{10.1}$$

where $Q(x, k)$ is the x-quantile of the χ^2 distribution with k degrees of freedom. The choice to use asymmetric errors is emphasised by the CMS statistics committee[143] and motivated by the fact that a Poisson distribution with mean λ has a variance of λ, but the interval $[\lambda - \sqrt{\lambda}, \lambda + \sqrt{\lambda}]$ may include considerably less than 68% of the complete probability distribution (undercoverage), this effect is larger for a mean close to zero. The chosen approach on the other hand is known to cover always at least 68% of the distribution (overcoverage).

10.1. Kinematic Variables of the Dimuon System

Before the final invariant mass distribution is studied, it is reasonable to check some kinematic variables of the dimuon system and search for potential deviations between data and SM simulation caused by unexpected effects. Figure 10.1 shows distributions for the muon angle in the transverse plane ϕ and the pseudo-rapidity η. It can be seen that the simulation describes the observed spectra well in all directions within the acceptance. The transverse momentum p_T is shown in figure 10.2 with and without a cut on the dimuon invariant mass $M_{\mu\mu} > 500\,\mathrm{GeV}$. It can be seen that the signal to background ratio rises in the high p_T tails, yet the sensitivity in this variable is much lower than in the dimuon mass distribution. Figure 10.3 shows the spectra for $cos(\theta^*)$ again with and without a mass cut $M_{\mu\mu} > 500\,\mathrm{GeV}$. The variable θ^* was introduced in equation 1.27 as the scattering angle of the positively charged muon in the dimuon center of mass frame. It can be seen that the signal favors smaller values for $cos(\theta^*)$ as it is expected from the calculations in [26]. The reasons for these different expectations is discussed in section 2.2.1.

10.2. Evaluation of the Dimuon Invariant Mass Spectrum

Various cross checks and the previous control plots showed that the dimuon system is well understood and one may proceed to study the dimuon invariant mass spectrum. The number of observed and expected events in different mass regions are listed in table 10.1. The

observed number of events is in good agreement with the SM expectation and the largest deviation taking only statistical errors into account is observed in the region from $0.4 \, \text{TeV} - 0.6 \, \text{TeV}$ with a value of 1.6σ. Two events are observed in the previously defined search region $M_{\mu\mu} > 1.8 \, \text{TeV}$ where approximately one event is expected, event displays for these events are shown in appendix C.2.

It can be seen that the top backgrounds run out of statistics in the high mass tails and a single entry for this background determines the statistical error in the search region.

The complete spectrum is shown in figure 10.4 together with the SM expectation and the data to simulation ratio. The results are presented with a variable binning where the value of a bin is given w.r.t. a fixed bin size of $1 \, \text{GeV}$. The y-axis values for a bin can be transformed into a number of events by multiplication with the bin size. The variable bin size is chosen to reflect the decreasing mass resolution for high mass muons as studied in section 8.4.3. The lower part of the figure shows the relative residuals with a different binning. Here the binning is chosen to merge bins until at least 20 Monte Carlo events are contained in the resulting bin. This method ensures that only estimates with a reasonable precision enter the illustration.

The search for a resonant excess in the dimuon spectrum [92] applied the same selection criteria as this analysis and a event by event comparison was performed for events above 900GeV. No deviations were found. Both analyses use an independently developed analysis framework and this cross check reduces the possibility for unwanted bias [1] for both approaches to a minimum. The list of events with invariant mass, some kinematic properties and CMS internal event identifiers are listed in appendix C.1.

In conclusion no significant deviations from the SM expectation in the dimuon mass spectrum at $8 \, \text{TeV}$ are observed and the obtained numbers may be used to calculate lower limits on model parameters.

Mass Range (TeV)	Observed events	Total SM background	Drell-Yan	$t\bar{t}$ & single top	Diboson
0.1 − 0.4	96959	97075±431	87168±427	8083±45	1784±13
0.4 − 0.6	1376	1446±18	1166±16	210±7	71±2
0.6 − 0.8	237	241±3	208±1	21±2	12±1
0.8 − 1.0	66	61.9±1.4	53.1±0.3	4.9±1.2	3.9±0.6
1.0 − 1.3	25	23.1±0.3	20.3±0.1	1.5±0.6	1.3±0.3
1.3 − 1.6	7	5.39±0.21	4.43±0.04	0.55±0.24	0.41±0.21
1.6 − 1.9	3	1.20±0.04	1.16±0.01	0.00±< 0.01	0.04±0.04
> 1.9	0	0.495±0.003	0.495±0.003	0.00±< 0.01	0.00±< 0.01

Table 10.1.: Number of observed and expected events in different mass regions for the full 2012 dataset. Uncertainties on the background expectation are statistical and assume to be poisson distributed.

---

[1]e.g. coding errors, missed parts of the dataset etc.
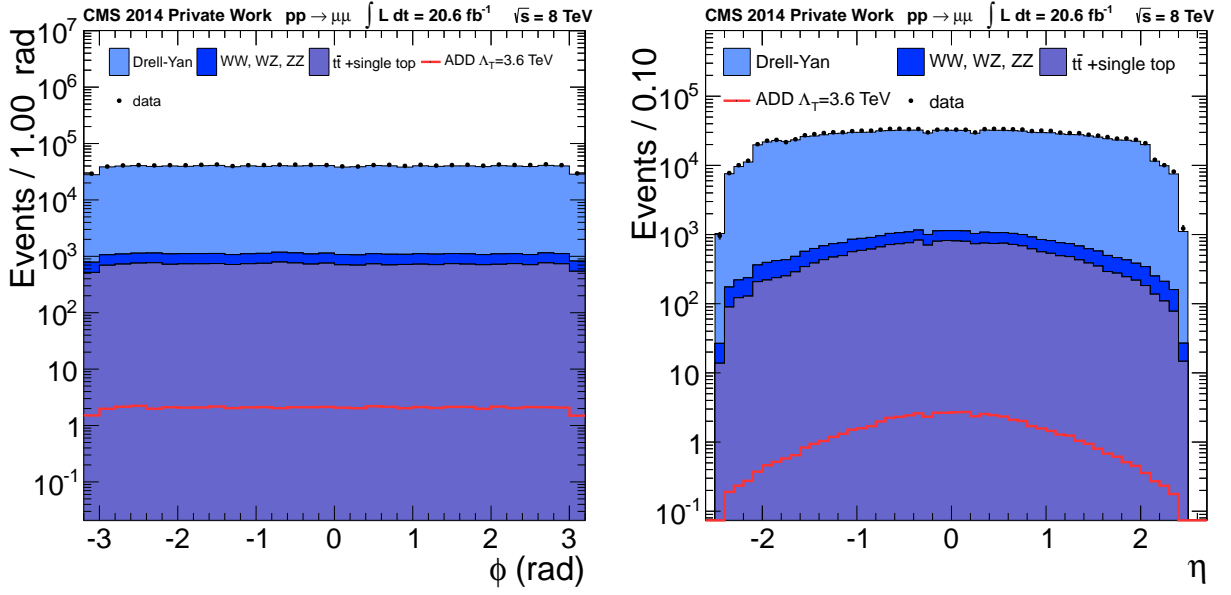
Figure 10.1.: Observed and expected spectra for transverse angle ϕ (left), pseudo-rapidity η (right). The ADD sample consists of SM LO-DY expectation, ADD signal and interference contributions and is produced with a mass cut $M_{\mu\mu} > 1050\,\text{GeV}$.
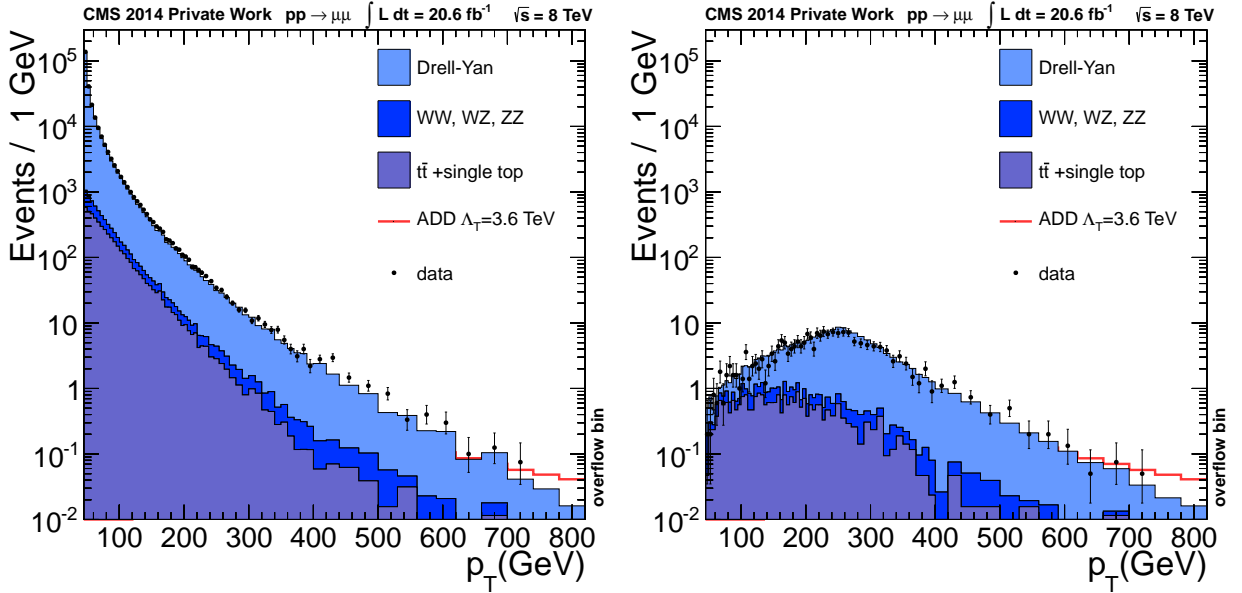
Figure 10.2.: Observed and expected spectra for the transverse momentum p_T without a cut on $M_{\mu\mu}$ (left) and with a cut $M_{\mu\mu} > 500\,\text{GeV}$. The ADD sample consists of SM LO-DY expectation, ADD signal and interference contributions and is produced with a mass cut $M_{\mu\mu} > 1050\,\text{GeV}$.
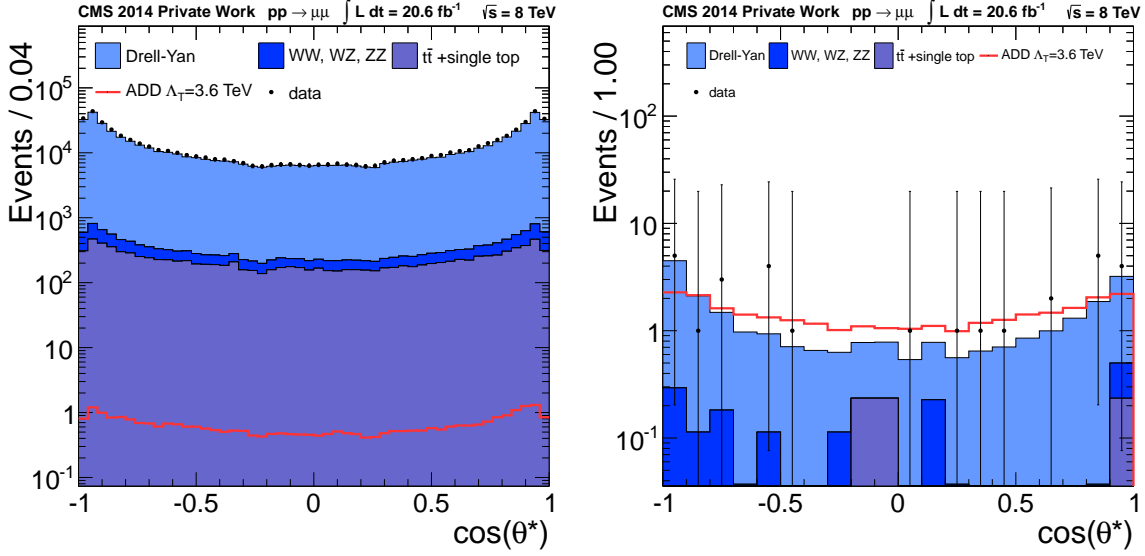
Figure 10.3.: Observed and expected spectra for $\cos(\theta^*)$ without a cut on $M_{\mu\mu}$ (left) and with a cut $M_{\mu\mu} > 500\,\text{GeV}$. The shown ADD signal is generated with a lower mass threshold $M_{\mu\mu} > 1050\,\text{GeV}$
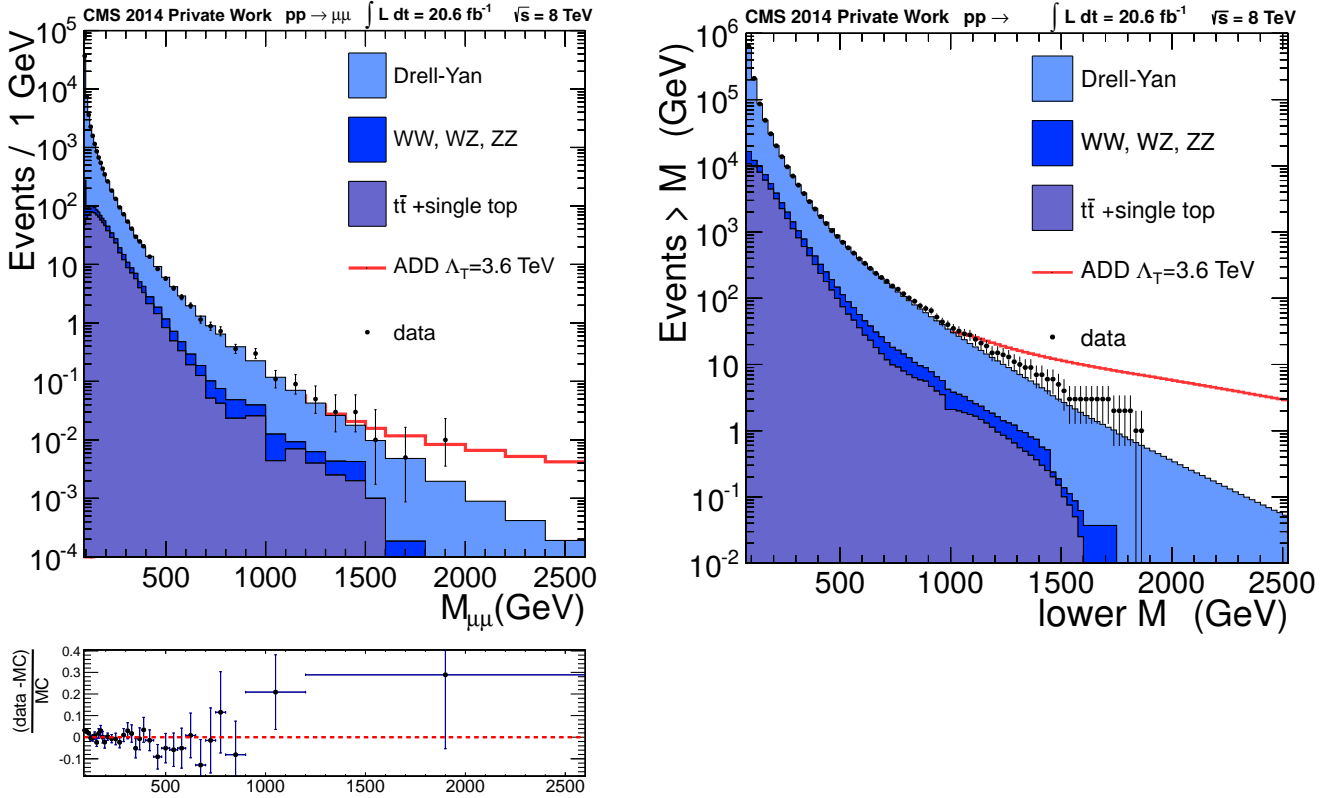
Figure 10.4.: Observed dimuon invariant mass spectrum (dots) together with the SM expectation (filled areas) (left: differential, right cumulative). The bin values are calculated w.r.t. a fixed bin size of 1GeV and the bin width reflects the muon mass resolution in the left plot. The lower part of the left plot shows relative residuals for simulation and data, where bins are merged until at least 20 Monte Carlo events are contained.

11. Observed Limits on ADD Parameters

The last chapter concluded that a sufficient level of confidence in the understanding of the dimuon spectrum is reached and that no evidence for a signal is found. This motivates the calculation of upper limits on the signal cross section in the previously defined search regions $M_{min} > 1.9$TeV ($M_{min} > 2.0$TeV). The obtained cross section limit is reinterpreted in terms of lower limits on the ADD model parameters. The calculation of observed limits uses a single bin counting experiment with a bayesian approach for statistical inference as described in section 9.1. Limits are estimated at 95% confidence level as explained in equation 9.5 where the signal cross section serves as the parameter of interest. Signal efficiencies stay stable for different values of Λ_T, and values of 80.0% (muons) and 82.7% (electrons) are used to calculate signal cross section limits. The observed (expected) cross section limit is 0.19 fb (0.19 fb) for the dimuon and 0.09 fb (0.09 fb) for the combination of the dimuon and dielectron results.
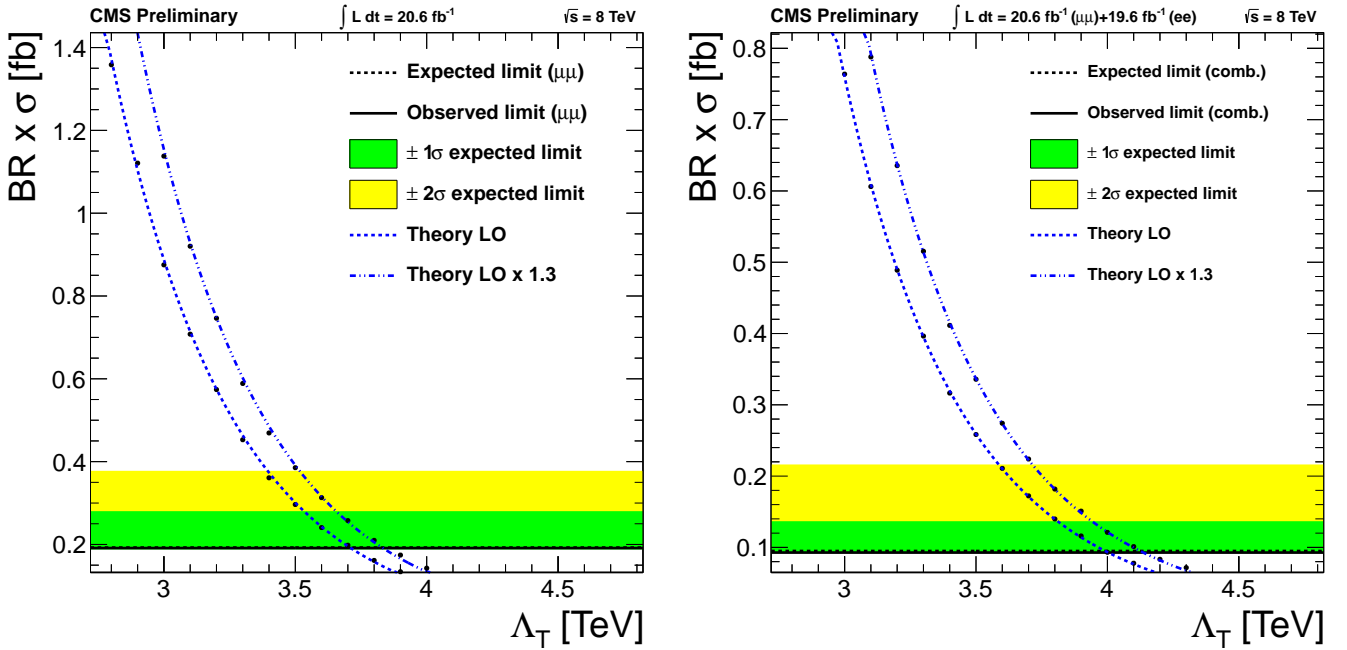
Figure 11.1.: Observed and expected cross section limits for the dimuon channel with $M_{\mu\mu} >$ 1.9TeV (left) and the combined (right) channel ($e+\mu$) with $M_{ll} > 2.0$TeV. The ADD theory cross section is shown for the LO and NLO QCD expectation.

The resulting limits on Λ_T can be read off from the intersection points of theory expectation and observed (expected) cross section limit in figure 11.1, as listed in table 11.1 together with a reinterpretation of the results in the HLZ convention (see described section 2.2.1) for the LO and the NLO signal estimate. Table 11.1 shows that the presented approach results in limits on M_s between 4.9 TeV and 4.9 TeV dependent on the number of extra dimensions.

11. Observed Limits on ADD Parameters

HLZ limits for n=2

The case $n = 2$ is not included in the already given transformation formulae between GRW and HLZ convention in equation 2.17 and requires a bit more effort because an additional dependence on the center of mass energy $\hat{s}$ given by the dimuon mass is introduced. It is thus necessary to calculate the differential cross section $\frac{d\sigma(M_s, 2)}{dM}$. The already simulated mass dependent distributions Λ_T were used for this using the relation:

$$\Lambda_T^4(M, M_s) = \frac{M_s^4(M)}{\log\left(\frac{M_s^2(M)}{M^2}\right)} \tag{11.1}$$

Distributions are calculated for M_s in 100 GeV steps. The corresponding Λ_T for each value of M_s, M is obtained with equation 11.1 and the corresponding cross sections for this Λ_T is used to fill the (M_s, n) bin with mass M:

$$\left.\frac{d\sigma(M_s, 2)}{dM'}\right|_{M'=M} = \left.\frac{d\sigma(\Lambda_T(M_s, M))}{dM'}\right|_{M'=M}$$

The obtained differential cross sections are then compared to the cross section limit to obtain a limit on $(M_s, n = 2)$, where M_{max} is set to M_s. The last step is similar to the limit setting procedure for Λ_T.

ADD k-factor	Limit type	Λ_T [TeV] (GRW)	M_s [TeV] (HLZ)					
			$n=2$	$n=3$	$n=4$	$n=5$	$n=6$	$n=7$
$\mu\mu$, $M_{\mu\mu} > 1.9$ TeV $\sigma_{\mathrm{s}} < 0.19$ fb (0.19 fb expected) at 95% CL								
1.0	expected	3.7	3.5	4.4	3.7	3.4	3.1	3.0
1.3		3.8	3.7	4.6	3.8	3.5	3.2	3.1
1.0	observed	3.7	3.5	4.4	3.7	3.4	3.1	3.0
1.3		3.8	3.7	4.6	3.8	3.5	3.2	3.1
ee, $M_{ee} > 1.8$ TeV $\sigma_{\mathrm{s}} < 0.18$ fb (0.19 fb expected) at 95% CL								
1.0	expected	3.8	3.7	4.5	3.8	3.4	3.2	3.0
1.3		3.9	3.9	4.6	3.9	3.5	3.3	3.1
1.0	observed	3.8	3.8	4.5	3.8	3.4	3.2	3.0
1.3		3.9	3.9	4.6	3.9	3.5	3.3	3.1
ee and $\mu\mu$, $M_{ll} > 2.0$ TeV $\sigma_{\mathrm{s}} < 0.09$ fb (0.09 fb expected) at 95% CL								
1.0	expected	4.0	3.9	4.7	4.0	3.6	3.4	3.2
1.3		4.1	4.1	4.9	4.1	3.7	3.5	3.3
1.0	observed	4.0	3.9	4.8	4.0	3.6	3.4	3.2
1.3		4.1	4.2	4.9	4.1	3.7	3.5	3.3

Table 11.1.: Observed and expected 95% lower limits in the dilepton channels and the combied case at 95% CL within GRW and HLZ conventions for a truncated signal at $M_{\mathrm{max}} = M_s$ (HLZ) or $M_{\mathrm{max}} = \Lambda_T$ (GRW).

11.1. Comparison with Previous Results

The presented exclusion limits extends the observed limits on Λ_T by 0.6TeV for the muon and 0.5TeV for the combined case compared to the previous best collider results [97] (The ATLAS search in [97] uses $ee+\mu\mu+\gamma\gamma$ channel to calculate a combined result). This previous result represents the best published limits on Λ_T and the presented analysis thus extends the experimental constrains on the ADD model. A comparison of the presented results with previous searches at collider experiments [95, 96, 97] is shown in figure 11.2. Both Atlas and CMS results use NLO k-factors to scale the signal. The [7]TeV ATLAS result applies a k-factor of 1.6 while the results from this analysis chose to use a rather conservative k-factor of 1.3.
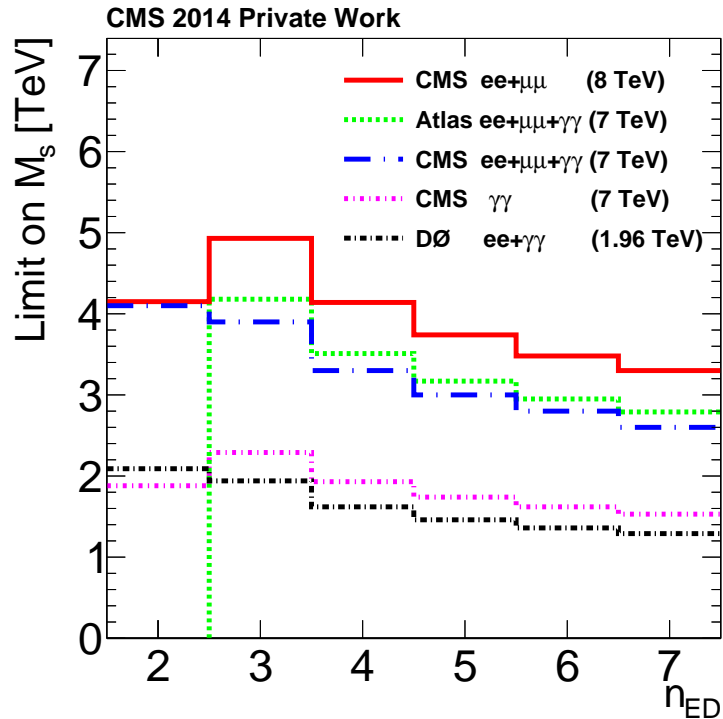
Figure 11.2.: Summary of observed limits on M_s for different numbers of additional dimensions obtained in previous searches with various collider experiments [95, 96, 97] and the result as shown in table 11.1 (red).

11.2. Implications for the Higgs Mass Hierachy Problem

Section 1.2.3 introduced the higgs mass hierarchy problem and it was argued, that the ultraviolet cut-off in equation 1.31 might be lowered enough by additional dimensions to reach a acceptable fine tuning. This raises the question: how can fine tuning be quantified? An intuitively built measure was developed in [144]:

$$f(\Lambda)) = \frac{\Delta m_h^2}{m_h^2} \approx 3.3 \frac{\Lambda^2}{\text{TeV}} \tag{11.2}$$

11. Observed Limits on ADD Parameters

where f describes that a fine-tuning of 1 in f is needed to ensure a stable higgs mass, when only one loop corrections (see equation 1.31) are taken into account. In order to calculate values for the fine tuning measure f it is necessary to identify the ultraviolet cut-off Λ in equation 11.2 with ADD model parameters. A possible choice would be the validity range of the effective theory given by M_s. One may argue that the validity range of the theory exceeds the fundamental planck mass $M_{pl}^{(4+n)}$ where additional quantum gravitational processes may be relevant. While no fundamental relation between M_s and $M_{pl}^{(4+n)}$ exists it is still possible to relate both based on unitarity arguments or similar initial definitions. One commonly used relation [145, 97] for the string scale M_s as defined in the HLZ convention[31] with the fundamental Planck scale $M_{pl}^{(4+n)}$ is given by:

$$M_s = 2\sqrt{\pi}[\Gamma(n/2)]^{\frac{1}{n+2}} M_{pl}^{(4+n)} \tag{11.3}$$

Table 11.2 lists the observed limits on M_s together with the value for $M_{pl}^{(4+n)}$ following equation 11.3 and the resulting fine tuning measures f_1 and f_2 for $\Lambda = M_s$ and $\Lambda = M_{pl}^{(4+n)}$, respectively. It can be seen that f_1 reaches values where one might argue that the ADD model starts to loose its appeal as a solution for the higgs mass hierarchy problem, while f_2 suggests that realisations of the model are still possible which result in acceptable fine tuning. The presented comparison shows that a a direct comparison of the obtained results strongly depends on the chosen definition of M_s and Λ. The chosen measure for the fine-tuning struggles with some problems, because the parameter space of the underlying theory is not correctly taken into account and the measure is not directly related to statistical quantities and the result can not be interpreted in terms of probabilities. In the past this question was often answered with intuitively built measures, e.g. the approach above or the Barbieri, Giudice measure [146]. These measures lack a consistent interpretation in terms of statistical quantities, but recent developments using the framework of Bayesian statistics introduce a method to quantify naturalness in terms of Bayesian probabilities [147, 148].

	Number of extra dimensions				
	3	4	5	6	7
observed limit M_s (TeV)	4.9	4.1	3.7	3.5	3.3
f_1	79	55	45	40	36
observed limit $M_{pl}^{(4+n)}$ (TeV)	1.4	1.2	1.0	0.9	0.8
f_2	6.6	4.4	3.3	2.7	2.2

Table 11.2.: Limits on fundamental planck scale and corresponding level of fine tuning f_1 and f_2.

12. Conclusion & Outlook

The aim of this thesis was to find additional spatial dimensions in the context of the ADD model . No evidence has been found with the CMS experiment at 8 TeV with the full dataset recorded in 2012. The presented search studied particles with up to now unreachable energies and a detailed study of theoretical and experimental sources of uncertainty was conducted. No previous measurements give an estimate for the expected background contributions at energies in the TeV range and a careful and detailed simulation of these contributions was necessary, relying only on simulated background expectations. Lower limits on the ADD model parameters were calculated, given that no evidence was found. The lower limit of $\Lambda_T = 4.13$ TeV for the combined electron and muon result represents the currently world best available constraint on the virtual graviton exchange in the ADD model. It was found that future searches start to investigate in a part of the model parameter space where one might argue that the ADD model is no satisfactory solution for its initial motivation, the higgs mass hierarchy problem, dependent on the definition of the ultra-violet cut-off for higgs mass loop contributions. Yet extra dimensions are still an attractive subject to study as they are relevant in many developments beyond the standard model. The next section presents some considerations about the sensitivity for ADD models to be expected in future LHC runs. The final section gives some suggestions for open questions which could not be answered within the scope of this thesis.

12.1. Projections for Future Searches

The preparations for the LHC Run II at $\sqrt{s} \sim 13$ TeV are currently ongoing, yet it is possible to give a rough estimate how the limit will rise given the unfortunate situation that still no evidence for extra dimensions is found. Current studies expect a single muon trigger p_T threshold at around 50GeV [149] and it is expected that the LHC produces an integrated luminosity of about $300 \, \text{fb}^{-1}$ in the first few years after the shutdown. A rough estimate for the expected limit on Λ_T at 14 TeV was calculated under the following assumption:

- All uncertainties remain unchanged except for the muon momentum scale uncertainty, which is adjusted to the lower mass threshold and calculated with equation 8.2. While most of the uncertainties will probably rise (e.g. PDF uncertainties) it is reasonable to neglect the effects as the scale uncertainties dominates clearly at such high energies (see chapter 8).

- The Drell-Yan background dominates and the effects from other backgrounds are neglected for this estimate.

- The complete calculation is done at LO.

New Drell-Yan and ADD samples with `Pythia8` at 14TeV were produced, and one example for the resulting distributions together with the ADD signal after subtraction of the LO Drell-Yan estimate are shown on the left side of figure 12.1 for $\Lambda_T = 6$ TeV. The limit was then calculated similar to the approach in chapter 9 for different lower mass thresholds M_{min};

the result is shown on the right side in figure 12.1. The first scan used only few parameter points and the simulation was then extended with additional ADD samples with values of Λ_T close to the expected maximum. It can be seen that the expected limits for the muon channel reach a plateau at $\Lambda_T = 7.6\,\text{TeV}$ for lower mass thresholds $3.5\,\text{TeV} < M_{min} < 4.5\,\text{TeV}$. The presented calculations emphasis future studies at $14\,\text{TeV}$ and it is expected that the limits on ADD models can be significantly extended if extra dimensions do not exist or are otherwise hidden by nature.
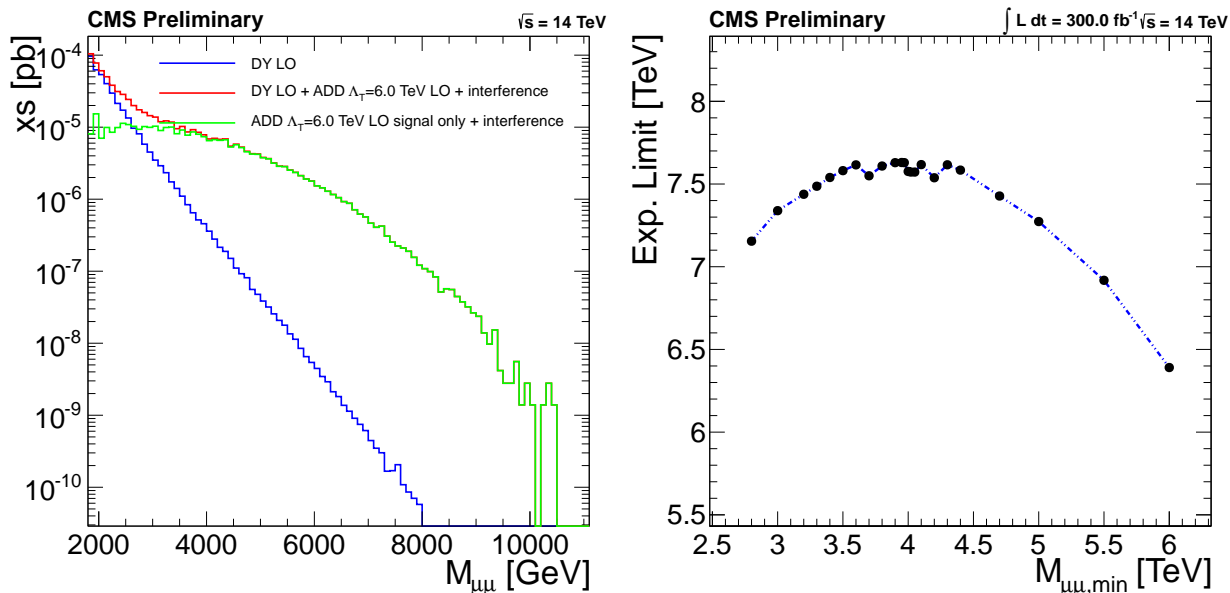
Figure 12.1.: (Left) Simulated cross section for LO Drell-Yan and a ADD model with $\Lambda_T = 6\,\text{TeV}$ where LO contributions from Drell-Yan are also included (red) and subtracted (green). (Left) Expected lower limit on Λ_T dependent on M_{min}

12.2. Suggestions for Following Studies

This section summarizes some ideas for future studies which could not be studied in the scope of this thesis:

- The asymptotic safety scenario tries to solve some of the problems which arise when gravity needs to be renormalized up to the highest energies by introducing a ultra-violet fixed point in the evolution of the couplings (β-functions) [150]. The effects of such a UV-fixed point in the ADD model was discussed in [151]. A version of the ADD model which takes effects of asymptotic safety into account was implemented in a modified version of `Pythia8` and first calculations revealed that the signal yield is reduced by this approach [152]. This means that past calculations may result in too large limits on the size of extra dimensions if the asymptotic safety scenario is realized in nature. It would be an interesting task for future studies to reinterpret previous results for this case.

- A better motivated measure for fine tuning should be developed to compare different models which are considered to solve the higgs mass hierarchy problem.

- Section 7.2 and equation 1.27 introduced the angular distribution as a potential way to differentiate between signal and background, yet the separation seemed too small compared to the dimuon invariant mass distribution to be considered in this search. The plots in figure 10.2 show that the angular distribution is well understood and it might be interesting to study if these quantities can be exploited using multi variate analysis techniques in order to reduce the DY background.

12.3. Acknowledgements

References

[1] L. Randall, *Warped Passages: Unravelling the Mysteries of the Universe's Hidden Dimensions.* Harper and Collins, New York, NY, 2005.

[2] Wikimedia Commons, "Black ant on a line." Published under Creative Commons license, Sep, 2013.
`http://commons.wikimedia.org/wiki/File:Black_ant_on_the_rope.jpg`.

[3] Stefan Antonius Schmitz, *Search for large spatial extra dimensions with dimuon events from 7 TeV pp collisions at CMS.* PhD thesis, RWTH Aachen University, 2013.

[4] T. G. Rizzo, "Pedagogical introduction to extra dimensions," *eConf* **C040802** (2004) L013, `arXiv:hep-ph/0409309 [hep-ph]`.

[5] G. Nordström, "Über die Möglichkeit, das elektromagnetische Feld und das Gravitationsfeld zu vereinigen," *Physikalische Zeitschrift* no. 15, (1914) 504–506.

[6] Theodor Kaluza, *Zum Unitätsproblem der Physik*, vol. Juli-Dec 1921. Verlag der Akademie der Wissenschaften, Berlin, 1921.
`http://www.biodiversitylibrary.org/item/92690`.

[7] E. Witten, "String theory dynamics in various dimensions," *Nucl.Phys.* **B443** (1995) 85–126, `arXiv:hep-th/9503124 [hep-th]`.

[8] M. Duff, "M theory (The Theory formerly known as strings)," *Int.J.Mod.Phys.* **A11** (1996) 5623–5642, `arXiv:hep-th/9608117 [hep-th]`.

[9] A. Thompson and B. N. Taylor, "Guide for the use of the international system of units (si)," NIST Special Publication 811, NIST, 2008.

[10] I. Aitchison and A. Hey, *Gauge Theories in Particle Physics: Volume I: From Relativistic Quantum Mechanics to QED, Third Edition.* Graduate Student Series in Physics. Taylor & Francis, 2002.

[11] I. Aitchison and A. Hey, *Gauge Theories in Particle Physics: QCD and the Electroweak Theory, Third Edition.* Graduate Student Series in Physics. Taylor & Francis, 2003.

[12] F. Halzen and A. D. Martin, *Quarks and Leptons: An Introductory Course in Modern Particle Physics.* Wiley India Pvt Limited, 2008.

[13] G. Altarelli, "Collider Physics within the Standard Model: a Primer," `arXiv:1303.2842 [hep-ph]`.

[14] M. Gonzalez-Garcia and Y. Nir, "Neutrino masses and mixing: Evidence and implications," *Rev.Mod.Phys.* **75** (2003) 345–402, `arXiv:hep-ph/0202058 [hep-ph]`.

[15] N. Arkani-Hamed, S. Dimopoulos, and G. Dvali, "The Hierarchy problem and new dimensions at a millimeter," *Phys.Lett.* **B429** (1998) 263–272, `arXiv:hep-ph/9803315 [hep-ph]`.

[16] S. P. Martin, "A Supersymmetry Primer," `arXiv:9709356 [hep-ph]`.

[17] M. F. Sohnius, "Introducing supersymmetry," *Phys. Rep.* **128** no. 2-3, (Nov., 1985) 39–204.

[18] J. Beringer *et al.*, "Review of Particle Physics," *Phys. Rev. D* **86** no. 1, (July, 2012) 010001.

[19] Collins, John C. and Soper, Davison E. and Sterman, George F., "Factorization of Hard Processes in QCD," *Adv.Ser.Direct.High Energy Phys.* **5** (1988) 1–91.

[20] The LEP Collaboration, ALEPH Collaboration, DELPHI Collaboration, L3 Collaboration, OPAL Collaboration, LEP Electroweak Working Group, *et al.*, "A Combination of Preliminary Electroweak Measurements and Constraints on the Standard Model," `arXiv:hep-ex/0412015 [hep-ex]`.

[21] L. Cerrito, "Top quark and Electroweak measurements at the Tevatron," *J. Phys. Conf. Ser.* **259** (Nov., 2010) 012019, `arXiv:1010.1735 [hep-ex]`.

[22] **CMS** Collaboration, "Observation of a new boson with mass near 125 GeV in pp collisions at $\sqrt{s} = 7$ and 8 TeV," *J. High Energy Phys.* **2013** no. 6, (June, 2013) 81, `arXiv:1303.4571`.

[23] **ATLAS** Collaboration, "Observation of a new particle in the search for the Standard Model Higgs boson with the ATLAS detector at the LHC," *Phys. Lett. B* **716** no. 1, (2012) 1–29.

[24] Nobelprize.org, "The nobel prize in physics 2013." Nobel media ab 2013. web., Feb, 2014. `http://www.nobelprize.org/nobel_prizes/physics/laureates/2013/`.

[25] S. D. Drell and T.-M. Yan, "Massive lepton-pair production in hadron-hadron collisions at high energies," *Phys. Rev. Lett.* **25** (Sep, 1970) 902–902.

[26] A. K. Gupta, N. K. Mondal, and S. Raychaudhuri, "Constraining Large Extra Dimensions Using Dilepton Data from the Tevatron Collider," `arXiv:hep-ph/9904234 [hep-ph]`.

[27] A. Djouadi, "The anatomy of electroweak symmetry breaking," *Phys. Rep.* **457** no. 1-4, (Feb., 2008) 1–216, `arXiv:hep-ph/0503172 [hep-ph]`.

[28] J. F. Donoghue, "Introduction to the effective field theory description of gravity," `arXiv:gr-qc/9512024 [gr-qc]`.

[29] DeWitt, Bryce S., "Quantum Theory of Gravity. I. The Canonical Theory," *Phys. Rev.* **160** (Aug, 1967) 1113–1148.

[30] R. P. Feynman, "The quantum theory of gravitation," *Acta Phys. Polon.* **24** (1963) 697–722.

References

[31] T. Han, J. D. Lykken, and R.-J. Zhang, "On Kaluza-Klein states from large extra dimensions," *Phys.Rev.* **D59** (1999) 105006, `arXiv:hep-ph/9811350 [hep-ph]`.

[32] G. F. Giudice, R. Rattazzi, and J. D. Wells, "Quantum gravity and extra dimensions at high-energy colliders," *Nucl.Phys.* **B544** (1999) 3–38, `arXiv:hep-ph/9811291 [hep-ph]`.

[33] R. Franceschini, P. P. Giardino, G. F. Giudice, P. Lodone, and A. Strumia, "LHC bounds on large extra dimensions," *JHEP* **1105** (2011) 092, `arXiv:1101.4919 [hep-ph]`.

[34] T. Sjostrand, S. Mrenna, and P. Z. Skands, "A Brief Introduction to PYTHIA 8.1," *Comput.Phys.Commun.* **178** (2008) 852–867, `arXiv:0710.3820 [hep-ph]`.

[35] S. Ask, "Simulation of Z plus Graviton/Unparticle Production at the LHC," *Eur.Phys.J.* **C60** (2009) 509–516, `arXiv:0809.4750 [hep-ph]`.

[36] G. L. Landsberg, "Extra dimensions and more...," `arXiv:hep-ex/0105039 [hep-ex]`.

[37] K. Cheung, W.-Y. Keung, and T.-C. Yuan, "Collider phenomenology of unparticle physics," *Phys. Rev. D* **76** no. 5, (Sept., 2007) 37, `arXiv:0706.3155`.

[38] G. Aad *et al.*, "Search for contact interactions in dilepton events from pp collisions at with the ATLAS detector," *Phys. Lett. B* **712** no. 1-2, (May, 2012) 40–58.

[39] C. Hoyle, D. Kapner, B. R. Heckel, E. Adelberger, J. Gundlach, *et al.*, "Sub-millimeter tests of the gravitational inverse-square law," *Phys.Rev.* **D70** (2004) 042004, `arXiv:hep-ph/0405262 [hep-ph]`.

[40] E. Adelberger, J. Gundlach, B. Heckel, S. Hoedl, and S. Schlamminger, "Torsion balance experiments: A low-energy frontier of particle physics," *Prog. Part. Nucl. Phys.* **62** no. 1, (Jan., 2009) 102–134.

[41] A. Kehagias and K. Sfetsos, "Deviations from the 1/r2 Newton law due to extra dimensions," *Phys. Lett. B* **472** no. 1-2, (Jan., 2000) 39–44, `arXiv:hep-ph/9905417 [hep-ph]`.

[42] C. D. Hoyle, U. Schmidt, B. R. Heckel, E. G. Adelberger, J. H. Gundlach, D. J. Kapner, and H. E. Swanson, "Submillimeter Test of the Gravitational Inverse-Square Law: A Search for "Large" Extra Dimensions," *Phys. Rev. Lett.* **86** no. 8, (Feb., 2001) 1418–1421.

[43] T. A. Wagner, S. Schlamminger, J. H. Gundlach, and E. G. Adelberger, "Torsion-balance tests of the weak equivalence principle," *Class. Quantum Gravity* **29** no. 18, (Sept., 2012) 184002, `arXiv:1207.2442`.

[44] R. Spero, J. Hoskins, R. Newman, J. Pellam, and J. Schultz, "Test of the Gravitational Inverse-Square Law at Laboratory Distances," *Phys. Rev. Lett.* **44** no. 25, (June, 1980) 1645–1648.

[45] J. Hoskins, R. Newman, R. Spero, and J. Schultz, "Experimental tests of the gravitational inverse-square law for mass separations from 2 to 105 cm," *Phys. Rev. D* **32** no. 12, (Dec., 1985) 3084–3095.

[46] L.-C. Tu, S.-G. Guan, J. Luo, C.-G. Shao, and L.-X. Liu, "Null Test of Newtonian Inverse-Square Law at Submillimeter Range with a Dual-Modulation Torsion Pendulum," *Phys. Rev. Lett.* **98** no. 20, (May, 2007) 201101.

[47] J. C. Long *et al.*, "Upper limits to submillimetre-range forces from extra space-time dimensions.," *Nature* **421** no. 6926, (Feb., 2003) 922–5, `arXiv:hep-ph/0210004 [hep-ph]`.

[48] S. Smullin *et al.*, "Constraints on Yukawa-type deviations from Newtonian gravity at 20 microns," *Phys. Rev. D* **72** no. 12, (Dec., 2005) 122001.

[49] **LEP** Collaboration, "Combination of LEP Results on Direct Searches for Large Extra Dimensions," LEP Exotica WG 2004-03, CERN, Geneva, 2004. `http://lepexotica.web.cern.ch/LEPEXOTICA/notes/2004-03/ed_note_final.ps.gz`.

[50] **D0** Collaboration, "Search for Large Extra Spatial Dimensions in the Dielectron and Diphoton Channels in $p\bar{p}$ Collisions at $\sqrt{s} = 1.96\,\text{TeV}$," *Phys. Rev. Lett.* **102** no. 5, (Feb., 2009) 051601, `arXiv:0809.2813`.

[51] **CMS** Collaboration, "Search for large extra dimensions in dimuon and dielectron events in pp collisions at $\sqrt{s} = 7\,\text{TeV}$," *Phys. Lett. B* **711** no. 1, (May, 2012) 15–34, `arXiv:1202.3827`.

[52] **ATLAS** Collaboration, "Search for contact interactions and large extra dimensions in dilepton events from pp collisions at $\sqrt{s} = 7\,\text{TeV}$ with the ATLAS detector," *Phys. Rev. D* **87** no. 1, (Jan., 2013) 015010.

[53] S. Hannestad and G. Raffelt, "Supernova and neutron-star limits on large extra dimensions reexamined," *Phys. Rev. D* **67** no. 12, (June, 2003) 125008, `arXiv:hep-ph/0304029 [hep-ph]`.

[54] J. Beringer *et al.*, "Review of Particle Physics," *Phys. Rev. D* **86** no. 1, (July, 2012) 010001.

[55] S. Hannestad, "Stringent Neutron-Star Limits on Large Extra Dimensions," *Phys. Rev. Lett.* **88** no. 7, (Feb., 2002) 071301, `arXiv:hep-ph/0110067 [hep-ph]`.

[56] CERN, "Cern member state information page," status 19.3.2013. `http://home.web.cern.ch/about/member-states`.

[57] M. Brice, "Aerial View of the CERN taken in 2008. Puplished under CC license.." Jul, 2008.

[58] O. S. Bruening *et al.*, *LHC Design Report*. CERN, Geneva, 2004.

[59] L. Evans and P. Bryant, *LHC Machine*, vol. 3. 2008.

References

[60] **ALICE** Collaboration, "The ALICE experiment at the CERN LHC," 2008.

[61] **ATLAS** Collaboration, "The ATLAS Experiment at the CERN Large Hadron Collider," *J. Instrum.* **3** no. 08, (Aug., 2008) S08003–S08003. `https://cdsweb.cern.ch/record/1129811`.

[62] **LHCb** Collaboration, "The LHCb Detector at the LHC," *J. Instrum.* **3** no. 08, (Aug., 2008) S08005–S08005. `https://cds.cern.ch/record/1129809`.

[63] **CMS** Collaboration, "CMS Luminosity - Puplic Results," status: 19.3.2014. `https://twiki.cern.ch/twiki/bin/view/CMSPublic/LumiPublicResults`.

[64] **CMS** Luminosity Group, "Multi-year collisions plots," 2013. `https://twiki.cern.ch/twiki/bin/view/CMSPublic/LumiPublicResults`.

[65] **CMS** Collaboration, "The CMS experiment at the CERN LHC," *J. Instrum.* **3** no. 08, (Aug., 2008) S08004–S08004. `http://inspirehep.net/record/796887?ln=de`.

[66] CMS Sketchup Project, "CMS cutaway views `https://twiki.cern.ch/twiki/bin/view/CMSPublic/SketchUpCMSGallery`," 2013.

[67] **CMS** Collaboration, "Missing transverse energy performance of the CMS detector," *J. Instrum.* **6** no. 09, (Sept., 2011) P09001–P09001, `arXiv:1106.5048`.

[68] **CMS** Collaboration, "2012 ECAL detector performance plots," CMS-DP 2013-007, Mar, 2013.

[69] **CMS** Collaboration, "The CMS hadron calorimeter project,". `https://cds.cern.ch/record/357153`.

[70] **CMS** Collaboration, "Jet Energy Resolution in CMS at $\sqrt{s} = 7\,\text{TeV}$," CMS-PAS-JME 10-014, 2011. `http://cds.cern.ch/record/1339945`.

[71] A. Tropiano, "Tracking and vertexing performance in CMS." conference talk Vertex 2012, Sep, 2012. `http://vertex2012.knu.ac.kr/slide/s1/cms.pdf`.

[72] **CMS** Collaboration, "Measurement of the properties of a Higgs boson in the four-lepton final state," `arXiv:1312.5353`.

[73] **CMS** Collaboration, *The CMS muon project.* CERN, 1997. `http://cds.cern.ch/record/343814`.

[74] **CMS** Collaboration, "Alignment of the CMS muon system with cosmic-ray and beam-halo muons," *J. Instrum.* **5** no. 03, (Mar., 2010) T03020–T03020.

[75] J. Brooke, "Performance of the CMS Level-1 Trigger," *PoS* **ICHEP2012** (2013) 508. `http://inspirehep.net/record/1218375`.

[76] J. Brooke, "Performance of the cms level-1 trigger," in *ICHEP*. July, 2012. `http://indico.cern.ch/event/181298/session/74/contribution/673`.

[77] Jim Brooke, "CMS Trigger Design and Limitations." Exotica Workshop at the PCTS, Nov, 2013. `https://indico.cern.ch/event/266531/`.

[78] C. Eck, J. Knobloch, *et al.*, *LHC computing Grid: Technical Design Report. Version 1.06 (20 Jun 2005)*. Technical Design Report LCG. CERN, Geneva, 2005.

[79] **WLCG** Collaboration, "Grid Tier sites overview," status: 19.3.2014. `https://espace.cern.ch/WLCG-document-repository/images1/WLCG/CCApr13-Tiers0-1-2.pdf`.

[80] C. Rovelli, "The detailed simulation of the CMS detector," CMS-CR 2007-082, CERN, Geneva, Oct, 2007.

[81] S. Agostinelli *et al.*, "Geant4—a simulation toolkit," *Nucl. Instruments Methods Phys. Res. Sect. A Accel. Spectrometers, Detect. Assoc. Equip.* **506** no. 3, (July, 2003) 250–303.

[82] Carsten Magass, Klaas Ole Padeken at al., "ACSUSYSkimmer Twiki page," status: 19.3.2014. `https://twiki.cern.ch/twiki/bin/viewauth/CMS/ACSusyAnalysis`.

[83] R. Brun and F. Rademakers, "ROOT — An object oriented data analysis framework," *Nucl. Instruments Methods Phys. Res. Sect. A Accel. Spectrometers, Detect. Assoc. Equip.* **389** no. 1-2, (Apr., 1997) 81–86.

[84] B. Jones and B. Tompkins, "A physicist's guide to kalman filters," 1998. `http://citeseerx.ist.psu.edu/viewdoc/summary?doi=10.1.1.57.1034`.

[85] **CMS** Collaboration, "Muon Reconstruction in the CMS Detector," CMS AN 08-097, 2008.

[86] Jordan Tucker, "Tracker-plus-first-muon-station (TPFMS) reconstructor and the TMR cocktail." Talk at Exotica Muon WG meeting, 6.5.2010. `https://indico.cern.ch/event/93943/contribution/0/3/material/slides/1.pdf`.

[87] Piotr Traczyk, "TeV Muons & Picky Muon Reco." Talk at EXOTICA Muon WG meeting, 6.5.2010. `https://indico.cern.ch/event/93943/contribution/0/2/material/slides/0.pdf`.

[88] Piotr Traczyk, "Updates in muon momentum assignment and high p_T ID." Talk at muon POG meeting, 1.10.2012. `https://indico.cern.ch/event/209971/material/slides/0?contribId=4`.

[89] J. Tucker, "Muon momentum resolution using cosmic muons: update with 2011 data." Muon POG Meeting, 31.1.2012.

[90] **CMS** Collaboration, "Performance of CMS muon reconstruction in pp collision events at $\sqrt{s} = 7\,\text{TeV}$," *Journal of Instrumentation* **7** (Oct., 2012) 2P, `arXiv:1206.4071 [physics.ins-det]`.

[91] Eduardo Navarro De Martino, "Single Trigger Muon Efficiencies of Run2012D." Muon HLT meeting, 15.1.2013.

References

[92] **CMS** Collaboration, "Search for high mass resonances decaying to muon pairs at $\sqrt{s} = 8\,\text{TeV}$," CMS AN 12-422, 2012.

[93] **CMS** Collaboration, "Search for high-mass resonances decaying to muon pairs with collisions gathered at $\sqrt{s} = 7\,\text{TeV}$," CMS AN 11-472, 2012.

[94] **CDF** Collaboration, "Search for New Physics with High Mass Tau Pairs in CDF," 2004. CDF note 7167.

[95] **CMS** Collaboration, "Search for Extra Dimensions in Dimuon Events in pp Collisions at sqrt(s) = 7 TeV," CMS-PAS EXO-10-020, CERN, Geneva, 2011.

[96] **CMS** Collaboration, "Search for Extra Dimensions in Dimuon Events in pp Collisions at $\sqrt{s} = 7\,\text{TeV}$," CMS PAS EXO-11-039, CERN, Geneva, 2011.

[97] **CMS** Collaboration, "Search for contact interactions and large extra dimensions in dilepton events from pp collisions at sqrt(s)=7 TeV with the ATLAS detector," *Phys. Rev. D* **87** no. 1, (Jan., 2013) 015010, `1211.1150`.

[98] S. Frixione, P. Nason, and C. Oleari, "Matching NLO QCD computations with parton shower simulations: the POWHEG method," *J. High Energy Phys.* **2007** no. 11, (Nov., 2007) 070–070.

[99] T. Sjöstrand, S. Mrenna, and P. Skands, "PYTHIA 6.4 physics and manual," *J. High Energy Phys.* **2006** no. 05, (May, 2006) 026–026.

[100] H.-L. Lai *et al.*, "New parton distributions for collider physics," *Phys. Rev. D* **82** no. 7, (Oct., 2010) 074024, `arXiv:1007.2241`.

[101] K. Melnikov and F. Petriello, "Electroweak gauge boson production at hadron colliders through O(αs2)," *Phys. Rev. D* **74** no. 11, (Dec., 2006) 114017, `arXiv:hep-ph/0609070 [hep-ph]`.

[102] R. Gavin, Y. Li, F. Petriello, and S. Quackenbush, "FEWZ 2.0: A code for hadronic Z production at next-to-next-to-leading order," *Comput. Phys. Commun.* **182** no. 11, (Nov., 2011) 2388–2403.

[103] **CMS** Collaboration, "PDF Uncertainties for Z' searches at 8 TeV," CMS AN 12-348, 2012.

[104] L. Barzè *et al.*, "Neutral-current Drell–Yan with combined QCD and electroweak corrections in the POWHEG BOX," *Eur. Phys. J. C* **73** no. 6, (June, 2013) 2474, `arXiv:1302.4606`.

[105] V. Zykunov, "Weak radiative corrections to the Drell-Yan process for large invariant mass of a dilepton pair," *Phys. Rev. D* **75** no. 7, (Apr., 2007) 073019, `arXiv:hep-ph/0509315 [hep-ph]`.

[106] C. M. C. Calame *et al.*, "Precision electroweak calculation of the production of a high transverse-momentum lepton pair at hadron colliders," *J. High Energy Phys.* **2007** no. 10, (Nov., 2007) 109–109, `arXiv:0710.1722`.

[107] G. Corcella, I. G. Knowles, *et al.*, "HERWIG 6: an event generator for hadron emission reactions with interfering gluons (including supersymmetric processes)," *J. High Energy Phys.* **2001** no. 01, (Jan., 2001) 010–010, `arXiv:0011363 [hep-ph]`.

[108] A. D. Martin, R. G. Roberts, *et al.*, "Parton distributions incorporating QED contributions," *Eur. Phys. J. C* **39** no. 2, (Feb., 2005) 155–161, `arXiv:0411040 [hep-ph]`.

[109] **CMS** Collaboration, "Search for high-mass resonances decaying to muon pairs with $15\,pb^{-1}$ of collisions gathered at $\sqrt{s} = 7\,\text{TeV}$," CMS AN 10-317, 2010.

[110] D. Stump *et al.*, "Inclusive jet production, parton distributions, and the search for new physics," *J. High Energy Phys.* **2003** no. 10, (Oct., 2003) 046–046.

[111] **CMS** Collaboration, "Search for Contact Interactions in Dilepton Mass Spectra in pp Collisions at $\sqrt{s} = 8\,\text{TeV}$," CMS PAS EXO-12-020, CERN, Geneva, 2014.

[112] PYTHIA 8 Group, "Pythia 8 Online Manual," 2014. `http://home.thep.lu.se/~torbjorn/pythia81html/Welcome.html`.

[113] R. Corke and T. Sjöstrand, "Interleaved parton showers and tuning prospects," *J. High Energy Phys.* **2011** no. 3, (Mar., 2011) 32, `arXiv:1011.1759`.

[114] A. Buckley, T. Sjöstrand, *et al.*, "General-purpose event generators for LHC physics," *Phys. Rep.* **504** no. 5, (July, 2011) 145–233, `arXiv:1101.2599`.

[115] P. Mathews *et al.*, "Next-to-leading order QCD corrections to the Drell–Yan cross section in models of TeV-scale gravity," *Nucl. Phys. B* **713** no. 1-3, (May, 2005) 333–377, `arXiv:hep-ph/0411018 [hep-ph]`.

[116] J. Alwall *et al.*, "MadGraph 5: going beyond," *J. High Energy Phys.* no. 6, (June, 2011) 128, `arXiv:1106.0522`.

[117] amc@NLO Group, "amc@NLO Hopmepage," 2014. `http://amcatnlo.web.cern.ch/amcatnlo/`.

[118] R. Frederix *et al.*, "Drell–Yan, ZZ, WW - production in SM & ADD model to NLO + PS accuracy at the LHC," *Eur. Phys. J. C* **74** no. 2, (Feb., 2014) 2745, `arXiv:1307.7013`.

[119] **CMS** Collaboration, "CMS Luminosity Based on Pixel Cluster Counting - Summer 2013 Update," CMS PAS LUM-13-001, CERN, Geneva, 2013.

[120] S. van der Meer, "Calibration of the effective beam height in the ISR," Tech. Rep. CERN-ISR-PO-68-31. ISR-PO-68-31, CERN, Geneva, 1968.

[121] R. Field, "Min-Bias and the Underlying Event at the LHC," `arXiv:1202.0901`.

[122] R. Field, "Predicting "Min-Bias" and the the "Underlying Event" at the LHC." Minimum Bias and Underlying Event Working Group meeting, 2.5.2010. `http://indico.cern.ch/event/83609/session/2/contribution/6/material/slides/1.pdf`.

References

[123] M. CACCIARI and G. SALAM, "Pileup subtraction using jet areas," *Phys. Lett. B* **659** no. 1-2, (Jan., 2008) 119–126, `arXiv:0707.1378`.

[124] G. Azuelos *et al.*, "Electroweak Physics," `arXiv:0003275 [hep-ph]`.

[125] **CMS** Collaboration, "Measurement of inclusive w and z boson cross section in pp collisions at $\sqrt{s} = 8\,\text{TeV}$," CMS AN 12-067, 2012.

[126] M. Botje *et al.*, "The PDF4LHC Working Group Interim Recommendations," `arXiv:1101.0538`.

[127] M. Whalley, D. Bourilkov, *et al.*, "The Les Houches accord PDFs (LHAPDF) and LHAGLUE," `arXiv:hep-ph/0508110 [hep-ph]`.

[128] R. Gavin *et al.*, "FEWZ 2.0: A code for hadronic Z production at next-to-next-to-leading order," *Comput.Phys.Commun.* **182** (2011) 2388–2403, `arXiv:1011.3540 [hep-ph]`.

[129] **CMS** Collaboration, "Measurement of the high-pt momentum scale with the endpoint method," CMS AN 11-479, 2011.

[130] T. K. for the UF group, "Endpoint results with the latest alignment." Muon POG Meeting, 2012.

[131] **CMS** Collaboration, "Search for W' in the leptonic channels in pp Collisions at $\sqrt{s} = 7\,\text{TeV}$," CMS-PAS EXO-11-024, 2011.

[132] P. Uwer, "EasyNData: A Simple tool to extract numerical values from published plots," `arXiv:0710.2896 [physics.comp-ph]`.

[133] **CMS** Collaboration, "Search for Large Extra Spatial Dimensions in Dielectron Production with the CMS Detector," CMS-PAS-EXO 12-031, CERN, Geneva, 2013.

[134] **CMS** Collaboration, "CMS Higgs combined tool - Twiki page," status: 21.3.2014. `https://github.com/cms-analysis/HiggsAnalysis-CombinedLimit`.

[135] L. Moneta, "Roostats, a framework for advanced statistical analysis," in *EPS*. July, 2013. `https://indico.cern.ch/event/218030/session/20/material/slides/0?contribId=482`.

[136] G. Cowan, *Statistical Data Analysis*. Clarendon Press, 1998.

[137] J. Stanford and S. Vardeman, *Statistical Methods for Physical Science*. Methods of experimental physics. Elsevier Science, 1994.

[138] N. Johnson, S. Kotz, and N. Balakrishnan, *Continuous univariate distributions*. Distributions in statistics. Wiley, New York, second ed.

[139] L. Demortier *et al.*, "Reference priors for high energy physics," *Phys. Rev. D* **82** no. 3, (Aug., 2010) 034002, `arXiv:1002.1111`.

[140] W. Press, *Numerical recipes : the art of scientific computing.* Cambridge University Press, Cambridge, UK New York, 2007.

[141] N. Metropolis, A. W. Rosenbluth, M. N. Rosenbluth, A. H. Teller, and E. Teller, "Equation of State Calculations by Fast Computing Machines," *J. Chem. Phys.* **21** no. 6, (1953) 1087.

[142] Patil, V.V and Kulkarni, H.V., "Comparison of Confidence Intervals for the Poisson Mean: Some New Aspects," *REVSTAT – Statistical Journal* no. 10, (June, 2012) 211–227.

[143] CMS statistics comittee, "Asymmetric Error Bars for Poisson Event Counts ." Twiki page, status 26.5.2014.
`https://twiki.cern.ch/twiki/bin/viewauth/CMS/PoissonErrorBars`.

[144] C. Kolda and H. Murayama, "The Higgs mass and new physics scales in the minimal standard model," *J. High Energy Phys.* **2000** no. 07, (July, 2000) 035–035, `arXiv:hep-ph/0003170 [hep-ph]`.

[145] T. Gleisberg *et al.*, "Helicity formalism for spin-2 particles," *J. High Energy Phys.* **2003** no. 09, (Sept., 2003) 001–001, `arXiv:0306182 [hep-ph]`.

[146] J. L. Feng, "Naturalness and the Status of Supersymmetry," *Annu. Rev. Nucl. Part. Sci.* **63** no. 1, (Oct., 2013) 351–382, `arXiv:1302.6587`.

[147] S. Fichet, "Quantified naturalness from Bayesian statistics," *Phys. Rev. D* **86** no. 12, (Dec., 2012) 125029, `arXiv:1204.4940`.

[148] M. E. Cabrera, A. Casas, and R. R. de Austri, "Bayesian approach and naturalness in MSSM analyses for the LHC," *J. High Energy Phys.* **2009** no. 03, (Mar., 2009) 075–075, `arXiv:0812.0536`.

[149] J. Brooke and B. Dahmes, "CMS Trigger : Design and Limitations." CMS Exotica Workshop, Nov, 2013. `https://indico.cern.ch/event/266531/session/0/contribution/40/material/slides/0.pdf`.

[150] E. Gerwick, "Phenomenology of asymptotic safety," 2011.
`http://www.thphys.uni-heidelberg.de/~plehn/includes/theses/gerwick.pdf`.

[151] E. Gerwick, D. Litim, and T. Plehn, "Asymptotic safety and Kaluza-Klein gravitons at the LHC," *Phys. Rev. D* **83** no. 8, (Apr., 2011) 084048.

[152] Gudrun Hiller, "Asymptotically Safe Gravity and the TeV-Scale." Seminar talk at RWTH, 17.11.2013.

Selbständigkeitserklärung

Hiermit erkläre ich, dass ich die vorliegende Arbeit selbstständig und ohne fremde Hilfe verfasst und keine anderen Hilfsmittel als angegeben verwendet habe. Insbesondere versichere ich, dass ich alle wörtlichen und sinngemäßen Übernahmen aus anderen Werken als solche kenntlich gemacht habe.

―――――――――――

Tobias Pook

Appendices

A. Definitions for the Neutral Drell-Yan Background

This section contains some additional definitions of the Drell-Yan cross section at LO. In particular $|D_z(\bar{s})|$ and the constants c_i in equation 1.27 are given by:

$$|D_z(s)| = \left| \frac{1}{s - m_Z^2 + i m_Z \Gamma_Z} \right| = \frac{1}{\left((s - m_Z^2)^2 + (m_z \Gamma_Z)^2 \right)^2} \qquad c_1 = 128 \cdot Q_q^2$$

$$c_2 = \frac{1}{16 \cdot \sin^4 \theta_W \cos^4 \theta_W} (L_l^2 \cdot (L_l^2 \cdot R_q^2 + R_l^2 \cdot L_q^2)) \quad c_3 = -\frac{2 \cdot Q_q}{\sin^2 \theta_W \cos^2 \theta_W} (L_l \cdot R_q + R_l \cdot L_q)$$

$$c_4 = \frac{1}{16 \cdot \sin^4 \theta_W \cos^4 \theta_W} (L_l^2 \cdot (L_l^2 L_q^2 + R_l^2 R_q^2)) \qquad c_5 = -\frac{2 \cdot Q_q}{\sin^2 \theta_W \cos^2 \theta_W} (L_l \cdot L_q + R_l \cdot R_q)$$

$$R_l = 4 \cdot \sin^2 \theta_W \qquad\qquad\qquad L_q = 4 \cdot (T_{3,q} - Q_q \cdot \sin \theta_W)$$

$$L_l = 4 \cdot \sin \theta_W - 2 \qquad\qquad\qquad R_q = -4 \cdot Q_q \cdot \sin_W^2$$

With the electric charge of the initial quark Q_q, the weak mixing (Weinberg) angle and the third component of the quarks weak isospin.

B. MC Samples

Background Monte Carlo

Process	Dataset
DY	DYToMuMu_M-1000_CT10_TuneZ2star_8TeV-powheg-pythia6_Summer12_DR53X-PU_S10_START53_V7C1-v1
	DYToMuMu_M-120_CT10_TuneZ2star_8TeV-powheg-pythia6_Summer12_DR53X-PU_S10_START53_V7C1-v1
	DYToMuMu_M-200_CT10_TuneZ2star_8TeV-powheg-pythia6_Summer12_DR53X-PU_S10_START53_V7C1-v1
	DYToMuMu_M-400_CT10_TuneZ2star_8TeV-powheg-pythia6_Summer12_DR53X-PU_S10_START53_V7C1-v1
	DYToMuMu_M-500_CT10_TuneZ2star_8TeV-powheg-pythia6_Summer12_DR53X-PU_S10_START53_V7C1-v1
	DYToMuMu_M-700_CT10_TuneZ2star_8TeV-powheg-pythia6_Summer12_DR53X-PU_S10_START53_V7C1-v1
	DYToMuMu_M-800_CT10_TuneZ2star_8TeV-powheg-pythia6_Summer12_DR53X-PU_S10_START53_V7C1-v1
	DYToMuMu_M-1000_CT10_TuneZ2star_8TeV-powheg-pythia6_Summer12_DR53X-PU_S10_START53_V7C1-v1
	DYToMuMu_M-1500_CT10_TuneZ2star_8TeV-powheg-pythia6_Summer12_DR53X-PU_S10_START53_V7C1-v1
	DYToMuMu_M-2000_CT10_TuneZ2star_8TeV-powheg-pythia6_Summer12_DR53X-PU_S10_START53_V7C1-v1
$\bar{t}W$	Tbar_tW-channel-DR_TuneZ2star_8TeV-powheg-tauola_Summer12_DR53X-PU_S10_START53_V7A-v1
$t\bar{t}$	TTJets_MassiveBinDECAY_TuneZ2star_8TeV-madgraph-tauola_Summer12_DR53X-PU_S10_START53_V7A-v1
tW	T_tW-channel-DR_TuneZ2star_8TeV-powheg-tauola_Summer12_DR53X-PU_S10_START53_V7A-v1
W+Jets	WJetsToLNu_TuneZ2Star_8TeV-madgraph-tarball_Summer12_DR53X-PU_S10_START53_V7A-v1
WW	WW_TuneZ2star_8TeV_pythia6_tauola_Summer12_DR53X-PU_S10_START53_V7A-v1
WZ	WZ_TuneZ2star_8TeV_pythia6_tauola_Summer12_DR53X-PU_S10_START53_V7A-v1
ZZ	ZZ_TuneZ2star_8TeV_pythia6_tauola_Summer12_DR53X-PU_S10_START53_V7A-v1

Table B.1.: Dataset paths for background MC samples

Background Monte Carlo

Process	Dataset
	ADDdiLepton_LambdaT-1600_Tune4C_8TeV-pythia8_Summer12_DR53X-PU_S10_START53_V19E-v1SIM
	ADDdiLepton_LambdaT-2400_Tune4C_8TeV-pythia8_Summer12_DR53X-PU_S10_START53_V19E-v1SIM
ADD	ADDdiLepton_LambdaT-3600_Tune4C_8TeV-pythia8_Summer12_DR53X-PU_S10_START53_V19E-v1SIM
$G \to \mu\mu$	ADDdiLepton_LambdaT-4000_Tune4C_8TeV-pythia8_Summer12_DR53X-PU_S10_START53_V19E-v1SIM
	ADDdiLepton_LambdaT-4400_Tune4C_8TeV-pythia8_Summer12_DR53X-PU_S10_START53_V19E-v1SIM
	ADDdiLepton_LambdaT-4800_Tune4C_8TeV-pythia8_Summer12_DR53X-PU_S10_START53_V19E-v1SIM
	ADDdiLepton_LambdaT-5200_Tune4C_8TeV-pythia8_Summer12_DR53X-PU_S10_START53_V19E-v1SIM

Table B.2.: Dataset paths for MC samples

C. Detailed Event Description

C.1. List of events above 900GeV

#	run	event	lumisection	$M_{\mu\mu}$ (GeV)	#	run	event	lumisection	$M_{\mu\mu}$ (GeV)
1	205694	398	416479300	1870.7	34	204601	186	252896431	1016.6
2	199409	553	676990060	1804.3	35	208487	96	170918748	1007.1
3	202178	931	1100609921	1711.8	36	202328	394	589121740	991.9
4	195378	193	225870452	1507.0	37	194115	280	257882341	989.7
5	206207	153	186909124	1494.8	38	201173	167	145943466	985.6
6	207924	215	209747123	1467.7	39	207273	39	47981615	982.8
7	199409	531	654043540	1412.4	40	194150	244	302855323	982.3
8	199833	1054	1136357968	1367.5	41	199008	160	179760542	964.3
9	204601	1215	1278017291	1356.7	42	206187	215	274374421	960.1
10	194050	995	936530164	1313.5	43	199436	166	119847245	952.0
11	196433	77	39187003	1290.8	44	206243	676	974886749	950.6
12	207492	78	65524201	1258.6	45	205667	39	42407203	949.1
13	196431	90	66057632	1253.1	46	196334	105	115704481	944.5
14	208391	666	845554877	1240.6	47	196027	99	153238373	943.8
15	202237	327	509578194	1208.6	48	199008	591	721792661	941.3
16	204563	368	499818262	1165.1	49	200600	972	1200752090	938.3
17	194912	444	739866334	1162.5	50	206744	431	605265207	936.7
18	193621	1359	1067285891	1159.4	51	201669	57	104849581	929.3
19	198969	641	779619791	1159.3	52	196218	591	860336640	929.0
20	194225	13	14353212	1143.5	53	202060	413	527655267	922.3
21	199571	97	109753290	1137.9	54	201816	96	111085280	921.4
22	198271	699	802097775	1118.6	55	198969	378	494909584	919.0
23	199753	40	42023310	1104.0	56	206389	186	220375909	917.3
24	198487	1075	1150495912	1103.3	57	201202	341	312065562	911.7
25	206869	685	629195087	1096.0	58	195774	48	94924923	911.6
26	202504	733	919226848	1083.4	59	203912	642	732385521	907.5
27	194424	654	909915359	1079.7	60	194533	82	85367726	906.9
28	191718	171	211765901	1077.3	61	194050	1568	1391733189	905.6
29	201624	194	250169307	1062.0	62	201278	340	474535371	902.8
30	195915	556	836688041	1043.1	63	195397	472	673031590	902.5
31	207922	50	55833120	1037.3	64	208686	133	160898864	902.2
32	207884	4	4187119	1025.6	65	199574	79	60631621	900.7
33	204563	221	272281825	1023.1					

Table C.1.: List of events with invariant dimuon mass above $900\,\mathrm{GeV}$

C.2. Event displays

CMS Experiment at LHC, CERN
Data recorded: Sun Oct 21 16:29:50 2012 CEST
Run/Event: 205694 / 416479300
Lumi section: 398

Muon 0,
pt = 456 GeV
eta = -1.033
phi = 2.861

Muon 1,
pt = 502 GeV
eta = 1.542
phi = -0.280

CMS Experiment at LHC, CERN
Data recorded: Sun Oct 21 16:29:50 2012 CEST
Run/Event: 205694 / 416479300
Lumi section: 398

Muon 0,
pt = 456 GeV
eta = -1.033
phi = 2.861

Muon 1,
pt = 502 GeV
eta = 1.542
phi = -0.280

97
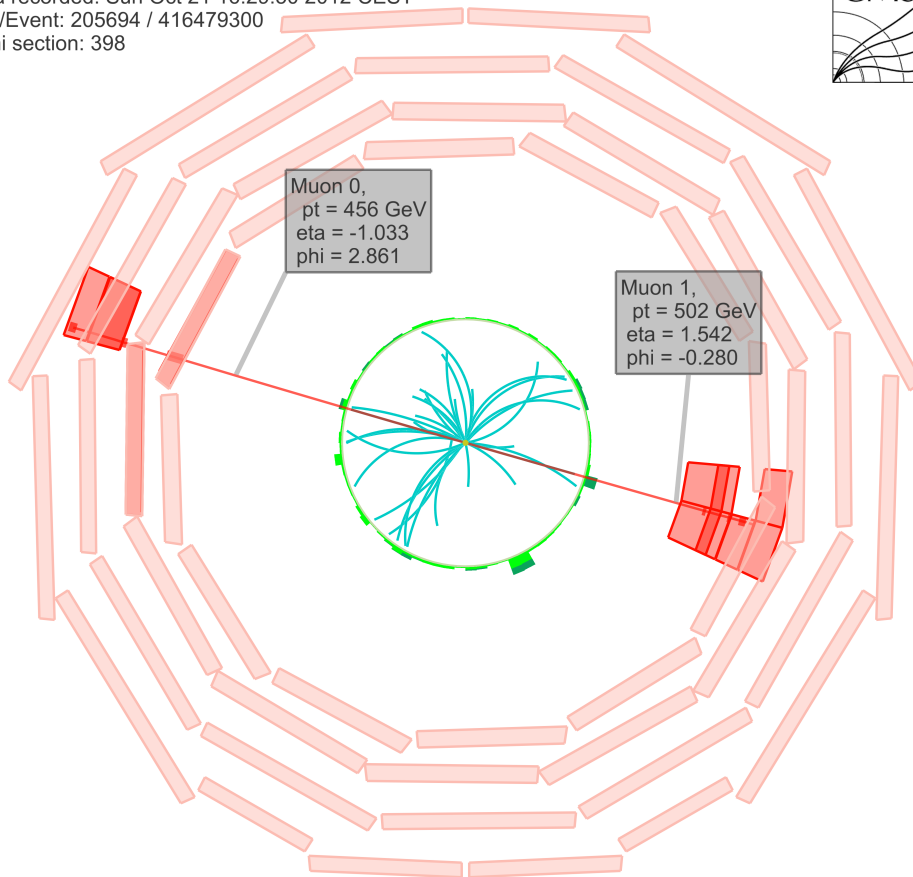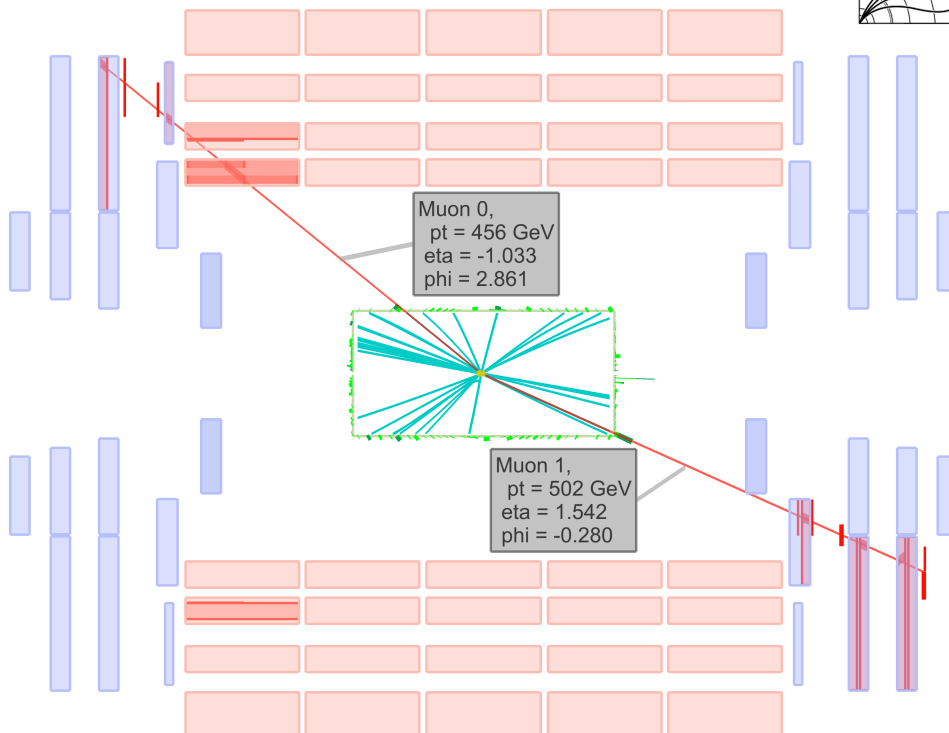
Figure C.1.: Event display for the event with the highest dimuon invariant mass as listed in table C.1